

RICE UNIVERSITY

**Rydberg Molecules and Polarons in Ultracold  
Strontium Gases**

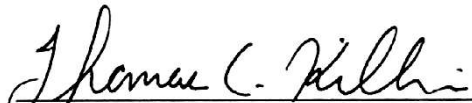
by

**Francisco Camargo**

A THESIS SUBMITTED  
IN PARTIAL FULFILLMENT OF THE  
REQUIREMENTS FOR THE DEGREE

**Doctor of Philosophy**

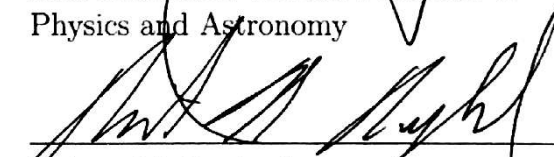
APPROVED, THESIS COMMITTEE:



Thomas C. Killian, Chair  
Professor of Physics and Astronomy



F. Barry Danning  
Sam and Helen Worden Professor of  
Physics and Astronomy



Robert M. Raphael  
Associate Professor of Bioengineering

Houston, Texas

June, 2017



# Abstract

## Rydberg Molecules and Polarons in Ultracold Strontium Gases

**Francisco Camargo**

In this work I describe the excitation spectra and decay mechanisms of Rydberg atoms in ultracold gases of strontium. In a few-body regime, we observe a highly structured spectrum reflecting excitation of ultralong-range molecules consisting of one or more ground-state atoms bound to the Rydberg core in potential wells formed by the Rydberg-electron wavefunction. In a many-body regime, with hundreds of ground-state atoms within the Rydberg orbital, the Rydberg atoms can be viewed as an impurity in a quantum gas, connecting to important concepts in condensed matter physics. The spectrum for impurity excitation displays signatures of polaronic states, in which the Rydberg atom significantly perturbs the density of the background gas.

Additionally, decay channels of Rydberg excitations are examined by monitoring the time evolution of Rydberg populations. The measured lifetimes reveal new information on the decay processes of Rydberg molecules and place limits on the time scales over which studies involving Rydberg species in cold, dense atomic gases can be undertaken and limit the coherence times for such measurements.



# Acknowledgments

I would like to thank my advisers Tom Killian and Barry Dunning who bestowed upon me the opportunity to initiate a new experiment. The intimidation induced by embarking on such an endeavor was overshadowed by their constant encouragement and support. To Roger Ding and Joe Whalen, my accomplices in building and conducting the experiments presented in this thesis, I'm proud to have worked with you and doubt not your future accomplishments. To Brian DeSalvo, thank you for illuminating the path in times of bewilderment. To Trevor Strickler, thank you for helping me keep my feet on the ground and always lending a reassuring word. To Richard Schmidt and Jesús Pérez-Ríos, thank you for the time and patience you have given me throughout our collaborations. To Jim Aman, I draw inspiration from the tenacity and focus with which you approach the task before you. Thank you for all the times you were more than willing to lend a helping hand.

To my mom, Maria Lorena Hidalgo-Ferretti, thank you for believing in me and guiding me through this journey. Your words of wisdom and compassion have been, and continue to be instrumental to the successes of my life. My accomplishments are your accomplishments.



# Contents

<b>Abstract</b>	<b>iii</b>
<b>Acknowledgments</b>	<b>v</b>
<b>1 Introduction</b>	<b>1</b>
1.1 Historical Perspective . . . . .	1
1.2 Rydberg Atoms . . . . .	3
1.3 Rydberg Molecules . . . . .	4
1.4 Thesis Organization . . . . .	5
<b>2 Cooling and Trapping <math>^{84}\text{Sr}</math></b>	<b>7</b>
2.1 Broad-Line Trap . . . . .	7
2.2 Narrow-Line Trap . . . . .	10
2.3 Optical-Dipole Trap . . . . .	10
2.4 $^{84}\text{Sr}$ BEC Production . . . . .	12
<b>3 Rydberg State Creation and Detection</b>	<b>21</b>
3.1 Driving Rydberg Transitions . . . . .	21
3.2 Rydberg Signal Detection . . . . .	22
3.2.1 Electric Field Ionization . . . . .	23
3.2.2 Selective Field Ionization . . . . .	24
3.2.3 Charged Particle Signal Detection . . . . .	27
<b>4 Few- to Many-Body Rydberg Molecule Regime</b>	<b>33</b>

4.1	Electron-Atom Interactions . . . . .	33
4.2	Spectroscopy Measurements . . . . .	35
<b>5</b>	<b>Rydberg State Decay</b>	<b>41</b>
5.1	Decay Rate in Few-Body Regime . . . . .	42
5.2	Decay Rates in Many-Body Regime . . . . .	47
5.3	Atom-Rydberg Collisions . . . . .	56
<b>6</b>	<b>Mean-Field Description in the Many-Body Regime</b>	<b>61</b>
6.1	Mean-Field Spectrum . . . . .	61
6.2	Analysis . . . . .	66
<b>7</b>	<b>Rydberg Polarons in a Bose-Einstein Condensate</b>	<b>75</b>
7.1	Background . . . . .	75
7.2	Results . . . . .	78
<b>8</b>	<b>Conclusion</b>	<b>83</b>
	<b>Appendices</b>	<b>85</b>
<b>A</b>	<b>Thermal Gas Density</b>	<b>87</b>
A.1	Spatial Density Distribution . . . . .	87
A.2	Density Distribution . . . . .	90
A.3	Trap Frequency Measurement . . . . .	91
A.4	Numerical Density Distribution . . . . .	92
<b>B</b>	<b>BEC Density</b>	<b>97</b>
B.1	Density Distribution . . . . .	97
B.2	Two-Component BEC . . . . .	98
B.3	BEC Trap Frequency and Peak-Density Measurement . . . . .	101
B.4	Transition Temperature . . . . .	103
B.5	BEC Fraction . . . . .	104
<b>C</b>	<b>Magnetic Field Zeroing</b>	<b>105</b>

<b>D Ionization Electrode Design</b>	<b>107</b>
<b>List of Figures</b>	<b>107</b>
<b>List of Tables</b>	<b>124</b>



# Chapter 1

## Introduction

### 1.1 Historical Perspective

The study of Rydberg physics has had a long and rich history spanning more than one-hundred years. In 1890 [1] Johannes Rydberg, following the work conducted by Johann Balmer, presented a formula that could describe the spectrum of atoms beyond just hydrogen. Now known as the Rydberg formula, this equation describes the binding energy of an electron in an atom as a function of the principal quantum number  $n$  and the quantum defect  $\delta_l$ .

The quantum defect is dependent on an atom's orbital angular momentum and reflects a lowering of the electron energy due to the overlap of the electron and the ionic core [2, 3]. The larger the overlap, the larger the quantum defect. This is reflected in an increase of  $\delta_l$  with atomic number but also decrease with orbital angular momentum,  $l$  [4]. Spectroscopic measurements of the energy spectrum can lead to very accurate determinations of an atoms quantum defect [5–7].

In 1913 Niels Bohr introduced the so-called Bohr model of the atom [8] with which he described the quantized nature of the electron's energy-levels. Transitions between these levels were found to correspond to the spectral measurements of hydrogen. Bohr's model brought to light that the Rydberg formula describes the hydrogen electron's binding energy, as well as other atomic scaling properties such that the orbital size which scales as  $n^2$ .

One of the earliest investigations of perturbations of Rydberg energy level structure due to interactions was conducted in 1934 by Amaldi and Segré [9]. They saw shifts and broadenings

of transitions to high  $n$  for Na and K states contingent on the presence of other buffer gases. They found the broadenings and shifts depended on the density and species of atom introduced into the system. In the same year, Fermi posited a mean-field explanation of the observed phenomena [10], whereby he introduced the pseudo-potential and scattering lengths. The Rydberg wavefunctions of the high- $n$  states encompassed many neighboring atoms and Fermi surmised that each atom that scattered off of the Rydberg electron induced a shift dictated by the sign and magnitude of the s-wave scattering length between the electron and a buffer gas atom.

In 2000 Greene *et.al.* [11] theorized the existence of bound states between atoms and Rydberg states. They proposed that attractive scattering between an atom and the Rydberg electron could result in a potential whose shape mirrors that of the electron wavefunction. The anti-nodes of the wavefunction thus corresponds to potential wells in which nearby atoms can become trapped. Through ultracold atomic physics, the necessary densities and temperatures are accessible. Furthermore, they identified two classes of Rydberg molecules, nonpolar and polar. Molecules of the first class correspond to binding between an atom and a Rydberg states of low ( $l \lesssim 2$ ) orbital angular momentum and possess binding energies of order MHz. In contrast, polar Rydberg molecules consist of multiple, high- $l$ , degenerate states of negligibly small quantum defects. These so-called “trilobite” molecules posses kilo-Debye electric dipole moments and GHz binding energies. Other theoretical work has been done to calculate molecular potentials, wavefunctions, and dipole moments under the influence of  $p$ -wave shape resonances in electron-atom scattering [12–15]

To create Rydberg molecules, the presence of two (or more) nearby atoms is required. Thus, high-density atomic samples are required to yield inter-particle spacings comparable to the size of a Rydberg state enabling molecule production. Additionally, low temperature atomic samples are necessary such that the dominant energy scale is that of the molecular binding energies. With the advent of ultracold dense atoms samples, such as atoms in a Bose-Einstein Condensates (BEC), the density and temperature regimes require to produce Rydberg molecules became experimentally accessible [16–21].

In 2009, the first direct observations of Rydberg molecules were made by Bendkowsky *et.al.* [22] using Rb. These measurements were the catalyst for a slew of work over the

next decade. Developments include realizations of Rydberg molecules in Cs [23] and Sr [7]. Molecular Rb  $P$  [24] and  $D$  [25, 26] Rydberg states. Realizations of Trilobyte [27, 28] and butterfly state [29, 30] formation. Polyatomic states of Rb [31], where up to four ground-state atoms were observed to be bound to the molecular potential. In order to utilize molecular Rydberg states where long coherence times are necessary, a good understanding of the mechanisms by which these states decay is required. Several decay channels have been identified and studied such as radiative decay, blackbody radiation, collisions with the background, L-changing collisions, and associative ionization [32–43].

In this thesis I will discuss spectroscopic and decay measurements we have conducted on Rydberg atomic and molecular states of strontium. With increasing density, the number of ground-state atoms within the Rydberg wavefunction increases, and thus spectroscopic measurements are subject to interactions between the constituent particles. At densities of  $\sim 10^{14} \text{ cm}^{-3}$  we can vary  $n$  and in doing so, transition between a few- and many-body regime. We have developed a mean-field theory of the spectra in the many-body regime. Additionally, we have found great agreement with a polaronic description [44, 45] valid at any density and  $n$  which treats the Rydberg excitation as an impurity embedded in a deformable medium. We have also conducted studies of the decay mechanisms of molecular Rydberg states of Sr in the few- and many-body regimes.

## 1.2 Rydberg Atoms

A Rydberg atom is an atom with an electron in a highly excited state of principal quantum number,  $n$ . This equation yields an electron's binding energy as a function of its quantum state and can be extended to any atom via a quantum defect,  $\delta_l$  [46], which is dependent on orbital angular,

$$E_n = -R_M/(n - \delta_l)^2. \quad (1.1)$$

The correction a quantum defect introduces is implemented to account for shifts in energy caused by overlap of an electron's wavefunction and the ionic core. The larger the overlap, the larger the correction, hence a dependence on orbital angular momentum,  $l$ . With increasing

Property	$n$ Scaling	Sr $5s38s\ ^3S_1$
Binding Energy	$n^{-2}$	$1200 \text{ cm}^{-1}$
Lifetime	$n^3$	$21 \mu\text{s}$
Rydberg Radius	$n^2$	60 nm
Ionization Field	$n^{-4}$	$225 \text{ V cm}^{-1}$
Polarizability	$n^7$	$7 \text{ MHz cm}^2 \text{ V}^{-2}$

Table 1.1: List of scaling laws and values for Sr  $5s38s\ ^3S_1$ .

$l$ , the overlap diminishes such that high- $l$  are described by small quantum-defects. The proportionally constant is the Rydberg constant,  $R_y$ , corrected for the finite mass of the nucleus,

$$R_M = R_y / (1 + m_e/M) \quad (1.2)$$

where  $m_e/M$  is the electron to nuclear mass ratio.

In addition to values of binding energy, Rydberg atoms maintain a strong scaling of many properties as a function of  $n$ . Table 1.1 presents some of these properties along with their absolute values for the  $5s38s\ ^3S_1$  state, as an example.

### 1.3 Rydberg Molecules

So far, I have described properties of an isolated Rydberg atom, in this work I will describe how the presence of neighboring ground state atoms changes the spectral landscape. Through attractive scattering between Rydberg electron and nearby atoms, bound states can emerge [11]. Through a Fermi pseudo-potential averaged over the electron wavefunction a potential arises between the Rydberg and an atom that is proportional to the product of the scattering length and the Rydberg electron density. Therefore, given attractive scattering, an atom can be trapped in the anti-nodes of the Rydberg wavefunction. For our experiments, we will drive transition from the Sr ground state to  $5sns\ ^3S_1$  lines which are isotropic. Since the Rydberg radius increases in size as  $n^2$ , so too does the corresponding molecule. In the case of  $n = 38$ , this results in a molecule  $\sim 100$  times the size of a water molecule!

Rydberg molecules themselves can exist in excited vibrational states [22]. In addition,

it is also possible to bind more than one atom to the Rydberg molecular potential as first demonstrated by Gaj *et.al.* [31], where binding of up to five particles was observed. Thus a zoo of molecular states is possible where multiple atoms can bind and each be in various vibrational states [44, 47].

## 1.4 Thesis Organization

This thesis is structured in the following manner. Ch. 2 discusses the trapping and cooling scheme implemented to achieve Sr atomic samples at the temperatures and densities necessary to conduct the experiments presented. Ch. 3 delves into how we drive atoms to Rydberg states and subsequently detect their presence. Then in Ch. 4, I discuss how the Rydberg molecular potential arises from electron-atom scattering, and introduce the spectral measurements that span the few- and many-body regime, which are analyzed in detail in later chapters. The decay mechanisms and associated rates of Rydberg states are explored in Ch. 5. Then, a mean-field description of the spectra in the many-body regime is presented in Ch. 6. Finally, in Ch. 7, I discuss the impurity-physics description of a Rydberg excitation which serves as a fully quantum-mechanical theory, valid in both the few- and many-body regimes.



# Chapter 2

## Cooling and Trapping $^{84}\text{Sr}$

The experiments described in this thesis are performed using ultracold samples of  $^{84}\text{Sr}$  in either a thermal or BEC phase. To obtain such samples, we go through multiple stages of laser cooling and trapping. First, we utilize the 461 nm  $(5\text{s}^2)^1\text{S}_0 \rightarrow (5\text{s}5\text{p})^1\text{P}_1$  broad-line transition to reach 1 mK (Fig. 2.1) in a Magneto-Optical Trap (MOT) in combination with a magnetic trap [48]. Subsequently we load a narrow-line MOT using the 689 nm  $(5\text{s}^2)^1\text{S}_0 \rightarrow (5\text{s}5\text{p})^3\text{P}_1$  transition cooling down to 2  $\mu\text{K}$  [49]. Finally, a recycled-beam optical dipole trap (ODT) [50, 51] is turned on, which can trap millions of atoms at 2 mK. We conduct experiments at this stage but may also choose to begin an evaporative cooling trajectory which results in BEC samples of several hundred thousand atoms.

### 2.1 Broad-Line Trap

Room temperature strontium is a metallic solid. As such, we load strontium into an ‘oven-nozzle’ which is heated to 425 °C, metallic pellets sublime resulting in gaseous strontium emitting from the nozzle with a mean velocity of about 450 m/s. We achieve trapping of these atoms by employing the 461 nm transition in three stages (Fig. 2.2): a 2D-Collimator, a Zeeman Slower, a broad-line MOT (all using the 461 nm, 30.5 MHz wide transition). Additionally, there is a decay path to the magnetically trappable  $^3\text{P}_J$  manifold from the  $^1\text{P}_1$  line. These atoms are collected by the quadrupole MOT field and are repumped back to the ground state for further cooling using the 481 nm  $(5\text{s}5\text{p})^3\text{P}_2 \rightarrow (5\text{p}^2)^3\text{P}_2$  transition.

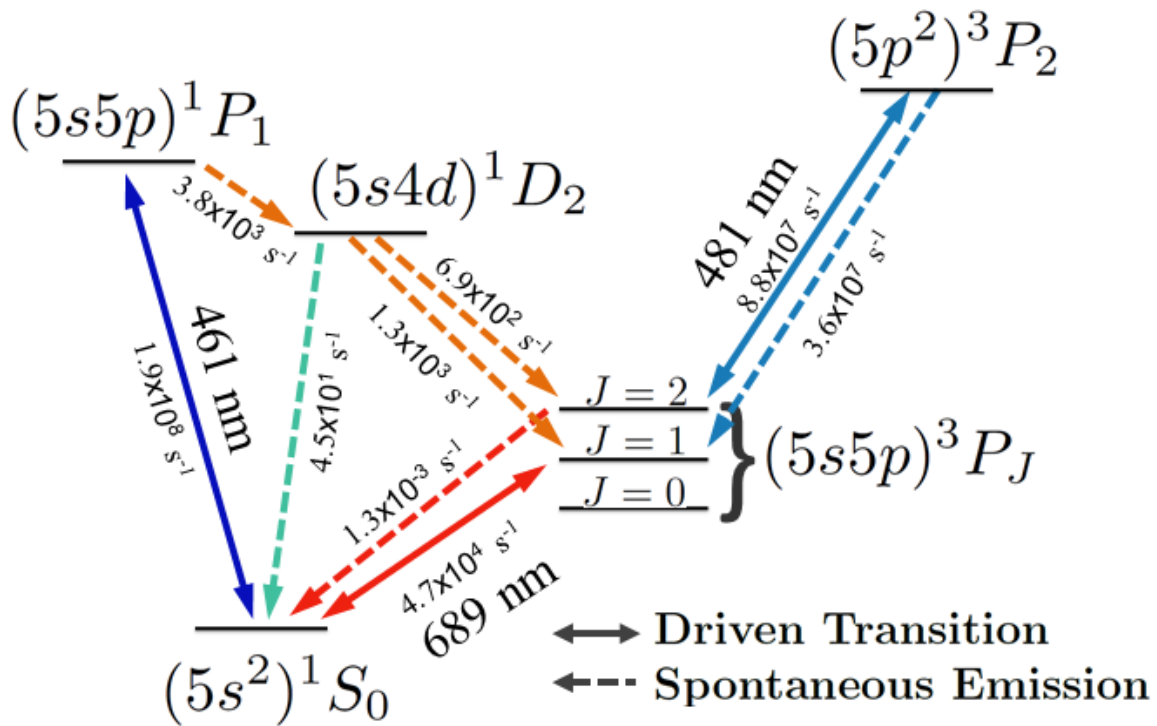


Figure 2.1: Energy level diagram of strontium.

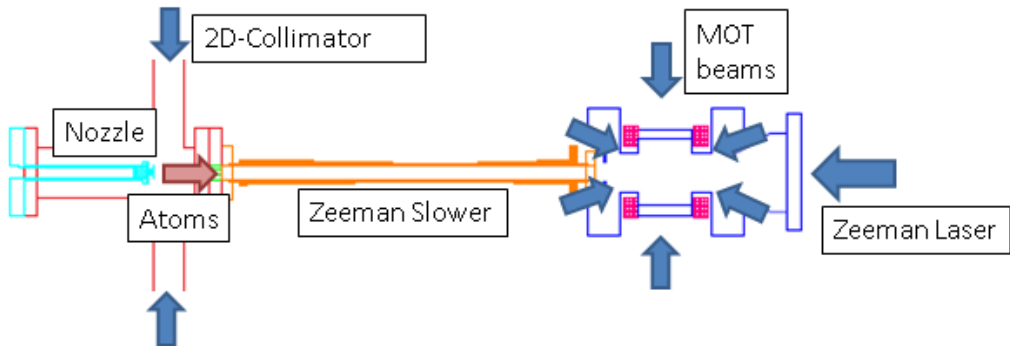


Figure 2.2: Schematic of 461 nm cooling and trapping stages. Shown is the oven-nozzle (light-blue), 2D-Collimator (red), Zeeman Slower (orange), MOT chamber (dark blue), MOT coils (pink), and arrows indicating the atom-beam propagation direction (red arrow) and 461 nm beams (blue arrows).

Immediately following the output of the oven, a 2D-Collimator cools the atoms via optical molasses in the radial direction. A retro-reflected beam incident on the atoms in two orthogonal directions perpendicular to the direction of the atom-beam propagation is used. By cooling in the transverse direction, we greatly increase the flux of atoms that will enter the trapping region of the MOT. We observe approximately an order-of-magnitude increase in the loading rate of the MOT with the inclusion of the 2D-Collimator red-detuned by half the natural linewidth.

Next, the atomic beam enters the Zeeman Slower where the mean axial velocity is reduced from about 450 m/s to about 30 m/s, slow enough for the MOT to capture. Using an acousto-optical modulator (AOM), the Zeeman laser beam is red-detuned by 18 times the natural linewidth of the transition in order to avoid scattering in the region of the MOT, therefore a spin-flip configuration is implemented such that somewhere along the path of the Zeeman slower the direction of magnetic field is reversed. The relative direction of Zeeman Slower fringe field compared to the on-axis field of the MOT can have a significant impact. We find that an anti-parallel configuration is optimal by a factor of  $\sim 2$ .

The output of the Zeeman Slower leads to the MOT region. The MOT light is set at a red-detuning of 1.8 times the linewidth of the 461 nm transition. A large loss channel is present due to decay from the  $(5s5p)^1P_1$  state to  $(5s4d)^1D_2$  and subsequently to the  $(5s5p)^3P_{1,2}$  states. However, the low-field seeking  $^3P_2$  states are trapped by the anti-Helmholtz magnetic field of the MOT. These atoms can therefore be reintroduced into the main cycling transition by repumping with a 481 nm laser to the  $(5p^2)^3P_2$  state. Experimentally we find that it is optimal to repump for 50 ms after having loaded the magnetic trap for several seconds instead of having the repump beam on during the whole loading procedure. Details of the repumping laser can be found in Pakorn Wongwaitayakornkul's undergraduate thesis.

For a 2 s load time, this scheme yields  $20 \times 10^6$  atoms of  $^{84}\text{Sr}$  near the Doppler temperature limit. Although  $^{84}\text{Sr}$  is the least abundant isotope, at 0.6%, and we could instead generate much larger MOT sample with the other isotopes, we chose to use  $^{84}\text{Sr}$  for these experiments due to the  $123a_0$   $^{84}\text{Sr}$ - $^{84}\text{Sr}$  scattering length, which is ideal for evaporative cooling. More details on our broad-line cooling and trapping scheme, including a description of the 461 nm laser system, can be found in Ref. [48].

## 2.2 Narrow-Line Trap

Having produced a trapped gas of ten's of millions of atoms at about 2mK, the next stage of cooling consistses of a narrow-line MOT. Utilizing the  $(5s^2)^1\text{S}_0 \rightarrow (5s5p)^3\text{P}_1$  transition enables us to reach a much colder temperature because of a reduction in line-width of over three orders of magnitude compared to the broad-line MOT. The theoretical temperature limits due to the Doppler limit and atom recoil are comparable at about 200 nK, however, experimentally we only cool to about 1  $\mu\text{K}$  which is sufficient to subsequently transfer atoms to the ODT.

To bridge the gap between broad-line MOT and initial ODT temperaures, the narrow-line MOT must capture  $\sim 2$  mK atoms and cool them to  $\sim 1 \mu\text{K}$ . To achieve this, we dynamically change the trap parameters. Initially, the narrow-line MOT begins with large laser intensity compared to the saturation intensity, far red-detuning compared to the transition line-width, and a dither of the laser frequency that is also large compared to the line-width. This ensures that the initial range of atom velocities at the end of the broad-line MOT will experience cooling and trapping on the 689 nm transition. As cooling takes effect and temperature falls, these experimental parameters follow suit and are changed to address a narrower velocity distribution, ultimatly yielding  $\sim 1 \mu\text{K}$  samples of about two million atoms. Details of our narrow-line cooling MOT can be found in Ref. [49].

## 2.3 Optical-Dipole Trap

We load atoms from the narrow-line MOT into a 1064 nm infra-red (IR) ODT with two perpendicularly crossed paths (Fig. 2.3). Each path is made up of three laser beams co-propagating with 10's of microns of separation [52], yielding a ‘Top-Hat’ laser profile. After loading the Top-Hat ODT, the intensity of the outer two beams linearly decrease to zero over 400 ms while maintaining constant intensity in the center. At this juncture,  $\sim 10^6$  atoms at  $\sim 2 \mu\text{K}$  are trapped in the ODT and represent a cold thermal sample which we have used for several of our measurements. Further cooling via forced evaporation can be employed, which enables an increase in phase-space density sufficient enough to create Bose-Einstein

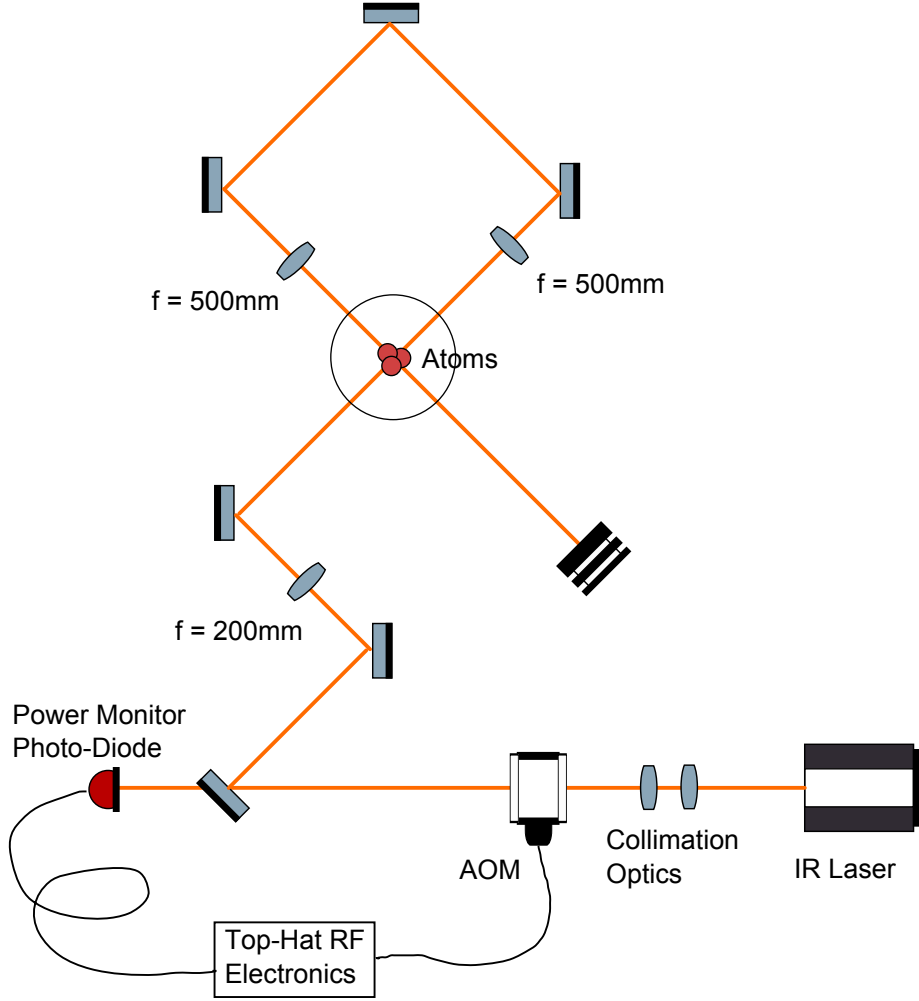


Figure 2.3: Schematic of optical setup used to generate ODT recycled beam configuration. Made using image library created by Alexander Franzen.

condensates (BEC) of  $^{84}\text{Sr}$  [19, 20]. We produce samples where 75% of trapped atoms are in the BEC phase. Several hundred thousand atoms enter the condensate phase at a peak number density of  $\sim 4 \times 10^{14} \text{ cm}^{-3}$ .

The Top-Hat ODT was a project completed by Germano Woehl Jr. We generate the three Top-Hat beams by driving an AOM at three different frequencies. The difference in frequencies sets the angular separation of the diffracted orders. The RF frequencies and amplitudes are calibrated by examining the beam profile on a CCD camera and ensuring an approximately flat top at sufficient intensity. Fig. 2.4 shows the beam profile with and without driving the frequencies corresponding to the outer beams. The absolute value of

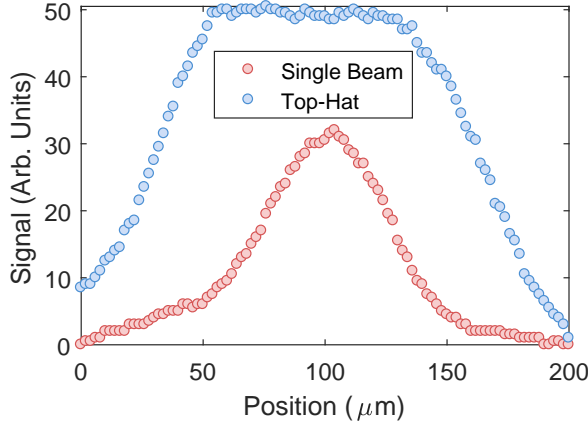


Figure 2.4: Traces of ODT beams before and after converging to a single beam.

frequencies are chosen to ensure a constant value of intensity at the center over a sufficiently large area. Fig. 2.3 shows the schematic of the RF setup used to drive the AOM. We feedback to a voltage-controlled attenuator (VCA) labeled VCA-2 in Fig. 2.3 using the measured power of all three diffracted beams. In this way, we power-lock to the total power. A separate VCA is used after combining the voltage-controlled oscillators (VCO) corresponding to the minimum and maximum center-frequencies used. In other words, this additional VCA (labeled VCA-1 in the schematic) controls the power of the outer beams of the Top-Hat relative to the center beam.

## 2.4 $^{84}\text{Sr}$ BEC Production

Once the Top-Hat phase is complete, whereby the power in the two outer beams has been linearly reduced to zero, we initiate a force-evaporation trajectory. We follow the prescription layout by O'Hara *et.al.* [53], where the trap depth dynamically changes as

$$V_0(t) = V_0(0) \left(1 + \frac{t}{\tau}\right)^{-2(\eta' - 3)/\eta'} \quad (2.1)$$

where  $V_0(0)$  is the initial trap depth,  $\tau$  is a time constant, and  $\eta'$  reflects the ratio between potential depth and temperature. The initial trap depth is chosen such that the initial equilibrium cloud temperature matches that of the narrow-line MOT final temperature. We follow an evaporation trajectory using  $\tau = 250\text{ ms}$  and  $\eta' = 16$  which we arrive at through

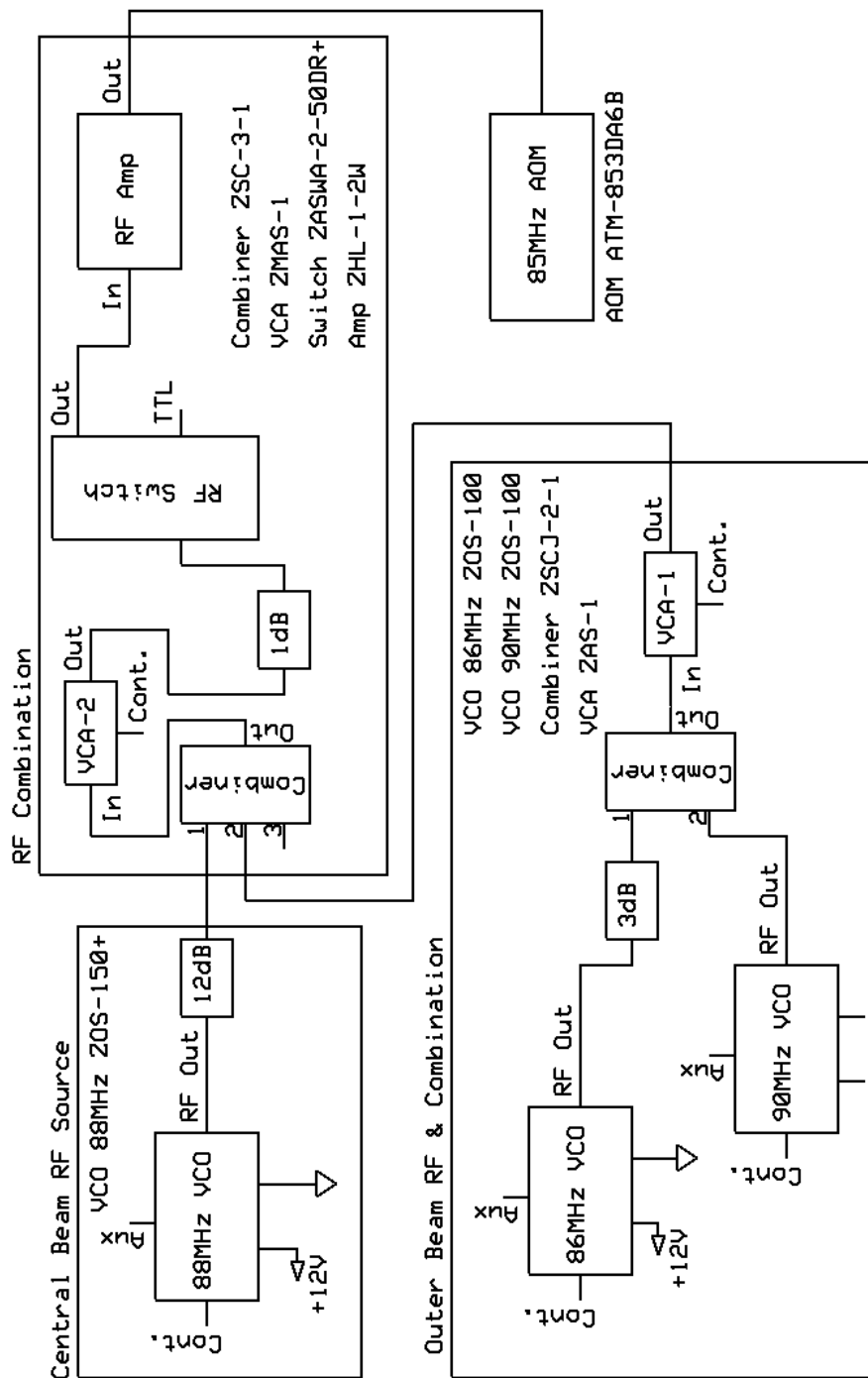


Figure 2.5: Schematic of RF components used to generate Top-Hat trap in combination with an IR AOM.

iterative optimization. Transition to the BEC phase occurs at 400 nK (See Appendix B.4).

Now I present comparative data of BEC production with and without the Top-Hat compression stage before evaporation. Figs. 2.6 and 2.7 show time-of-flight (TOF) atom images and fits at various times during an evaporation trajectory using a single beam at all times. Figs. 2.8 and 2.9 show the same evaporation trajectory preceded by a Top-Hat phase. The difference in BEC production is drastic. Fig. 2.10 shows the extracted fit parameters in either scenario. Implementing a Top-Hat phase results in BEC samples with population nearly twice as large with higher purity at comparable temperature.

The confluence of these cooling and trapping techniques allow us to produce sufficiently large and cold samples of  $^{84}\text{Sr}$  for use in the experiments described in the following chapters.

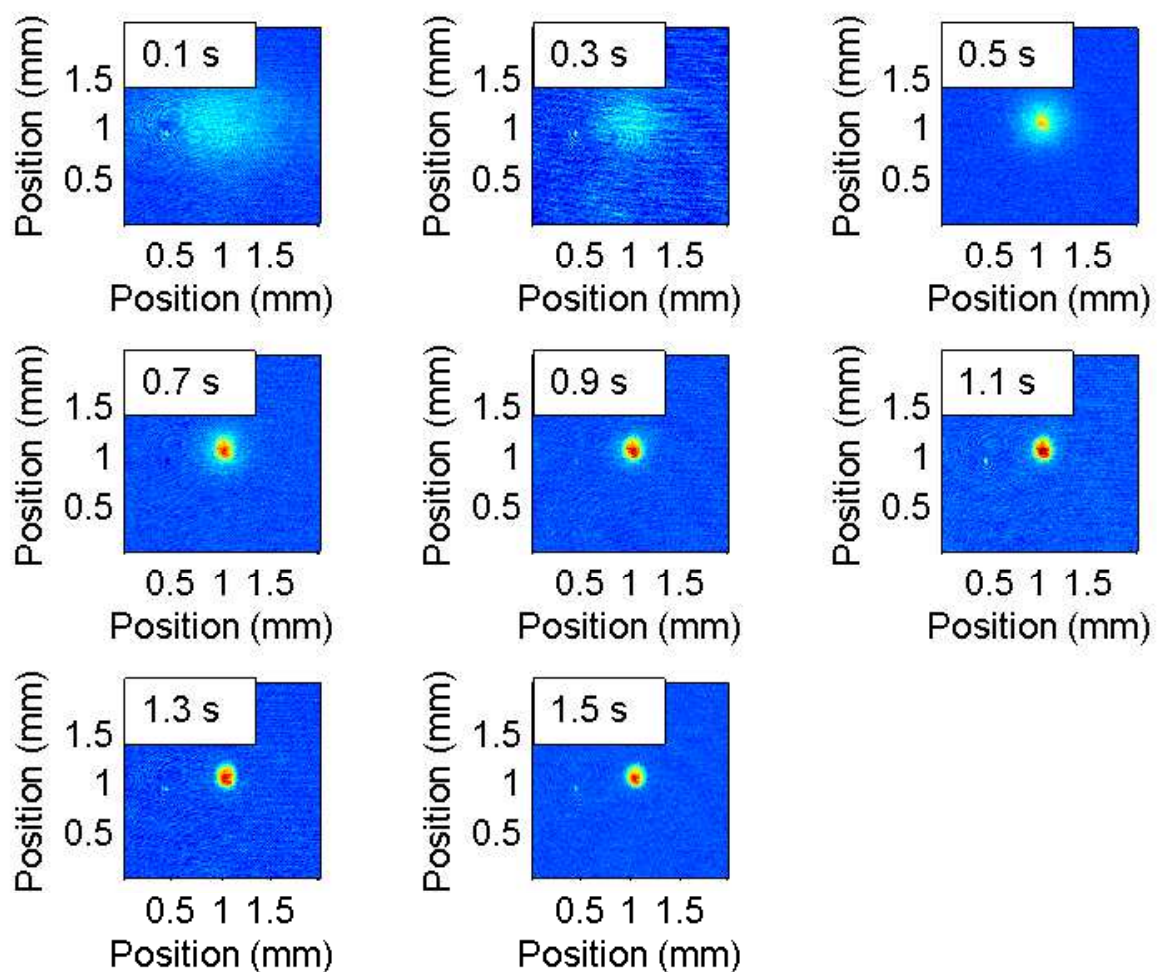


Figure 2.6: TOF atom images in at various times during evaporation in the absence of a preceding Top-Hat phase.

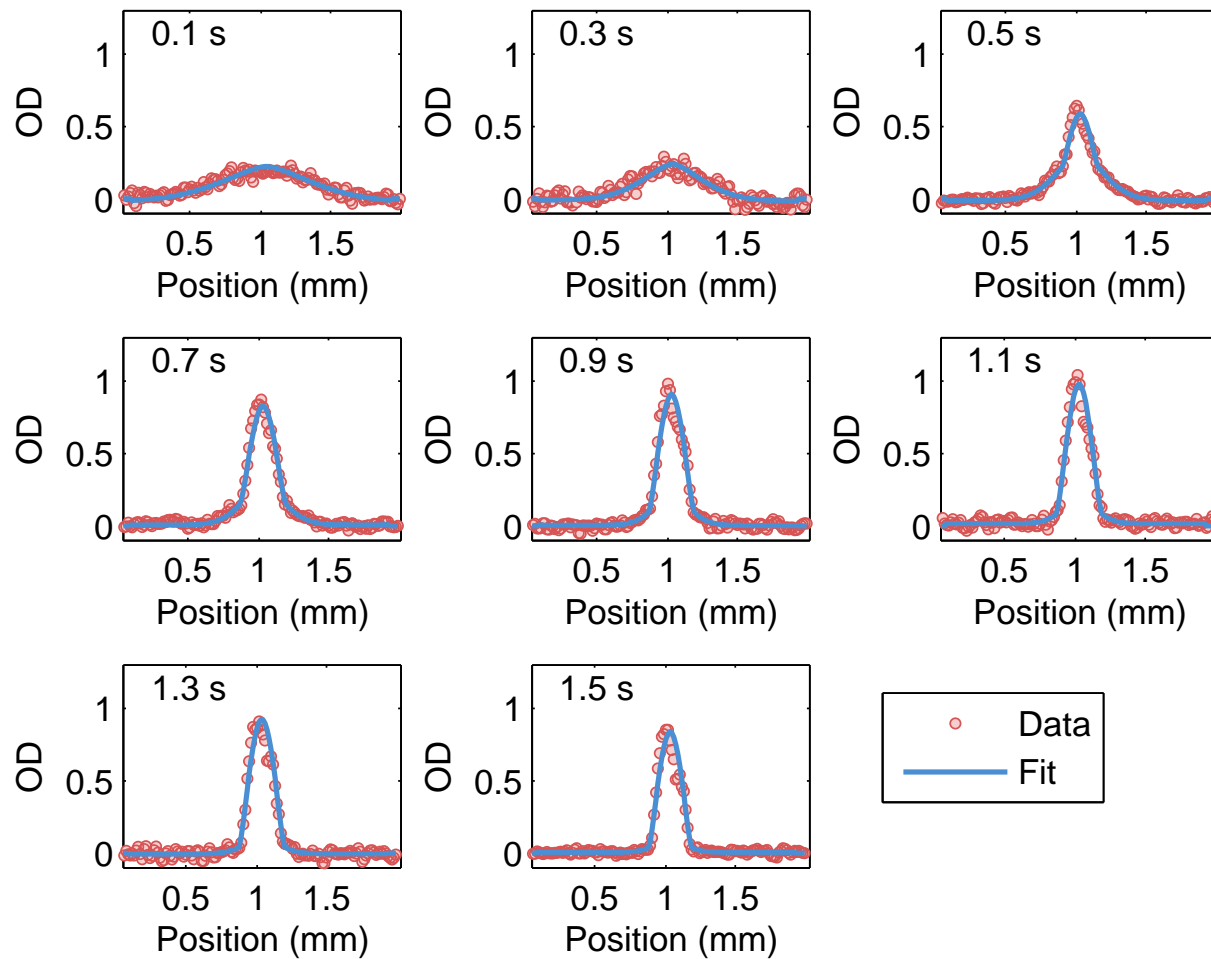


Figure 2.7: One dimensional slices of atom images from Fig. 2.6, and fits.

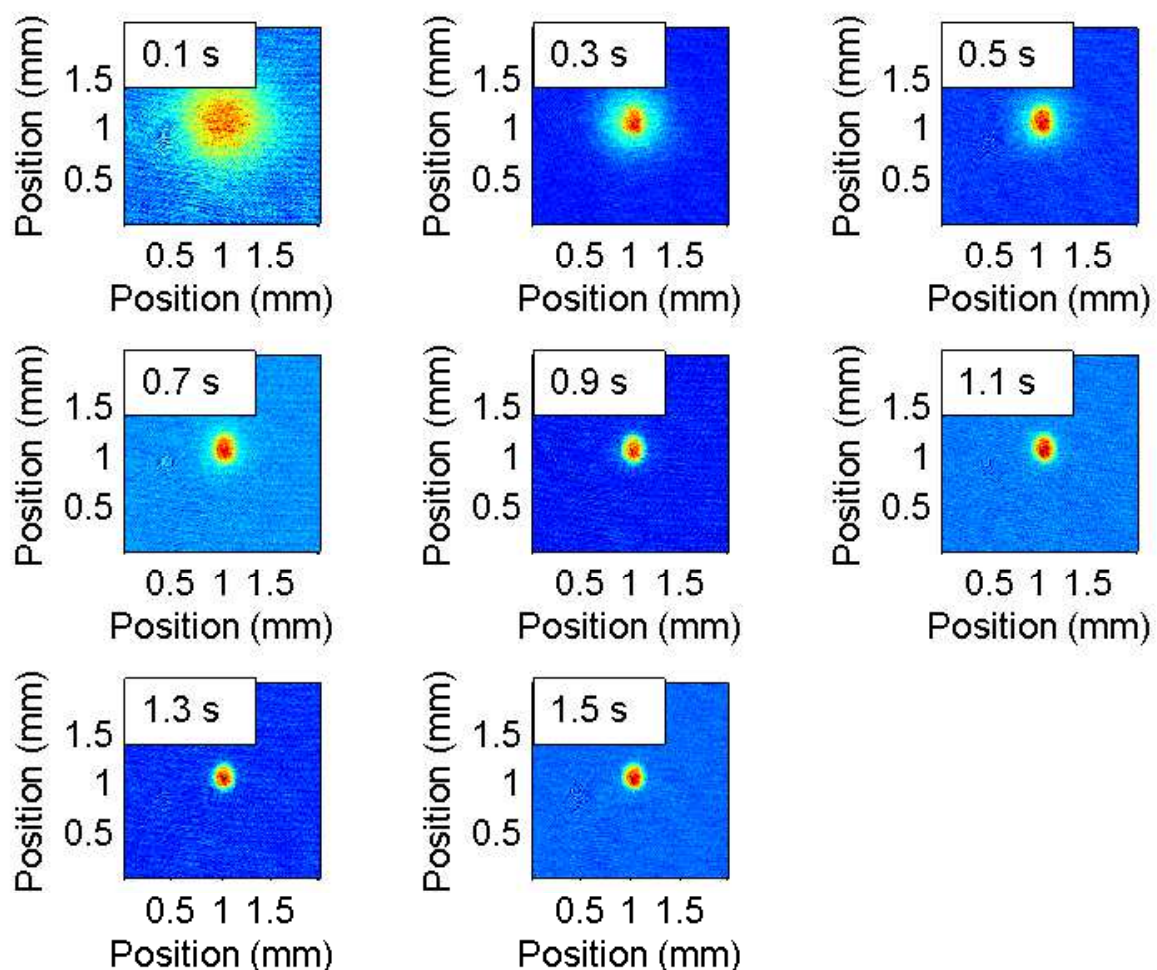


Figure 2.8: TOF atom images in at various times during evaporation following a Top-Hat phase.

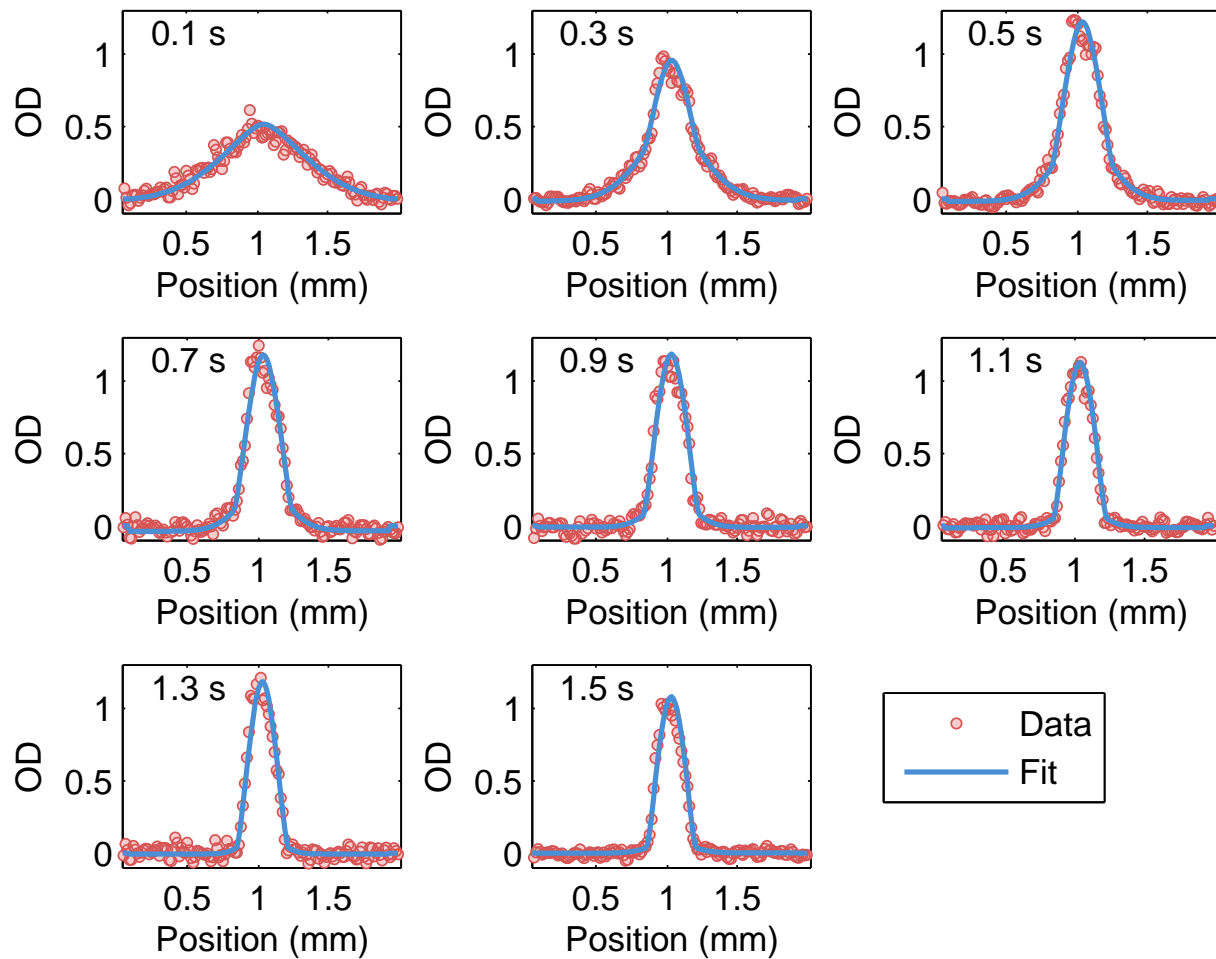


Figure 2.9: One dimensional slices of atom images from Fig. 2.8, and fits.

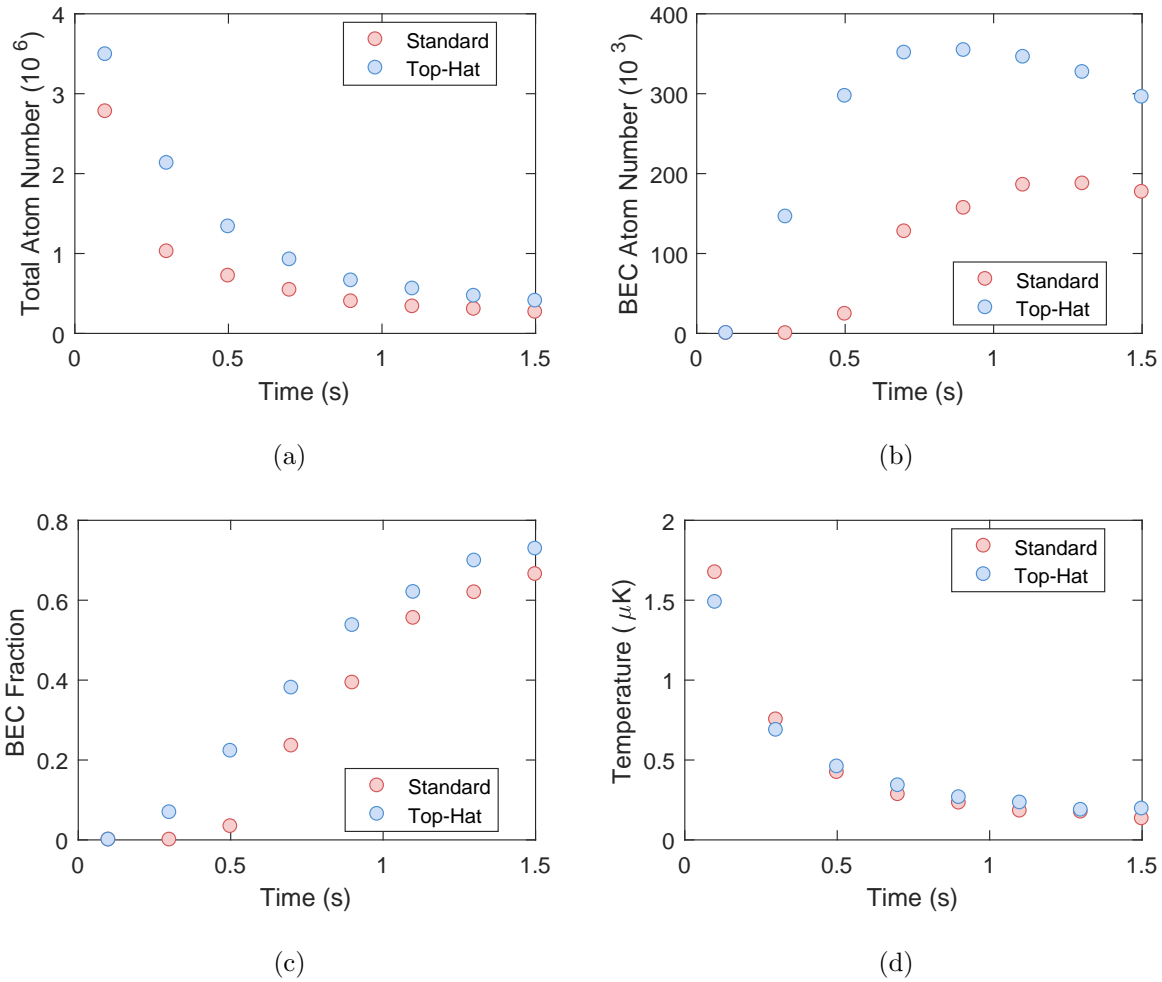


Figure 2.10: A comparison of BEC production with and without the use of the top-hat trap. (a) Total number of atoms as a function of time. (b) Number of condensate atoms. (c) BEC fraction. (d) Thermal temperature.



# Chapter 3

## Rydberg State Creation and Detection

### 3.1 Driving Rydberg Transitions

For these experiments we drive atoms from the ground state to  $(5snp)^3S_1$  Rydberg states via two-photon excitation. The  $(5s5p)^3P_1$  level is used as the intermediate state due to it's low scattering rate derived from the narrow linewidth. Additionally, the 689 nm laser is blue-detuned by 80 MHz to decrease scattering on the intermediate transition. The sign in detuning direction is chosen to avoid photoassociation lines [54]. Fig. 3.1 shows the level diagram of these transitions.

The 689 nm light that drives Rydberg transitions is derived from the same laser used for narrow-line cooling. On the output of the laser, 4 mW of light is picked off and sent to an AOM to set the 80 MHz blue detuning. Next, the beam passes through a half-wave plate and is then fed into an optical fiber that outputs to the atoms. The wave-plate ensures correct polarization alignment, which can be cleaned up on the output of the fiber with the help of a polarizing beam-splitting cube. The beam will be turned on for a few  $\mu\text{s}$  at a time during experiments and it is therefore important to align into the fiber for this situation. Heating of the AOM due to the RF signal will affect beam pointing and thus alignment into the fiber. So continuous-wave operation and pulsed operation are not optimized with the same alignment. For precise detuning, we use an RF synthesizer. It is also important to

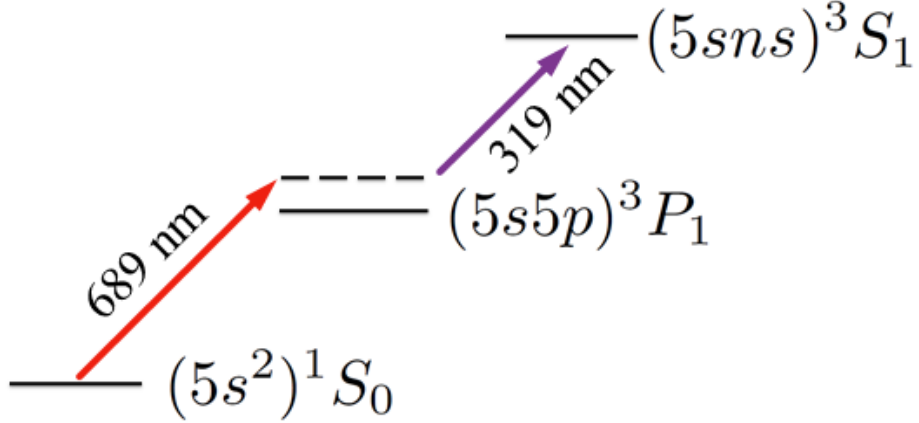


Figure 3.1: Relevant energy level diagram of strontium for two-photon Rydberg transitions.

have a good AOM extinction ratio to assure that Rydberg transitions are only being driven when intended and not due to unwanted leakage light. Similarly, one must be thorough in eliminating any sources of stray light. With the beam linearly polarized, we drive the  $m = 0$  transition.

From the output of a Toptica second-harmonic generation cavity, we obtain up to 300 mW of UV light with a 400 kHz linewidth, which we use to drive the  $(5s5p)^3P_1 \rightarrow (5sns)^3S_1$  transition. Because we drive the  $m = 0$  intermediate state, to drive the allowed  ${}^3S_1$ ,  $m_j = \pm 1$  states we employ circularly polarized UV light<sup>1</sup>. With knowledge of the quantum defect, we can find the atomic line of any particular state of interest. Fig. 3.2 shows a fit to a variety of  $ns$  states from which we extract a value of the quantum defect for strontium;  $\delta = 3.3721$ . This result expands on the range of previous measurements [7]. A detailed description of our 319 nm photon generation scheme can be found in Brian DeSalvo's PhD thesis [55].

## 3.2 Rydberg Signal Detection

We count Rydberg excitations through a combination of selective-field ionization (SFI) and charged particle detection [22–25, 27, 31, 56]. We employ SFI using electrodes within the vacuum chamber to dynamically drive an electric field and ionize Rydberg states within

---

<sup>1</sup>In spite of the transition being electric dipole allowed, zero overlap of spin part of the wavefunctions disallows the  $m = 0 \rightarrow m = 0$  transition

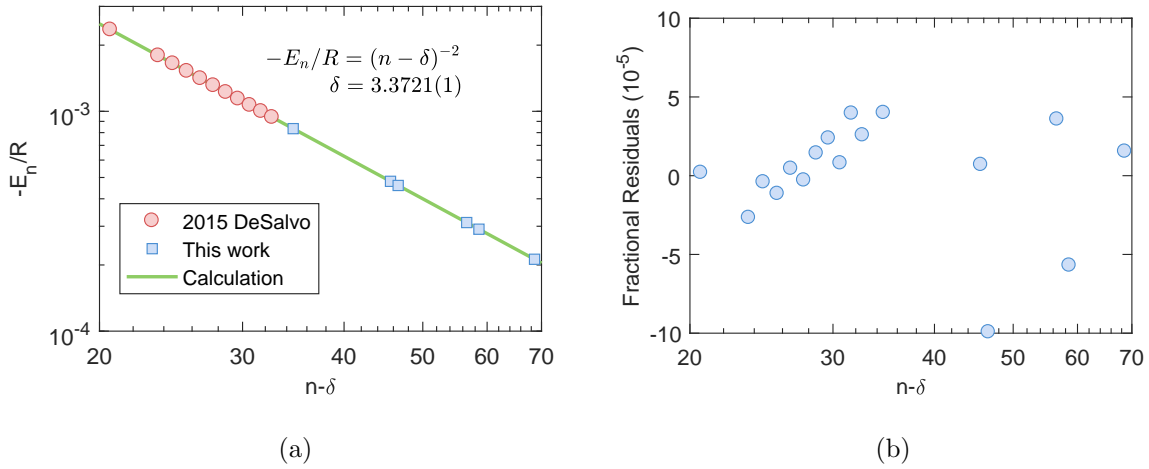


Figure 3.2: (a) Measured energy of  $5sns^3S_1^{84}\text{Sr}$  states. (b) Corresponding fractional fitting residuals.

an atomic sample. Subsequently we employ charged-particle detection on a micro-channel plate (MCP) detector to retrieve a signal proportional to the number of excitations created in the sample. The electrodes yield electrons, which are then guided by the net electric field towards the detector. The MCP generates pulses, which are then recorded using a multichannel scalar. When an atom in a sample is excited to a Rydberg state we want to measure its presence with good fidelity, though our detection efficiency is about 20%, our apparatus yields an adequate signal-to-noise ratio.

### 3.2.1 Electric Field Ionization

For qualitative understanding of the electric fields needed, here I derive the classical ionization field result. We begin by considering the potential of an electron in the presence of a positive ionic core and an external uniform field,

$$V(\mathbf{r}) = -\frac{e^2}{4\pi\epsilon_0 r} + eFz. \quad (3.1)$$

The first term is the Coulomb potential for an electron of charge  $-e$ , an ionic core of charge  $e$ , and where  $\epsilon_0$  is the vacuum permittivity. The second term is the potential energy of an external field of amplitude  $F$ , along the cardinal direction  $z$ . Fig. 3.3 plots this potential at various values of  $F$ , additionally the plot shows the binding energy (Eq.1.1) of an  $n = 20$

hydrogenic state. Graphically, the value of field needed for ionization,  $F_{\text{Adi}}$ , corresponds to the trace where an electron with an energy equal to the binding energy is unbound. We solve for  $F_{\text{Adi}}$  in the following way. We equate the binding energy to the value of potential at the saddle point,  $z_0 \propto -\sqrt{1/F}$ . The potential at this location is  $V(z_0) \propto -\sqrt{F}$ . Setting this value of potential equal to the Rydberg formula results in the classical ionization field,

$$F_{\text{Adi}} = \frac{F_0}{16(n - \delta_l)^4}, \quad (3.2)$$

where  $F_0$  is the atomic unit of electric field.

However, this classical result is lacking in a few respects. Ionization also depends on  $|M_L|$  sublevels, the electric-field slew-rate [2, 46], and as will be discussed in Ch. 5, the presence of neighboring atoms. The slew-rate dictates the behavior of states traversing an avoided crossing in the Stark-map. The classical result corresponds to adiabatic passage while sufficiently large slew-rates result in diabatic ionization and an ionization field given by, given by

$$F_{\text{Dia}} = \frac{1}{9(n - \delta_l)^4}. \quad (3.3)$$

### 3.2.2 Selective Field Ionization

To generate the fields required for SFI, we have incorporated several electrodes within the vacuum chamber. Each electrode can be individually controlled such that we can apply a potential difference amounting to desired electric fields at the location of the atoms. To determine the value of electric field in the region of the atoms we employed SimIon software which solves the Laplace equation given the electrode voltages and geometry<sup>2</sup>.

We define  $\Delta\phi \equiv V^+ - V^-$  where  $V^+$  ( $V^-$ ) is the potential of the positive (negative) plates. Using the SimIon software we calculate the electric field in the region of the atoms as a function of  $\Delta\phi$ ,

$$F = 0.30\text{cm}^{-1}\Delta\phi. \quad (3.4)$$

Note that this is under a scheme where half the ionization electrodes will be pulsed to a positive value of potential, while the other half will be subject to a pulse equal in magnitude

---

<sup>2</sup>The SimIon configuration files and related work are located in the Killian Lab Drobo under Rydberg\Projects\Electric\_Field\_System\Electron Dection Simulation\Final\_Configuration

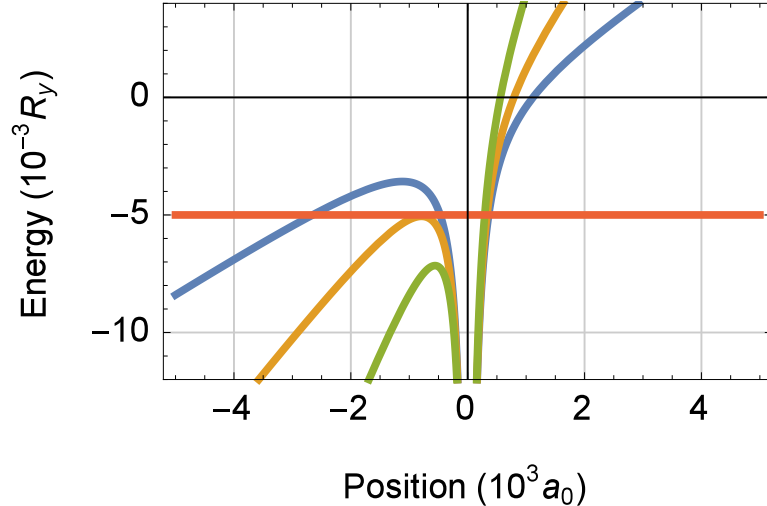


Figure 3.3: In red is the binding energy of an atom in the  $n = 20$  state. The other traces are the potentials experienced by an electron at different values of external electric field. In orange is the potential of an electron with an external field equal to the classical ionization field for  $n = 20$ . The blue trace is at half the same ionization field, and the green trace has an external field twice as strong compared to the ionization field.

but of opposite sign, as detailed in Fig. 3.4. We included three additional plates within the chamber to allow flexibility in controlling the path Rydberg electrons will take (12-14 in Fig. 3.4) *en route* to the detector. Electrodes 12, and 13 allow for vertical control of the electron path, while electrode 14 acts akin to a lens, focusing the the electron trajectory towards the MCP.

Experimentally we find that grounding plates 12-14 is optimal. However, this is not to say that they have no influence on the electrons, they still play an important role in shaping the potential landscape. More generally, it is important to be judicious in modeling the potential landscape of a proposed apparatus as diagnosing and resolving poor electron trajectory after-the-fact may prove problematic.

The last ingredient required is the ability to ramp the electrode potential values sufficiently and in an appropriate time-scale. Ideally, the potential ramps will be fast compared to the lifetime of the Rydberg states such that there is minimal state evolution during detection, however this detracts from the resolution of ionization spectra. We model the field

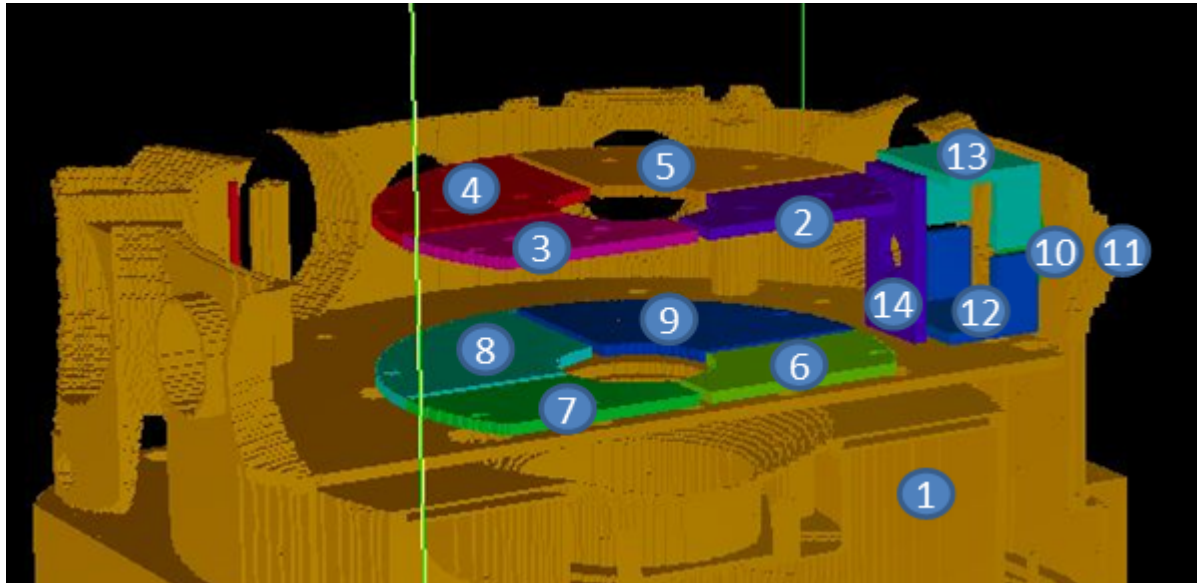


Figure 3.4: Layout of electrodes within our vacuum-chamber. 1 represents the chamber which sets ground. 10 is the MCP front-plate, 11 is the grounded MPC case. Atoms are in the geometric center of electrodes 2-9 which constitute the ionization electrodes. Plates 2, 5, 6, 9 are pulsed to positive voltages while 3, 4, 7, 8 are pulsed negatively. By doing so, the potential difference between the Rydberg electrons and the MCP is constant irrespective of the ionization fields and therefore the the states being ionized. Plates 12, 11, 13, 14 in these experiments always grounded. The front-plate of the MCP is set to 200V.

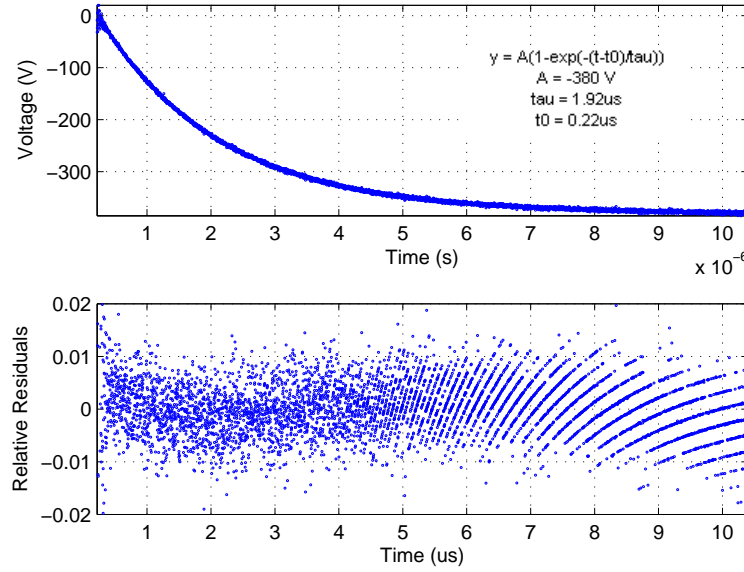


Figure 3.5: Electrode potential ramp measurement.

in the region of the atoms as

$$F(t) = F_0 \left( 1 - e^{-\frac{t-t_0}{\tau}} \right) \quad (3.5)$$

Where we fit to measurements of the  $\Delta\phi$  and extract  $\tau = 2.0 \mu\text{s}$ , the time-constant, and  $t_0 = 0.2 \mu\text{s}$ , a time-offset. The peak electric field,  $F_0$ , is chosen to be large enough to ionize the desired Rydberg states. Fig. 3.5 demonstrates a sample field-ramp profile. Because in these experiments we detect electrons, we assume a negligible flight-time due to their small mass. By mapping the time of arrival of the signal onto electric field, we can determine at what field excitations were ionized. Fig. 3.6 shows an example SFI spectrum obtained with 100 ns resolution converted to electric-field units. Note that due to the non-linear electric field ramps, SFI-profile data points will be unevenly distributed on the field axis.

### 3.2.3 Charged Particle Signal Detection

Utilizing 689 nm and 319 nm lasers we drive transitions from the ground state to Rydberg states of choice. Subsequently voltages on the electrodes are ramped up, and in doing so, the electric field ionizes any Rydbergs and directs resulting electrons towards the MCP. Out of the MCP, charge pulses are emitted and sent to an MCS discriminator.

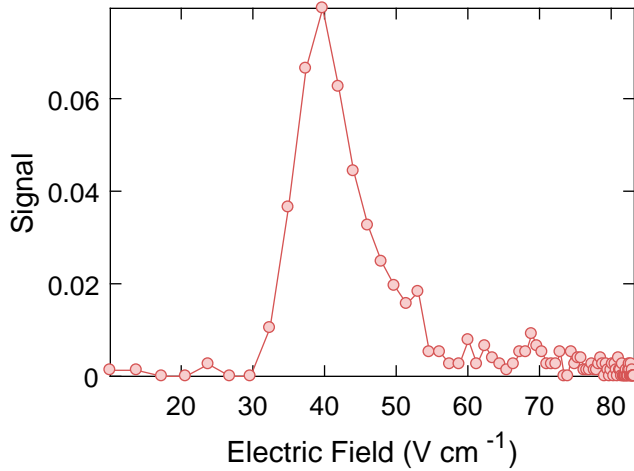


Figure 3.6: Sample charged particle signal after MCS discriminator with 100 ns resolution, plotted in electric-field units.

In order to ascribe proportionality between detection signal and the number of excitations in a sample, we must operate in a linear-response regime. There are multiple effects that can impede this effort, for example, a fast succession of Rydberg electrons can cause a problem at the MCP. Our MCP is made-up of two plates (chevron configuration), upon electron impact each one yields amplification via a cascade of electrons. A shower of electrons from the front-plates causes secondary emission once they arrive at the back-plate. However, each cascade depletes the plates, after which, they each take time to recharge. If not enough time has passed before a subsequent Rydberg electron arrives at the MCP, signal amplification is diminished which could result in a pulse being disregarded by the discriminator. Alternatively, inducing Rydberg blockade [57, 58] is another example of a non-linear regime where Rydberg-Rydberg interactions limit the production of Rydberg states.

We seek to enter a linear regime of operation prior to each unique experiment conducted. In other words, when experimental parameters change one must reaffirm that linear operation is maintained. We enforce linearity through the control of two of the knobs at our disposal; the excitation rate (controlled by laser intensity) and the excitation pulse duration. We vary each of these and looking for a roll-over in detection. Fig. 3.7 (a) depicts signal as a function 689 nm laser power at fixed pulse duration and UV laser power. Similarly, Fig. 3.7 (b) demonstrates a change in pulse duration at fixed laser powers.

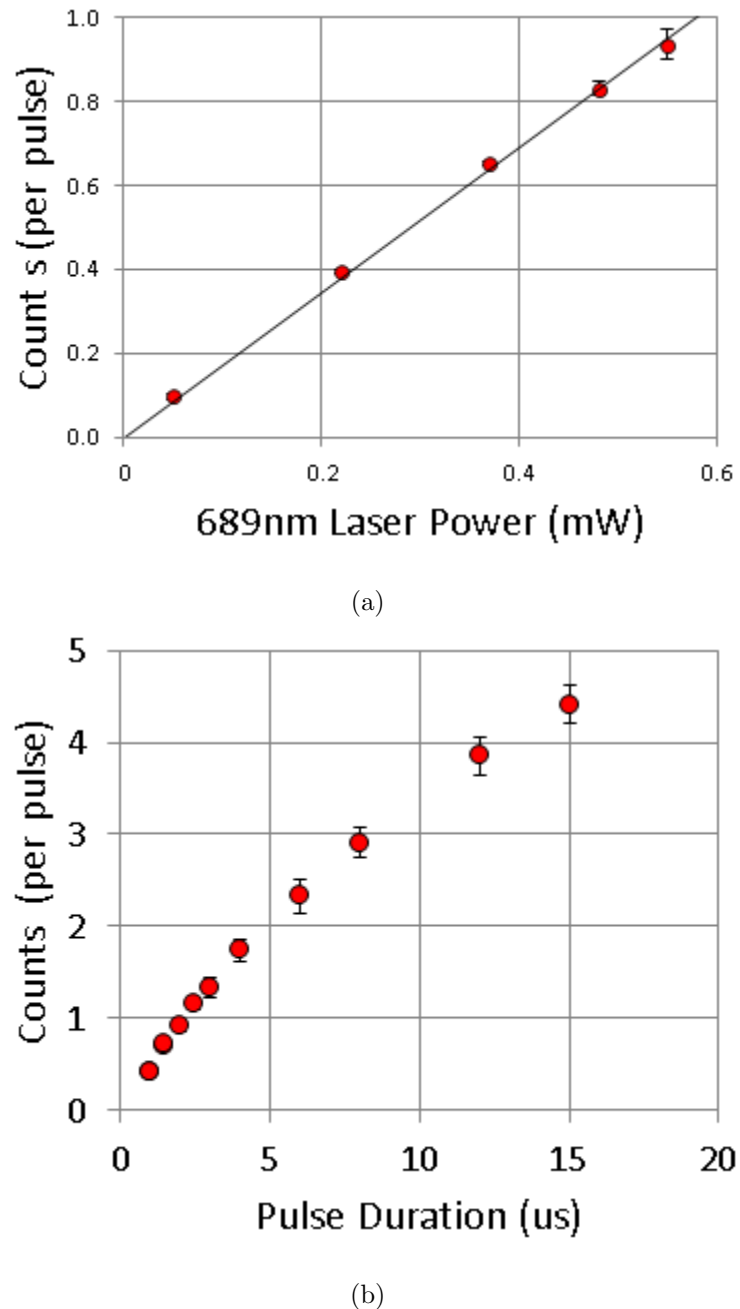


Figure 3.7: (a) For  $2\ \mu\text{s}$  long pulses and  $220\ \text{mW}$  UV power, signal response is linear across the available red laser power. (b) At fixed laser powers, roll-over is evident as a function of laser pulse time.

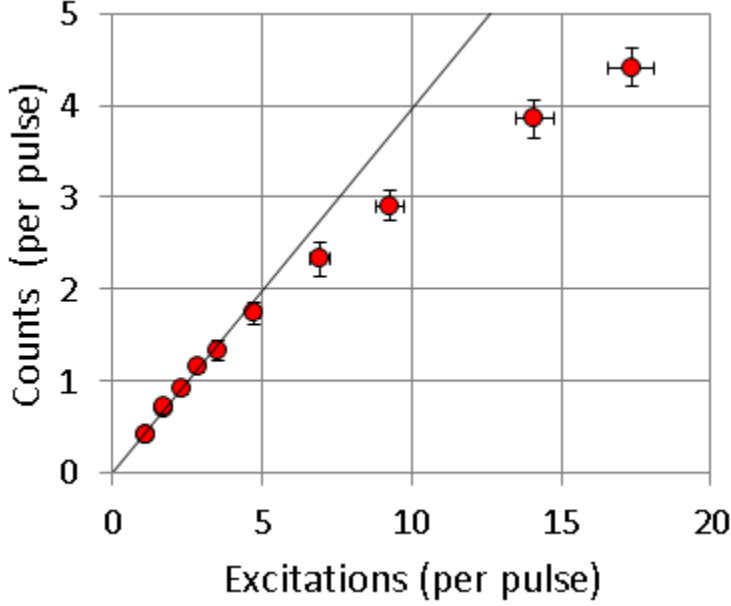


Figure 3.8: For low number of excitations per pulse, detection is linear up to about four excitations per pulse and corresponding to one count on the MCP.

To determine the rate of Rydberg excitation,  $\Gamma_{\text{Ryd}}$ , we measure the lifetime of a trapped strontium cloud with and without the presence of excitation lasers. Excitation to Rydberg states and subsequent ionization is a loss channel for ground state atoms and will be reflected in the atom number of the atom cloud. Though a single atom loss is too small to detect via imaging, we excite and ionize a single cloud thousands of times resulting in the loss of a comparable number of atoms. In this way we have a second method by which we count Rydbergs. More importantly, it circumvents any non-linearities that could arise from the charge-particle detection system. We then plot the results of each method against one another at variable excitation rate, Fig. 3.8. Rollover is evident above a count rate of more than one per pulse.

To generate a UV laser spectrum, the integral of an SFI profile (*e.g.* Fig. 3.6) is computed at a particular value of detuning and taken to be the amplitude of the spectrum at that frequency. The SFI profile represents the distribution of Rydberg states as a function of ionization field, therefore the choice of integration region selects which states to admit when generating a frequency spectrum.

Another way to asses whether or not one is operating in a linear regime is to look

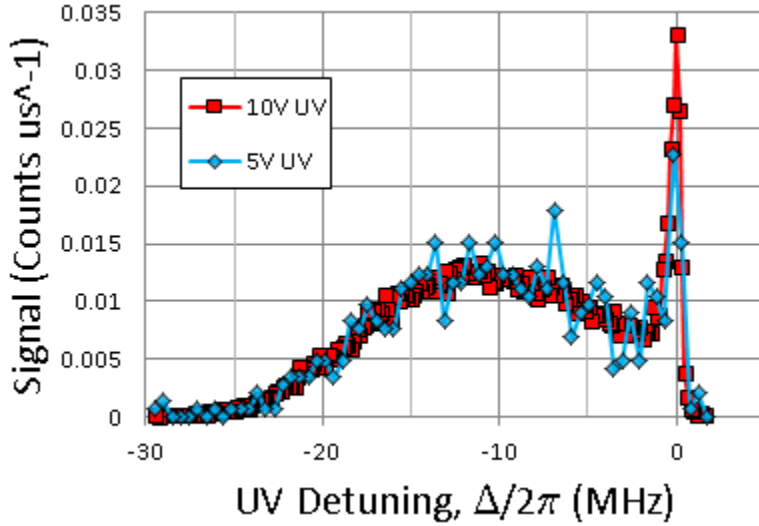


Figure 3.9: Here are two spectra each taken within the linear response regime. Between the two traces the UV power was changed, however shape invariance of the spectra is reflective of having taken the data in the linear regime.

for shape-invariance of spectra as a function of count rate. Fig. 3.9 demonstrates shape-invariance, whereby that same spectrum was measured at two values of UV laser power. After normalizing the spectra to have equal area, it is readily evident that the shape does not substantially change, though the signal-to-noise does. This is a good indicator that the higher value of power can be utilized without having to sacrifice signal quality yet still retain linear response. Additionally, this method has the advantage of being insensitive to any changes that could induce shifts. That is to say, when looking for signal extrema, one must not be deceived by mechanisms that induce a change in amplitude at a fixed frequency via shifts on the line.



# Chapter 4

## Few- to Many-Body Rydberg Molecule Regime

Formation of Rydberg molecules results from an attractive interaction of a Rydberg electron and one or more neighboring ground-state atoms [11]. A molecular potential emerges whose shape is dictated by the electron wavefunction. Nearby atoms can be trapped within the minima of this potential which correspond to anti-nodes of Rydberg wavefunctions. At sufficiently low  $n$ , the number of neighboring atoms found within a Rydberg orbital is  $\lesssim 1$ , thus spectra in this regime demonstrates a rich structure of discrete peaks corresponding to resolved molecular states. At increasing values of principal quantum number, a continuous many-body response emerges [44] where hundreds of atoms can bind.

### 4.1 Electron-Atom Interactions

We can describe electron-atom interactions using a Fermi pseudo-potential [10, 59] for the scattering between the Sr valence electrons at  $\mathbf{r}_i$  and a ground-state atom at  $\mathbf{R}$ ,

$$V_{\text{pseudo}}(\mathbf{r}_1, \mathbf{r}_2, \mathbf{R}) = \sum_{i=1}^2 \frac{2\pi\hbar^2 A_s(k(\mathbf{R}))}{m_e} \delta(\mathbf{r}_i - \mathbf{R}) + \frac{6\pi\hbar^2 A_p^3(k(\mathbf{R}))}{m_e} \overleftarrow{\nabla} \delta(\mathbf{r}_i - \mathbf{R}) \overrightarrow{\nabla}, \quad (4.1)$$

where the location of the Rydberg ionic core is assumed to be at the origin.  $A_s$  and  $A_p$  are the s- and p-wave scattering lengths, which depend on the relative momentum,  $k$ , and  $\hbar$  is the reduced Planck constant. These scattering lengths result from the phase-shift,  $\theta(k)$ ,

between the incoming and outgoing wavefunctions [29, 59, 60]

$$A_l(k) = -\frac{\tan(\theta_l(k))}{k^{2l+1}}. \quad (4.2)$$

Because Sr has no p-wave shape resonance, we can approximate the scattering lengths [7, 61] to be

$$\begin{aligned} A_s(k) &= A_s(0) + \frac{\pi\hbar^2\zeta}{3m_e e^2 a_0^2} k \\ A_p(k) &= A_p(0) \end{aligned} \quad (4.3)$$

where  $\zeta$  is the polarizability of the perturbing atom, with a measured value of  $\alpha_a = 186a_0^3$  [62]. The calculated value of the s-wave scattering length is  $A_s(0) = -18a_0$  [63]. Recent measurements have yielded  $A_s(0) \simeq -13.2a_0$ , and  $A_p(0) \simeq 8.4a_0$  [7].

The valence electron momentum can be calculated from a semi-classical kinetic energy calculation of a charged particle in a Coulomb potential and total energy equal to the Rydberg binding energy (Eq. 1.1),

$$\begin{aligned} E_n &= \frac{\hbar^2 k^2}{2m_e} - \frac{e^2}{4\pi\epsilon_0 R} \\ k(R) &= \sqrt{\frac{2m_e}{\hbar^2} \left( E_n + \frac{e^2}{4\pi\epsilon_0 R} \right)} \end{aligned} \quad (4.4)$$

The Sr wavefunction under a Born-Oppenheimer approximation [64], treats the motion of electron and atom nuclei separately such that for the valence electrons with a Rydberg core at the origin we write,

$$\Psi(\mathbf{r}_1, \mathbf{r}_2) \simeq \frac{1}{\sqrt{2}} [\phi_{5s}(\mathbf{r}_1)\psi_{ns}(\mathbf{r}_2) - \psi_{ns}(\mathbf{r}_1)\phi_{5s}(\mathbf{r}_2)] \quad (4.5)$$

where  $\phi_{5s}(\mathbf{r})$  is the wavefunction of the  $5s$  state for  $\text{Sr}^+$  ions and  $\psi_{ns}$  is the wavefunction of the  $ns$  Rydberg state. However, because the  $5s$  electron remains near the ionic core it does not appreciably alter the molecular potential such that a mean-field potential can be calculated as an effective one-electron system.

And so, for a given value of  $n$ , the electron momentum is a function of the electron position. Under first-order perturbation theory we arrive at the mean-field Rydberg molecular potential by averaging over the electron degree of freedom with the Rydberg core at the

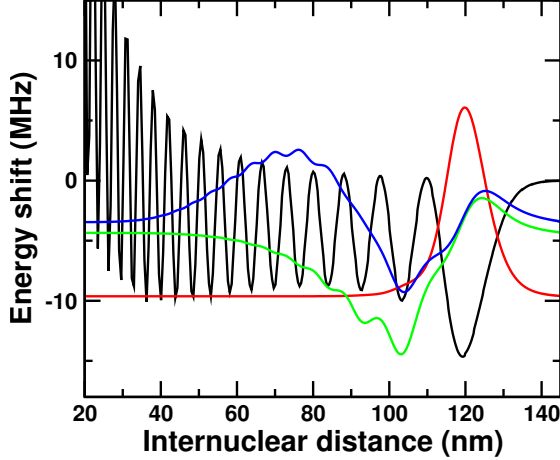


Figure 4.1: Calculated molecular potential (black) at  $n = 38$  and calculated wavefunctions for the  $\nu = 0$  (red), 1 (green), and 2 (blue) molecular vibrational states.

origin,

$$\begin{aligned} V_{\text{MF}}(\mathbf{R}) &= \int d^3r_1 d^3r_2 \Psi^*(\mathbf{r}_1, \mathbf{r}_2) V_{\text{pseudo}}(\mathbf{r}_1, \mathbf{r}_2, \mathbf{R}) \Psi(\mathbf{r}_1, \mathbf{r}_2) \\ V_{\text{MF}}(\mathbf{R}) &\simeq \frac{2\pi\hbar^2 A_s(k(\mathbf{R}))}{m_e} |\psi_{ns}(\mathbf{R})|^2 + \frac{6\pi\hbar^2 A_p^3(k(\mathbf{R}))}{m_e} |\nabla\psi_{ns}(\mathbf{R})|^2 \end{aligned} \quad (4.6)$$

Solving the associated Schrödinger equation results in molecular wavefunctions and their binding energies. Fig. 4.1 depicts the potential, the ground-state molecule wavefunction and the first two vibrational excited states with the zeros corresponding to their binding energies.

## 4.2 Spectroscopy Measurements

We use laser spectroscopy to measure the energy structure that arises from the molecular Rydberg potential. We carry out the experiments in samples sufficiently cold,  $\sim 100 \text{ nK} - 1 \mu\text{K}$ , such that the dominant energy scale is set by the molecular potential Eq. 4.6 and not the temperature of the atomic cloud. Note however that the UV laser linewidth of 400 kHz limits the width of features that we can resolve. Additionally, the sample density must be high enough,  $\sim 10^{13} - 10^{14} \text{ cm}^{-3}$ , such that the interparticle spacing is similar or smaller than the size of Rydberg wavefunctions of interest,  $\sim 100 \text{ nm}$ . Both of these conditions are met with either thermal or BEC samples we produce, as described in Ch. 2.

As described in Ch. 3, Rydberg states are excited by driving the  $5s^2 \ ^1S_0 \rightarrow 5s5p^3P_1 \rightarrow$

$5sns^3S_1$  two-photon transition using 689 nm and 319 nm light. Through SFI and charge-particle detection we can subsequently count the number of excitations in the sample. To then generate a spectrum we repeat the measurements at variable UV laser frequencies. Typical intensities of the excitation beams are  $20 \mu\text{Wcm}^{-2}$  and  $0.5 \text{mWcm}^{-2}$  for the 689 nm and 319 nm beams, respectively. These are kept low such that Rydberg blockade effects are absent. The Rydberg excitation rate is kept below one per pulse. We collect data by pulsing the excitation beams between  $2 \mu\text{s}$  and  $10 \mu\text{s}$  at a 4 kHz rate. Signal from  $10^3$  pulses is acquired at each frequency for each atom sample. The atom loss during each pulsing sequence is minimal such that the density varies by  $\sim 5\%$ . In addition to spectral measurements, we separately measure atom number, temperature, and trap frequencies through TOF atom image analysis.

The molecular formation rate, and therefore the relative spectrum feature amplitudes, can be estimated by the square of a matrix element of the two-photon transition matrix,  $T$ , as

$$\Gamma_\nu \propto |\langle \Psi, \chi_\nu | T | \Psi, \chi_0 \rangle|^2, \quad (4.7)$$

where  $\chi_0$  is the initial state, and  $\chi_\nu$  is the  $\nu$  vibrational Rydberg state. Under first-order perturbation theory the transition matrix is independent of the molecular states and is therefore given by the overlap of the molecular wavefunctions, *i.e.*, the Frank-Condon factor [7],

$$\Gamma_\nu \propto \left| \int dR R^2 \chi_\nu(R) \chi_0(R) \right|^2. \quad (4.8)$$

As an example, the relative molecular formation rates are shown in Fig. 4.2 and are in general agreement with the spectroscopic signal strength of each state. Note that also shown are calculated rates of higher excited states that were not resolved experimentally. Furthermore, the position of the estimated amplitudes are set to the calculated values of binding energy which are also in good agreement with observed measurements.

Fig. 4.3 shows spectra extending the range of UV laser detunings over which measurements were made. At sufficiently high detuning, higher oligomer states are evident (in addition to the dimers (D), already featured in Fig. 4.2); trimers (Tr), tetramers (Te), pentamers (P), and hexamers (H). The relative signal strength of different oligomer series is contingent on the density distribution of trapped atoms. In other words, the transition rates depend on

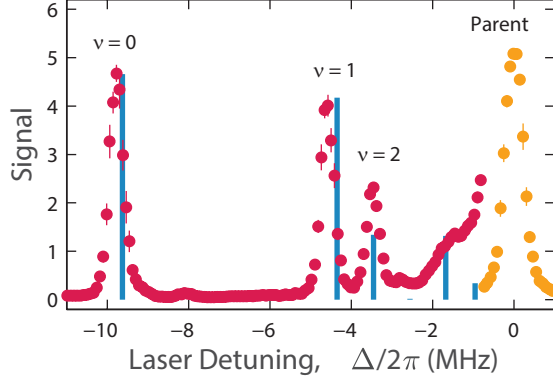


Figure 4.2: Measured Rydberg excitation spectrum (the parent  $38^3S_1$  feature is attenuated by a factor of 10). Calculations done by Shuhei Yoshida of the positions and relative excitation strengths for the  $\nu = 0, 1$ , and  $2$  molecular vibrational dimer states are indicated by the vertical bars.

the availability of a number of neighboring ground-state atoms sufficiently close to the Rydberg excitation commensurate with the oligomer being driven. Therefore, production rate is lower for higher oligomers [7, 31, 47] as the distribution approaches zero at high values of density. Additionally this also is reflected by the difference between the relative amplitudes of the thermal and BEC spectra where the shape of the density distribution itself is quite different (see appendices A and B).

Focusing on the  $n = 38$  spectra, we find that the prevalent features are a repeating pattern correspond to ground-state oligomers and the first couple excited states. This is observed for dimers, trimers, and tetramers. A few other states are resolvable and correspond to multiple excitations of multiple particles. For example, the peaks at -8 MHz and -18 MHz are likely  $Tr_{12}$  and  $Te_{012}$ , given that their binding energy is approximately the sum of the energies of the  $Tr_{01}$  and  $Tr_{02}$  states and the  $Te_{001}$  and  $Te_{002}$  states, respectively.

The binding energies scale as  $1/(n - \delta_l)^6$ , *i.e.*, they change as the inverse of the Rydberg electron wavefunction amplitude. That is to say, with increasing principal quantum number, the molecular potential depth decreases as the Rydberg wavefunction increases in spatial extent, resulting in smaller binding energies, as is evident from the  $n = 49$  data in Fig. 4.3. Our measurements agree well with this scaling of the binding energy (Fig. 4.4). Though higher oligomers are evident (*e.g.* pentamers), a fixed laser linewidth prevents us from

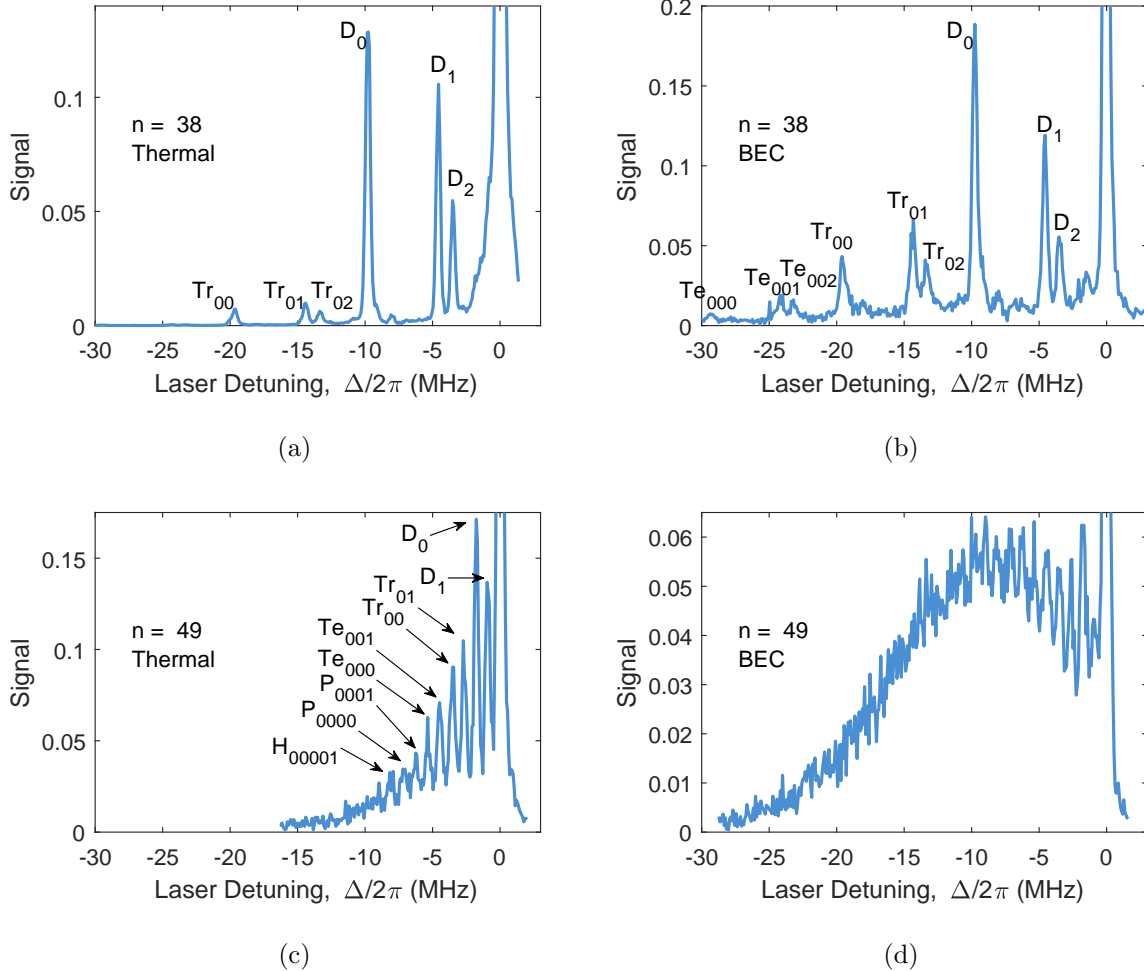


Figure 4.3: Left column: spectra taken in thermal samples, right column: spectra taken in BEC samples. Top row:  $n = 38$  spectra. Bottom row:  $n = 49$  spectra. Pure atomic excitation is at zero detuning, and lines for dimers ( $X = D$ ) through hexamers ( $X = H$ ) are visible. Subscripts ( $X_{ij\dots}$ ) indicate the molecular levels of the Rydberg potential occupied by atoms after laser excitation.

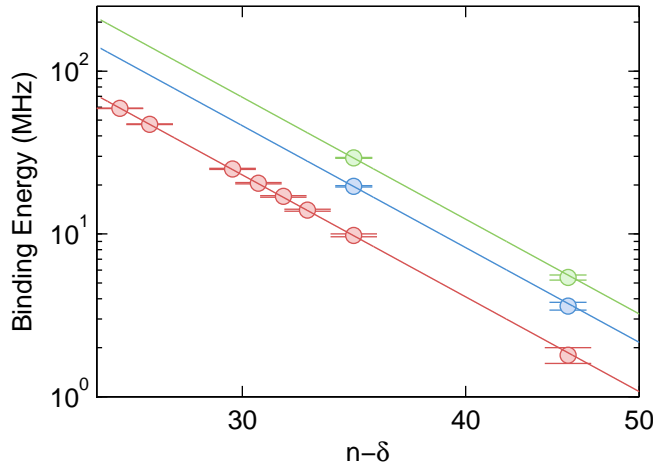


Figure 4.4: Measured binding energies for the ground state wavefunctions of dimers (red), trimers (blue), and tetramers (green) along with  $1/(n - \delta_l)^6$  fit trendlines. Data presented is a combination of results of from [7] and this work.

resolving all of the corresponding excited states observed at  $n = 38$ . Additionally, we find the ground states of each oligomer to be evenly spaced, indicating no significant boson-boson interaction.

Prevalent in the  $n = 49$  data is a background signal on par with the amplitude of the individual molecular lines. This indicates physics beyond a single-particle picture. Increasing  $n$  further to 60 and 72 as shown in Fig. 4.5, away from zero detuning we *only* see a continuum feature corresponding to a many-body response of the system. In Ch. 6, I present a mean-field description of the spectra, which elucidates our observations at high  $n$ . In Ch. 7, I present a quantum description that is valid in both the few- and many-body regime [44, 45].

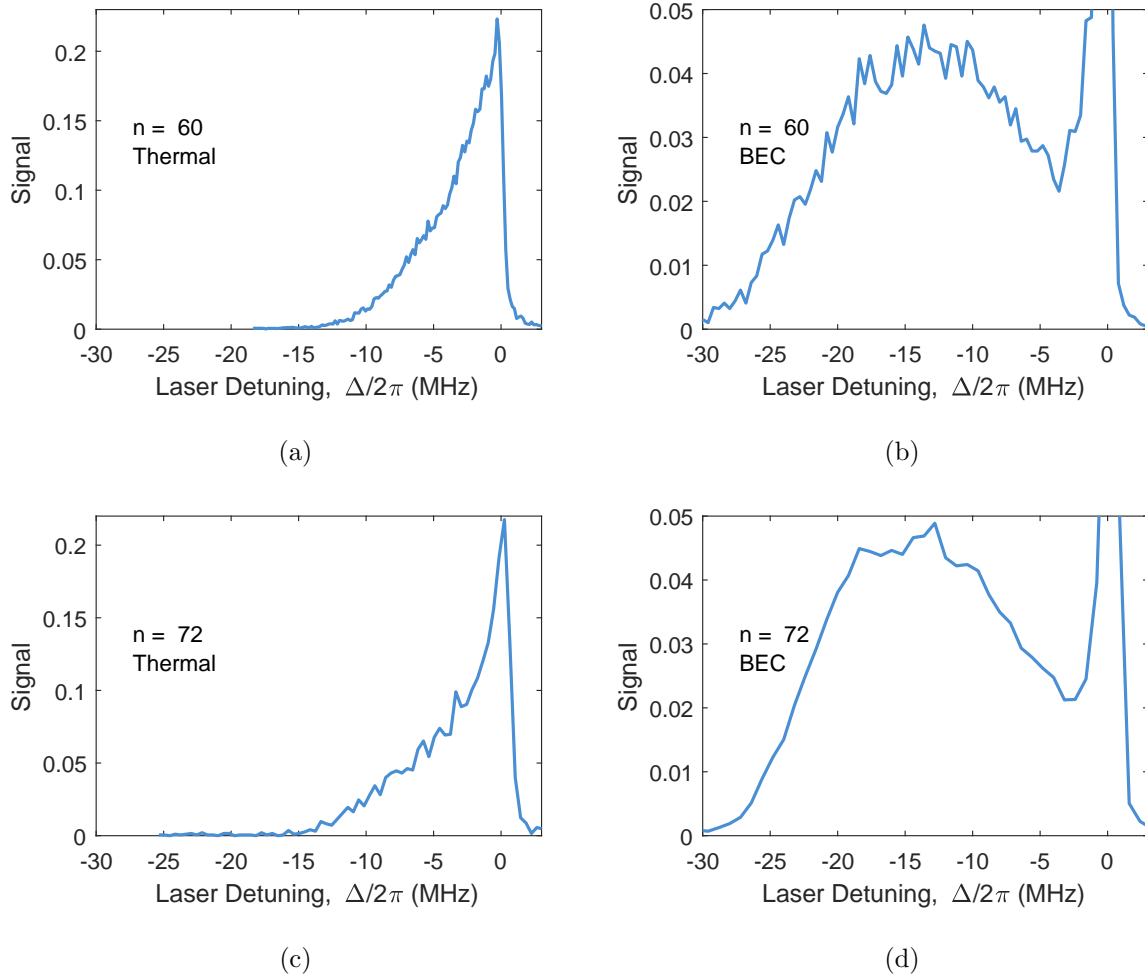


Figure 4.5: Left column: spectra taken in thermal samples, right column: spectra taken in BEC samples. Top row:  $n = 60$  spectra. Bottom row:  $n = 72$  spectra.

# Chapter 5

## Rydberg State Decay

Any Rydberg experiments that require long coherence times are beholden to the decay channels of states of interest, which in turn set feasible experimental time scales. To this end, we have investigated the different decay mechanisms of  $5sns\ ^3S_1$  atomic and molecular states across the few- to many-body regimes. Natural radiative decay is present in all our observations and is found to scale as  $n^{-3}$ , as expected. However it is not the only reaction by which Rydberg states change. In the few-body regime we find decay can occur via collisions with the background given by a cross-section slightly smaller than the geometric size of the Rydberg wavefunction, as well as transitions induced by blackbody radiation. In the many-body regime we encounter decay of Rydberg molecules due to internal dynamics between bound atoms and the ionic core. The rates of these reactions at high densities are found to be much faster than radiative decay and dominate the evolution of a Rydberg state in this regime.

The first experiments on molecular Rydberg lifetimes [33] concentrated on  $(35s)\text{Rb}$  atoms in a thermal state. This work showed these dimer states posses a significantly larger natural decay rate as compared to the parent atomic Rydberg state. This difference was attributed to the inward penetration of the potential by the molecular states due to the strong p-wave shape resonance in electron-Rb scattering. In contrast, there is no p-wave shape resonance in Sr and in the limit of low density we find no appreciable difference between the natural decay rate of the parent and the dimer molecular states. In addition, we find molecular cross-sections to be smaller than the geometric cross-section [35], and decay in the few-body

regime occurs predominantly through natural radiative decay, in addition to collisions with the background, and transitions due to blackbody radiation (BBR).

Lifetime measurements have also been extended to BEC densities and multiple other quantum numbers in Rb [36], where two reactions were identified as additional decay channels, associative-ionization and L-changing collisions. We have carried out similar measurements in Sr [37] in a BEC in the intermediate- and many-body regimes and identify the presence of the same decay channels at similar rates.

## 5.1 Decay Rate in Few-Body Regime

Driving the  $5s38s\,{}^3S_1$  transition in a thermal gas, we have measured decay in the few-body regime where the average number of atoms within a Rydberg orbital is  $\sim 1$ . We identify the lifetimes of the atomic state and three dimer states at a variety of densities. The spectrum of these states is shown in Fig. 4.2.

For this experiment,  $1.3(6)\times 10^6$  atoms were trapped in the ODT at a temperature of  $2.2(1)\,\mu\text{K}$  and average density of  $1.5(2)\times 10^{13}\,\text{cm}^{-3}$ . Excitations were driven as described in Ch. 3. To measure the decay rate of the state, we allow for a variable delay time,  $t_D$ , between driving the transition and the beginning of the ionization pulse, Fig. 5.1. The ODT is turned off during excitation in order to prevent inhomogeneous Stark shifts which would result in broadening of the spectrum. Within one sample, multiple measurements are conducted at a rate of 4 kHz. Between subsequent pulses the density does not change much, but after 150–250 cycles, we hold the sample within the ODT (without Rydberg excitations) long enough for loss of atoms from the trap. Thus, repetition of the excitation sequence would then yield lifetime measurements at lower densities.

Figure 5.2 shows plots of the SFI profiles at different values of delay time for the parent state and the ground molecular state. Nearby states are populated with increasing delay time and are identified by their ionization field which is well described by Eq. 3.2. The broad shoulder at high electric field is present at the earliest times for each dimer SFI profile, but it is absent for atomic excitation (Compare Figs. 5.2 (a) with 5.2 (b)). At early times, collisions and blackbody decay have not yet had any effect. The shoulder at high field is ascribed to

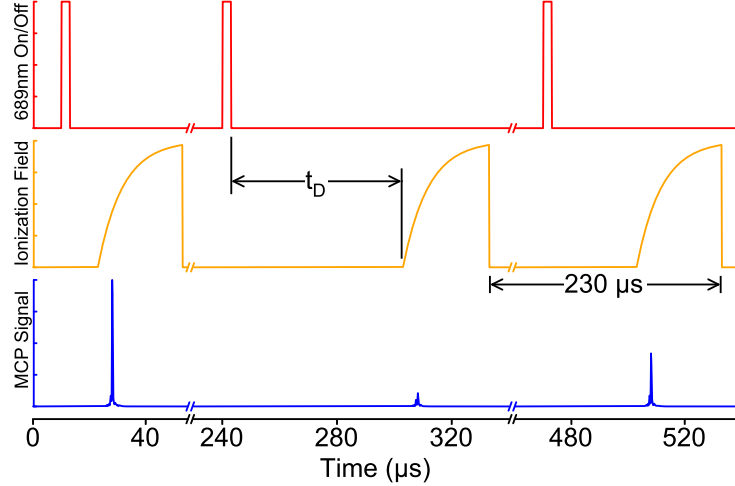


Figure 5.1: Schematic diagram of the timing sequence used to determine lifetimes. The time between laser pulses and the beginning of field-ionization is varied. We maintain the time between ionization ramps fixed at  $230\ \mu s$ , a time long compared to the lifetimes measures such that no residual Rydberg states remain in between pulse sequences.

an intrinsic effect during the selective field ionization of a dimer due to the presence of the bound atom in the Rydberg orbital [37].

Fig. 5.3 shows the integral of the  $38S$  peak signal of the SFI profiles in the few-body regime as a function of delay time, normalized to have an initial population of one. We model this state evolution as

$$\frac{dN_P}{dt} = -(\Gamma_R + \Gamma_S + \Gamma_{BBR})N_P, \quad (5.1)$$

where  $N_P$  is the state population,  $\Gamma_R$  is the natural radiative decay rate,  $\Gamma_S$  is the decay rate due to scattering collisions with the background gas, and  $\Gamma_{BBR}$  is decay due to black-body radiation. We describe the rate of collisions with the background as the product of a cross-section  $\sigma_S$ , the background gas density  $\rho$ , and the average relative collision velocity  $\bar{v}$ .

$$\Gamma_S = \bar{v} \sigma_S \rho \quad (5.2)$$

Fitting to an exponential (of the form Eq. 5.1), yields a single rate constant. Isolating the collisional decay contribution is achieved through repeated measurements at different densities. Given the linear dependence of  $\Gamma_S$  on  $\rho$ , we determine the cross-section of each

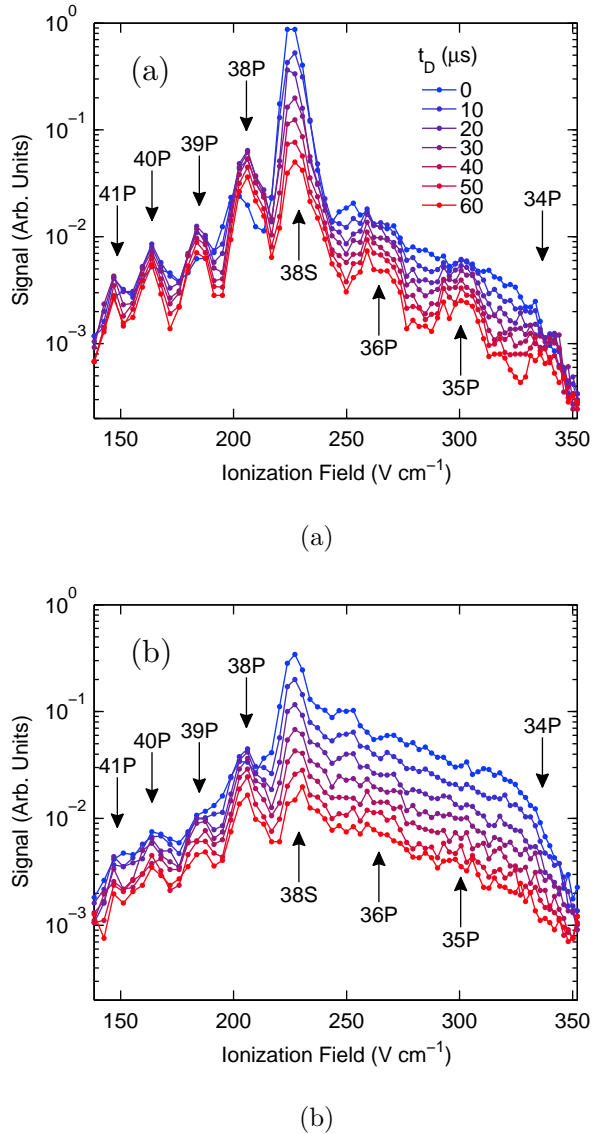


Figure 5.2: Evolution of the SFI spectrum for (a) the parent  $38^3S_1$  Rydberg state and (b) the  $\nu = 0$  molecular vibrational state as a function of delay time. The values of the various delay times used are as indicated. The arrows indicate the  $n$  values of  ${}^3P$  states populated by BBR-induced transitions.

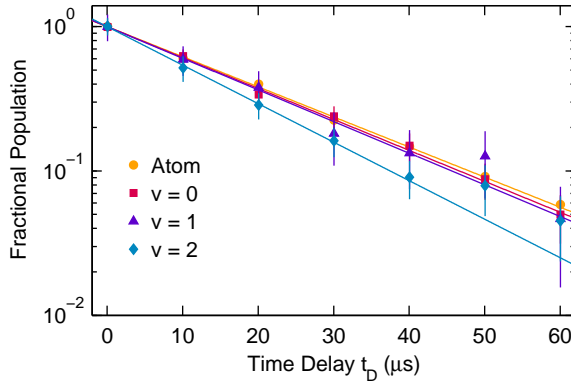


Figure 5.3: Evolution of the population of  $38^3S_1$  Rydberg atoms and of the molecular  $\nu = 0$ , 1, and 2, vibrational states as a function of time delay  $t_D$ . The data sets are each normalized to one at  $t_D = 0$ .

molecule from slope of the linear fits to total decay rate versus density. In Fig. 5.4 the extracted total decay rates are plotted versus density for the various Rydberg states created; the atomic on-resonance transition, as well as the ground state dimer and first two excited dimer states. We find the atomic state to have a collisional cross-section about a factor of  $\sim 1/8$  smaller than the geometric cross-section, given by  $\frac{4\pi}{3}a_0(n - \delta_l)^2$ . The molecular states exhibit a cross-section  $\sim 1/2$  times smaller than geometric cross-section. Fig. 5.4 also shows decay measurements of Rb in a thermal sample at similar temperatures [33]. The density dependence of the molecular Rb rates is suggestive of a cross-section  $\sim 5$  times *larger* than the geometric cross-section. Thus, experiments utilizing molecular Sr in the few-body regime stand to benefit from the relatively small collisional cross-section.

The limit of low density yields the sum  $\Gamma_R + \Gamma_{BBR}$  (the y-intercepts of Fig. 5.4). We disentangle these two rates in the following way. Blackbody radiation causes the parent state to change to Rydberg states of nearby  $n$  and  $L$ . This leads to the increased relative population of states near  $38S$  over time. The parent population undergoes a change of state and the resulting products are detected at different ionization fields (Fig. 5.2). Thus, considering the decay of the SFI signal across all fields over time is less sensitive to  $\Gamma_{BBR}$ . In the limit of low density, examining the evolution of the whole SFI profile yields only the radiative decay rate  $\Gamma_R$ . Depending on the region of integration of SFI profiles we ascertain

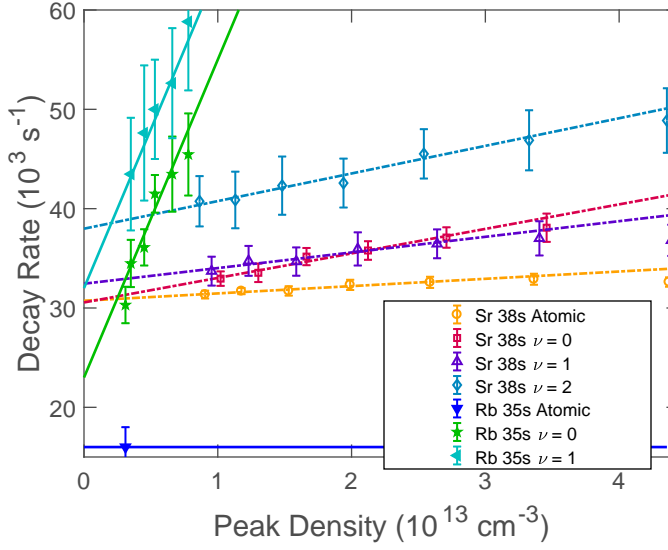


Figure 5.4: Comparison of decay rate results between Sr and Rb [33]. Measured decay rates as a function of peak trap density with linear best fit lines.

State	$\Gamma_R (10^3 \text{ s}^{-1})$	$\Gamma_{\text{BBR}} (10^3 \text{ s}^{-1})$	$\sigma_S (10^{-11} \text{ cm}^2)$
Atomic	31 (2)	17	2 (2)
$\nu = 0$	32 (4)	17	8 (3)
$\nu = 1$	32 (5)	17	6 (3)
$\nu = 2$	39 (4)	22	8 (3)

Table 5.1: Decay rate results and estimated collisional cross-sections for Rydberg atoms and molecules on the  $5s38s^3S_1$  line.

$\Gamma_R + \Gamma_{\text{BBR}}$  or  $\Gamma_R$ , by then taking the difference we estimate  $\Gamma_{\text{BBR}}$ .

The measured values of natural decay and blackbody rates as well as collisional cross-sections are presented in Table 5.1. We find the values of  $\Gamma_{\text{BBR}}$  to be in agreement with results from a two-active-electron model [35], and are consistent with previous studies [65–67]. The determined natural decay rate of the atomic state is found to be  $31(2) \times 10^3 \text{ s}^{-1}$ , about twice as large as  $\Gamma_{\text{BBR}}$ . Similar rates are found for the ground and first excited dimer states. The second vibrational excited state appears to have a faster natural decay at  $39(4) \times 10^3 \text{ s}^{-1}$  which may be attributed to the spatial extend of the wavefunction which penetrates more deeply into the region of the Rydberg core (Fig. 4.1).

## 5.2 Decay Rates in Many-Body Regime

Now we consider decay rate measurements at higher  $n$  where we can access the many-body regime where between  $\sim 10\text{-}150$  atoms can be found within a Rydberg orbital. These experiments were conducted in BEC samples of peak densities of  $\sim 4 \times 10^{14} \text{ cm}^{-3}$ . We observe fast decay rates that are not explained by the mechanisms discussed previously. That is, scaling the measured cross-section which goes as  $n^4$  yields an underestimate by about an order of magnitude compared to the rates observed. Similar to the findings of Ref. [36], we conclude that associative-ionization (AI) and L-changing collisions (LCC) are the reactions by which the fast population decay in the many-body regime takes place.

Associative ionization is a chemi-ionization reaction [11, 22, 23, 68], which results in the binding of the ionic Rydberg core and a neutral ground state atom (Fig. 5.5).

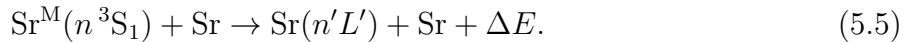


This is due to the attractive interaction at short-distance dictated by the  $\text{Sr}^+ - \text{Sr}$  potential. After a collision with the core, the Rydberg electron becomes unbound and is ejected with excess energy from the reaction. Recall that measurements count the number of electrons that result from field ionization, and because the electron resulting from AI is ejected from the trap before field ionization commences, the creation of  $\text{Sr}_2^+$  appears as signal loss. AI can occur because creation of a Rydberg state with a sufficiently high local density necessarily means there are neutral atoms near the ionic core. Thus, these atoms experience the  $\text{Sr}^+ - \text{Sr}$  potential,

$$V_{\text{Ion}}(r) = -\frac{C_4}{r^4} \quad (5.4)$$

which would otherwise be shielded by the Rydberg electron if the initial atom-core separation was sufficiently large. The  $C_4$  is equal to half the Sr polarizability,  $\alpha = 200 \text{ a.u.}$  [69].

The other reaction that we identify as playing a significant role is LCC. The process is similar to AI in that it is mediated by the atom-core potential, and thus shares similar time-scales. However, the reaction products are different,



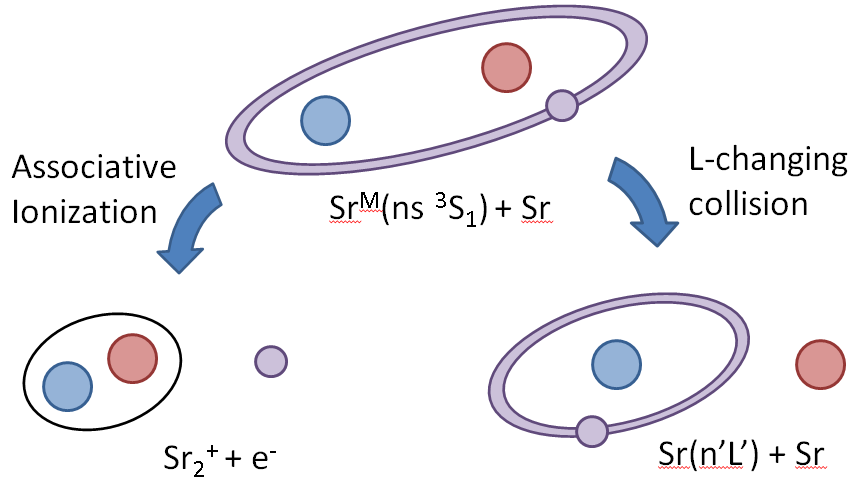


Figure 5.5: Diagram of the two decay channels that arise from the internal dynamics of a Rydberg molecule. The blue circles denote the Rydberg ionic core, the purple circles and rings denote the Rydberg electron, and the red circles represent an initially bound atom. Associative ionization produces a  $\text{Sr}_2^+$  molecule and a free electron. Through an L-changing collision, enough energy is released to dissociate the molecule and a Rydberg atom results with different values of  $nL$ .

The Rydberg electron transitions to a state of different  $n$  and  $L$ , here denoted as  $\text{Sr}(n'L')$ . The product Rydberg state has sufficiently low enough energy such that it will remain within the vicinity of the trap and is detected through field ionization. At the same time, any Sr atoms become unbound from the Rydberg molecular potential after an LCC reaction.

We conduct lifetime measurements across three values of the principal quantum number ( $n = 49, 60, 72$ ) in BEC samples, the spectra of which are shown in Fig. 5.6. From a mean-field description of the spectrum (detailed in Ch. 6), we know that the value of the laser detuning determines the average local density at which excitations take place within the sample. The particular density addressed is proportional to the value of detuning. In this way, instead of varying the total number of atoms trapped in order to adjust density, we are able select at which local density a Rydberg excitation will occur via the choice of laser detuning. On-resonance excitations correspond to regions of low density within the sample, thus the states created at this detuning do not undergo AI or LCC, on the time scale of this measurement since no Sr atoms are sufficiently close enough to react with the Rydberg core.

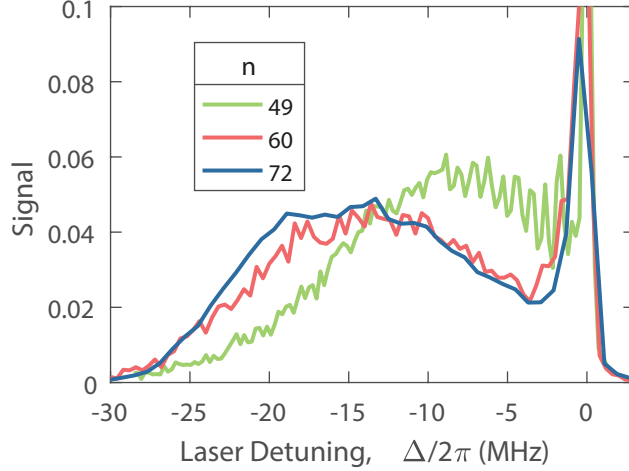


Figure 5.6: Excitation spectra recorded for (a) 49s, (b) 60s, and (c) 72s Rydberg states expressed as a function of detuning from the atomic line. The spectra are normalized to have equal areas.

Figs. 5.7, 5.8, and 5.9 show the time evolution the SFI profiles at  $n = 49, 60, 72$ . Because of the fast decay rates at play, the pulse duration is kept to  $1-2\ \mu\text{s}$  and similarly, the electrode slew-rate is fast enough to ionize within  $1 - 2\ \mu\text{s}$ . Fig. 5.10 shows the integral of the SFI profiles across all electric fields as a function of delay time. Integrating across all fields means that the signal is comprised of any Rydberg states present, including those that result from LCC events.

We model the decay of the Rydberg parent state population,  $N_P$ , as

$$\frac{dN_P}{dt} = -(\Gamma_R + \Gamma_{\text{AI}} + \Gamma_L)N_P, \quad (5.6)$$

where  $\Gamma_R$  is the natural radiative decay rate,  $\Gamma_{\text{AI}}$  is the AI rate, and  $\Gamma_L$  is the LCC rate. Because we integrate the whole SFI profiles, in addition to measuring  $N_P$ , we also detect nearby Rydberg states, the population of which follows

$$\frac{dN_L}{dt} = \Gamma_L N_P - \Gamma_R N_L. \quad (5.7)$$

We assume that the difference in orbital angular momentum is small enough such that these state also radiate at the same rate,  $\Gamma_R \propto n^{-3}$ . The analytic solutions to these rate equations

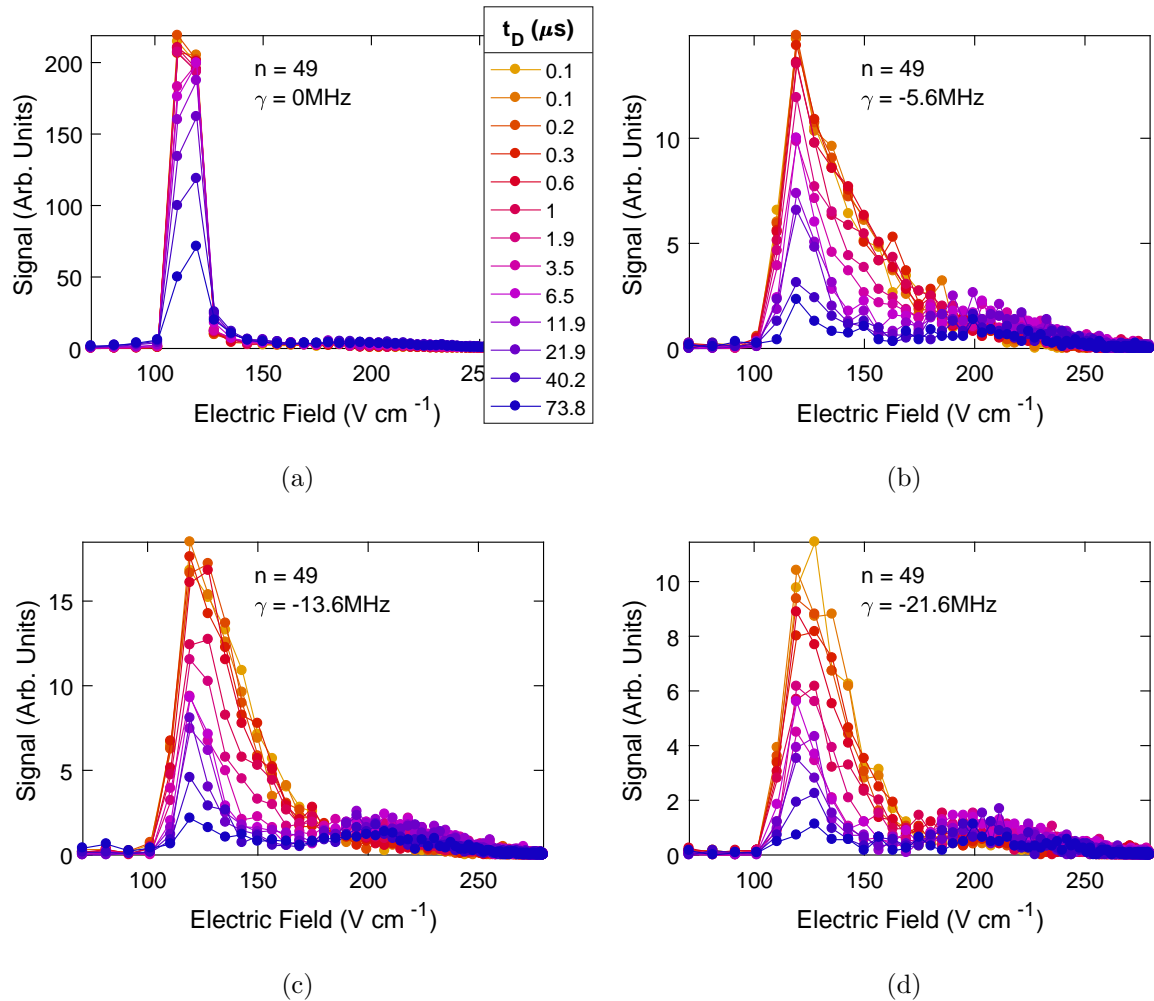


Figure 5.7: Time evolution of the SFI spectra recorded for  $n = 49$  and the detunings indicated.

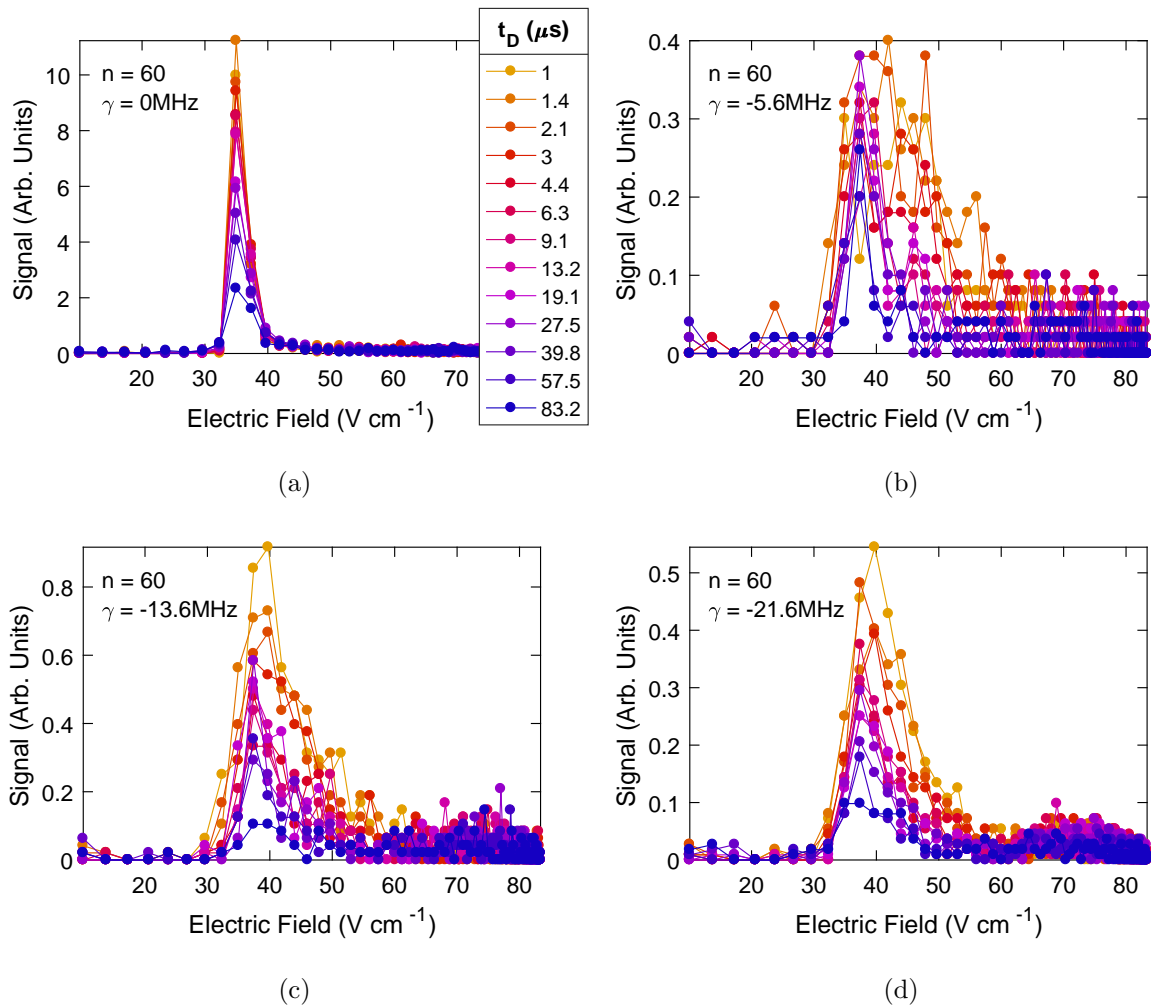


Figure 5.8: Time evolution of the SFI spectra recorded for  $n = 60$  and the detunings indicated.

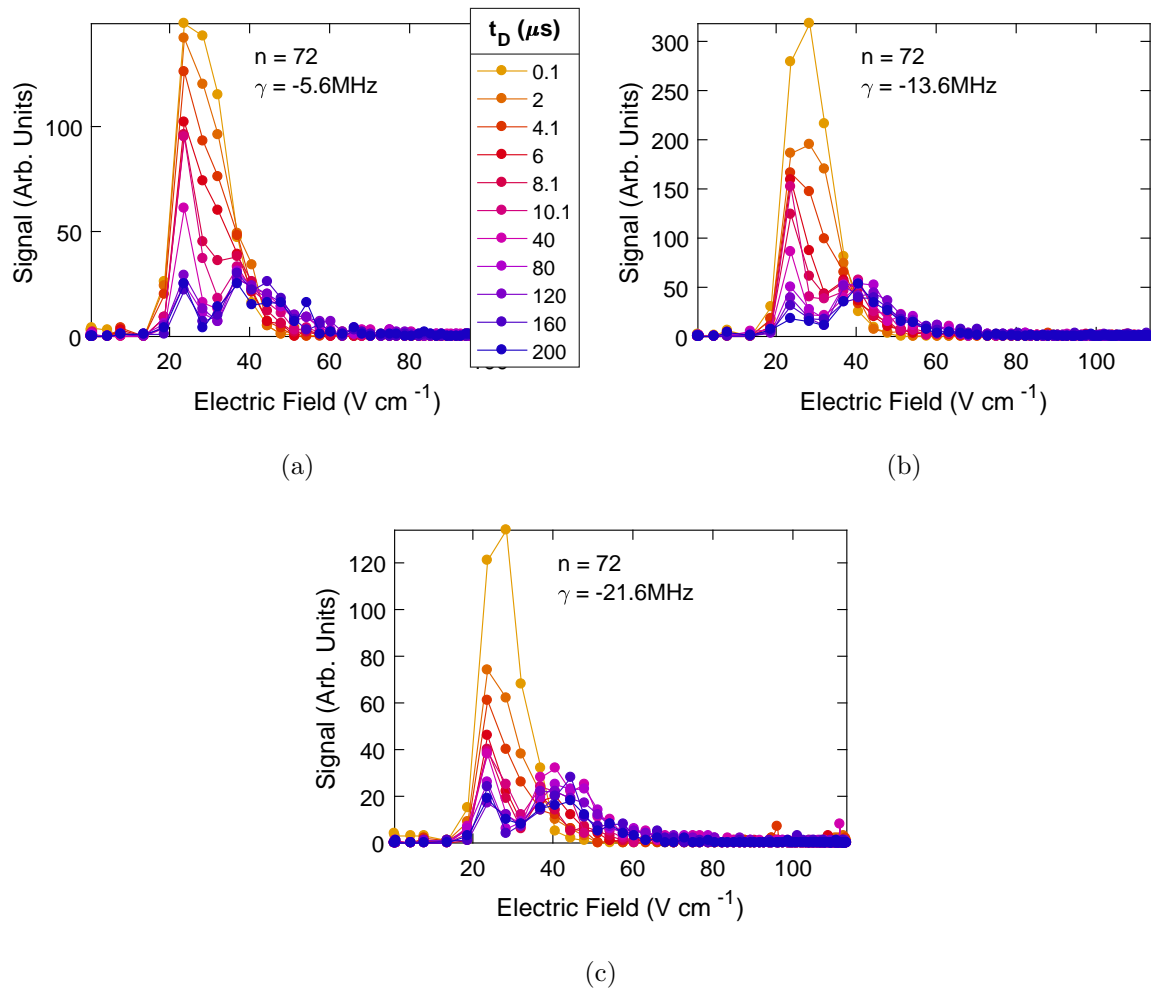


Figure 5.9: Time evolution of the SFI spectra recorded for  $n = 72$  and the detunings indicated.

are in terms of the initial Rydberg parent state population,  $N_0 \equiv N_P(0)$ ,

$$\begin{aligned} N_P &= N_0 e^{-(\Gamma_R + \Gamma_{AI} + \Gamma_L)t} \\ N_L &= N_0 \frac{\Gamma_L}{\Gamma_{AI} + \Gamma_L} e^{-\Gamma_R t} [1 - e^{-(\Gamma_{AI} + \Gamma_L)t}]. \end{aligned} \quad (5.8)$$

Both of these populations are Rydberg states, either the parent  $ns^3S_1$  or other nearby state. As such, by ramping up electric fields, all these states are ionized resulting in electrons, all of which can be detected by the MCP. In other words, we measure the sum  $N_P + N_L$  as a function of delay-time. Fig. 5.10 shows the data along with fits to the sum of Eqs. 5.8, for off-resonant detuning values. In all off-resonant data, two regimes of decay are present. At short-time, the fast depopulation of the parent state by AI and LCC dominate state evolution. At later times, with a depleted molecular state population the AI and LCC decay channels close. Any remaining Rydberg states experience decay dominated by the natural radiative decay, similar to on-resonant states.

Fig. 5.11 shows a  $n^{-3}$  fit of the natural decay rates  $\Gamma_R$  which agrees with results in the few-body regime. Also plotted is the sum  $\Gamma_{AI} + \Gamma_L$  at different values of principal quantum number  $n$  and at various UV laser detunings corresponding to excitations at different local-densities. Additionally, we present calculation results of AI and LCC rates from our collaborator Jesús Pérez-Ríos [37]. Natural decay rates at non-zero detunings do not differ greatly from the parent state indicating that the Rydberg product of LCC events are indeed states of low-L. Meanwhile, the sum  $\Gamma_{AI} + \Gamma_L$  has no dependence on  $n$  which follows from  $V_{\text{Ion}}$  being state independent.

We can qualitatively assess the dependence of the fast decay rates on local density as follows. The rates of AI and LCC can be thought of as the inverse of the time needed for the closest atom to reach the Rydberg core given the attractive atom-core interaction and the average nearest-neighbor distance in the gas. We can calculate this time by neglecting initial kinetic energy and equating the kinetic energy to the decrease in potential energy as an atom falls towards the ion core,

$$-V_{\text{Ion}}(r) = \frac{1}{2}\mu \dot{r}^2 \quad (5.9)$$

where  $\mu$  is the reduced mass,  $r$  is the atom-core separation, and  $-C_4/r^4$  is the potential between a  $\text{Sr}^+$  core ion and a neighboring atom. Then one can integrate to solve for the time

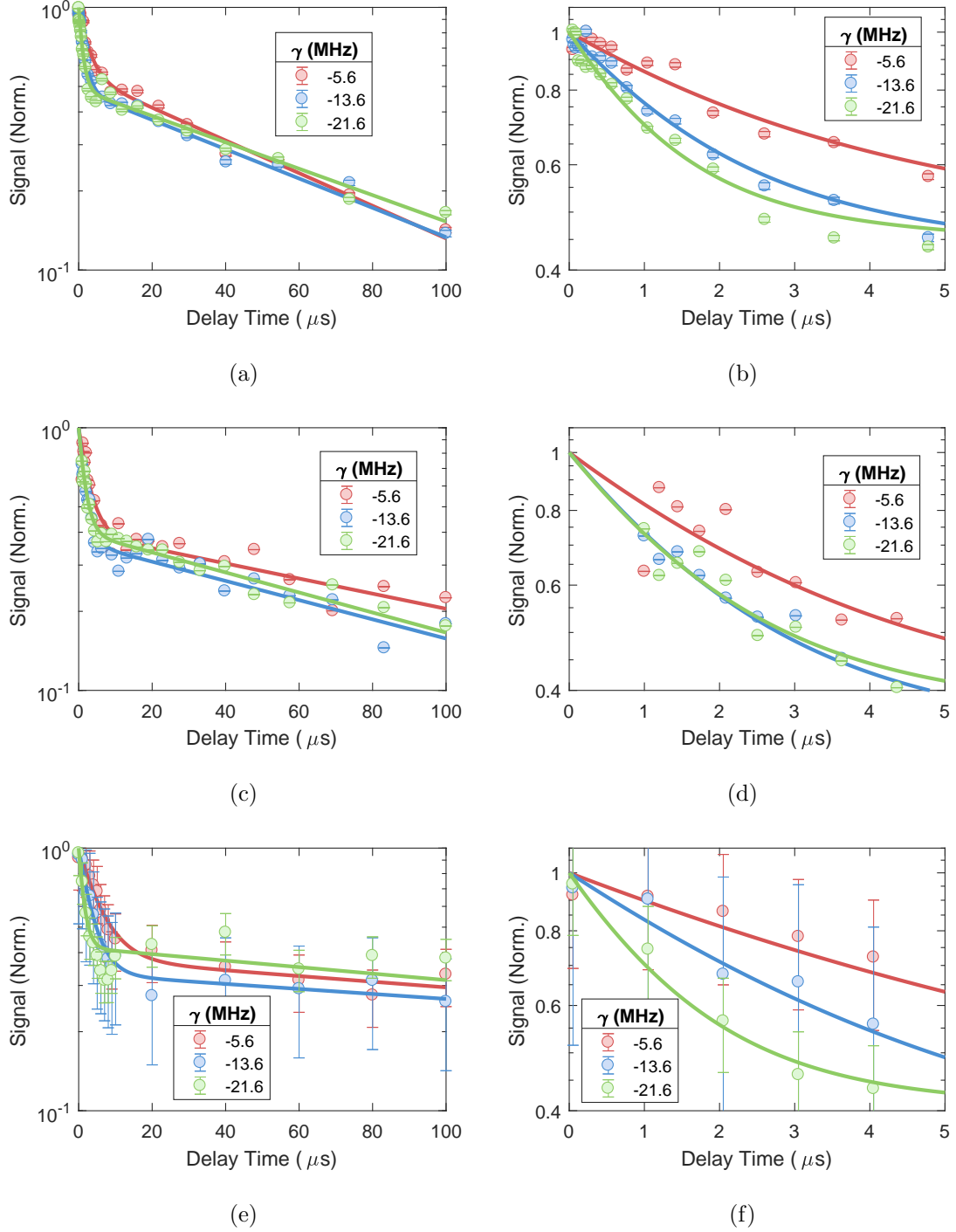


Figure 5.10: Relative Rydberg population evolution over time. In the left-column, decay is plotted over a time range comparable to the natural decay of the Rydberg states. In the right-column a subset of the data is plotted where we focus on the first  $5\ \mu\text{s}$  where AI and LCC are the dominant decay channels. The solid lines show the fits to the data obtained using Eqs. 5.8. Top-row:  $n = 49$ , middle-row:  $n = 60$ , bottom-row:  $n = 72$ .

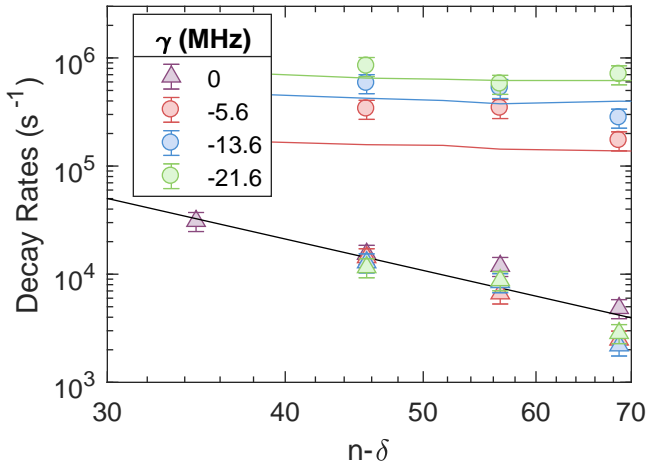


Figure 5.11: Circles: Rydberg molecule destruction rates,  $\Gamma_{AI} + \Gamma_L$ , measured in a BEC for the detunings,  $\gamma$ , indicated. The colored solid lines show the results of model simulations (see text). Triangles: radiative decay rates,  $\Gamma_R$ , measured using thermal samples on atomic resonance and L-changed atoms created in a BEC [35]. The black solid line indicates a fit to the radiative decay rates on resonance.

elapsed during the trajectory of the atom between the initial separation,  $r = R$ , to collision at the core at  $r = 0$ :

$$t \propto \int_R^0 \frac{dr}{\sqrt{C_4/r^4}} \propto R^3 \quad (5.10)$$

Thus the collision time is proportional to the initial interparticle separation to the third power, *i.e.*, the collision rate is proportional to the local density of background atoms. This is indeed what is simulated and observed experimentally, Fig. 5.12.

Fig. 5.13 is a plot from Ref. [36] demonstrating AI and LCC measurements using Rb in a BEC. Within a similar range of  $n$ , we have observed comparably fast decay rates ( $\sim 10^6 \text{ s}^{-1}$ ) in the many-body regime via AI and LCC reactions. Unlike the results in RB, we do not observe a discernible  $n$  dependence. Additionally, at  $n > 110$  increased lifetime was observed. This behavior was attributed to the influence the electron-Rb p-wave shape resonance has on the molecular potential. We have not measured rates at comparable values of  $n$  but it would be interesting to do so. If the explanation for the Rb behavior is correct, we would not expect to see increased lifetime in Sr for  $n > 110$  because there is no analogous shape

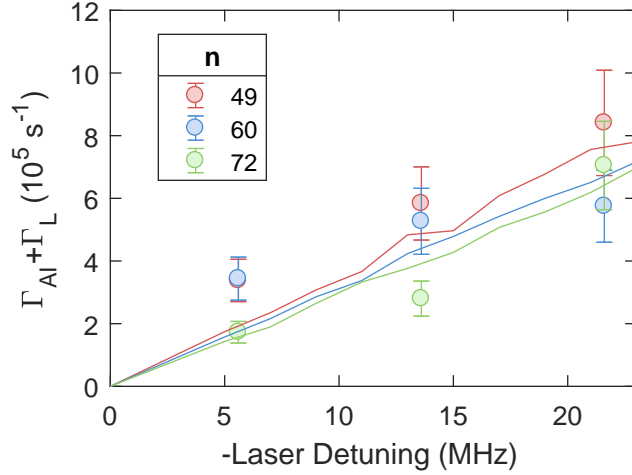


Figure 5.12:  $\Gamma_{AI} + \Gamma_L$  plotted versus UV laser detuning at various values of  $n$ . Plotted are both simulation and experimental results which each demonstrated a linear dependence.

resonance in electron-Sr scattering.

### 5.3 Atom-Rydberg Collisions

We posit that both AI and LCC constitute the microscopic mechanisms by which collisional decay across *all* density. We describe the dynamics as occurring in two steps. First, the time (if any) it takes an atom to reach the region inside the Rydberg orbital where the interaction with the ion core can become strong,  $t_S$ . Second, once an atom is inside the region of the Rydberg electron, there is the time it takes,  $t_{Ion}$ , for the ion to accelerate an atom within the Rydberg orbital to short range where AI or LCC occur. We take these travel times as corresponding to the inverse of their respective decay rates,  $t_S \sim \Gamma_S^{-1}$  and  $t_{Ion} \sim (\Gamma_{AI} + \Gamma_L)^{-1}$ . We assume that the total travel time is indicative of an effective collisional decay rate,

$$\Gamma_{Coll} = \frac{1}{t_S + t_{Ion}}. \quad (5.11)$$

The decay rates observed in either the few- or many-body regime arise from either  $t_S$  or  $t_{Ion}$  acting as a rate-limiting step, respectively. The low-density regime, where initial interparticle separation is large, corresponds to a ballistic limit where  $t_S \gg t_{Ion}$ , such that  $\Gamma_{Coll} \sim \Gamma_S$ . In contrast, when an atom is initially in the vicinity near the core corresponds to setting

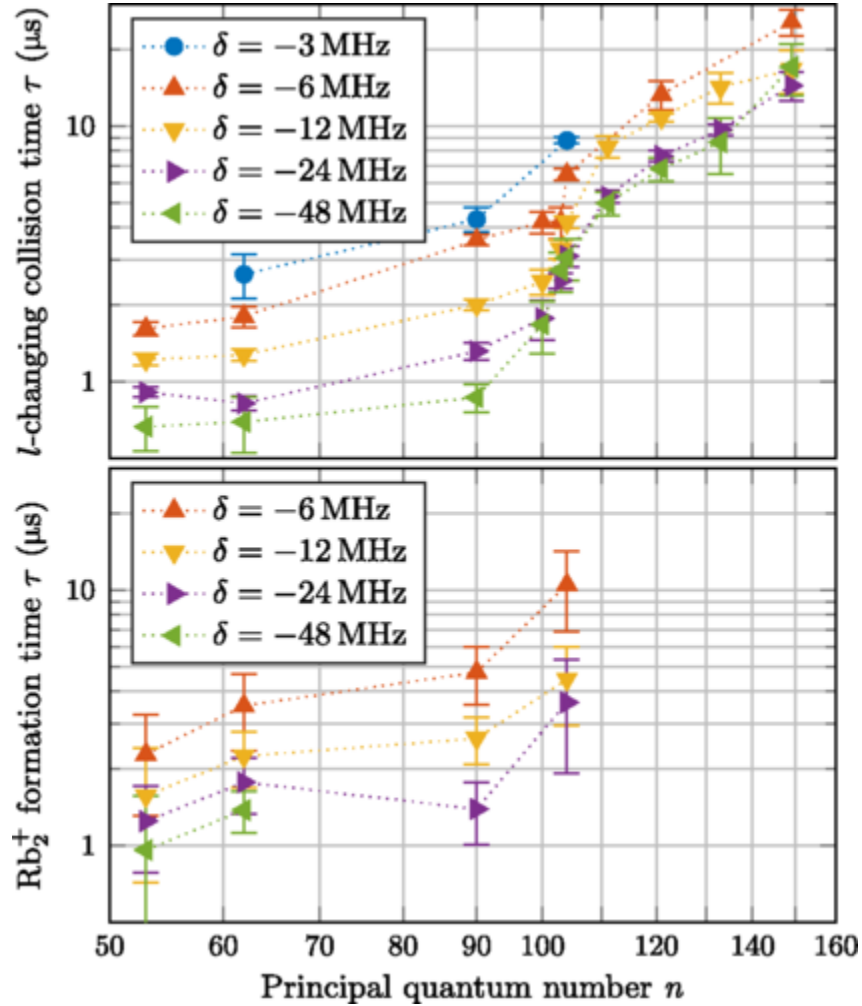


Figure 5.13: L-changing and associative ionization collisions times in a BEC Rb at various detunings as measured and plotted in Ref. [36]. Rates range from  $\sim 2 \times 10^5 \text{ s}^{-1}$  at -3 MHz detuning to  $\sim 10^6 \text{ s}^{-1}$  at -48 MHz for quantum numbers between 50 and 70.

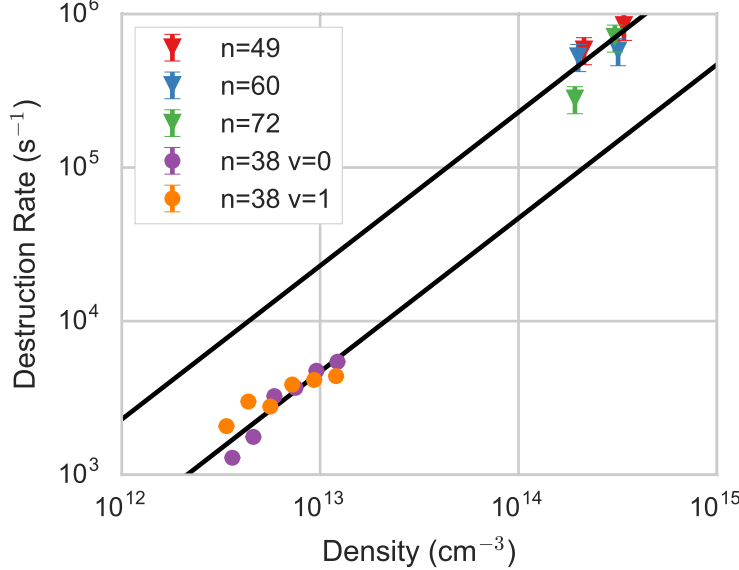


Figure 5.14: Comparison of decay rate measurements made in the few- and many-body regime. We have extrapolated the predictions made by each model. The offset between the two trendlines alludes to the incompatibility of the models across all density. Measurements at  $n = 49, 60, 72$  correspond to the many-body regime, measurements at  $n = 38$  correspond to the few-body regime.

$t_S \rightarrow 0$  such that  $\Gamma \rightarrow \Gamma_{\text{AI}} + \Gamma_L$ .

Fig. 5.14 depicts the observed rates of decay from collisions in both of these limits where the dynamics are ballistic or are mediated by the atom-core potential. Extensions of the model predictions are included, where the apparent mismatch is indicative of incompatibility between the two models. This comparison is possible, because as will be described in Ch. 6, the value of laser detuning used to drive excitations, corresponds to the Rydberg appearing in a specific region of local density within the sample. And so, we are able to translate decay rate measurements in the many-body regime taken at various detunings, into results attributed to regions of different local densities.

The model used to simulate the decay rates in the many-body regime assumed an unscreened ionic core. At fixed temperature and principal quantum number, one could expect this model to break down at sufficiently low density where the average initial particle separation,  $R \propto \rho^{-1/3}$ , far exceeds the spatial extend of the Rydberg electron wavefunction. This

may explain the mismatch in Fig. 5.14. Therefore, we consider a modified *ad hoc* potential to incorporate screening,

$$V'_{\text{Ion}}(r) = V_{\text{Ion}}(r) e^{-r/R_{\text{Orb}}}. \quad (5.12)$$

We define  $R_{\text{Ion}}$  to be a characteristic length scale corresponding to the interparticle separation at which the energy of the modified potential matches the initial kinetic energy,

$$V'_{\text{Ion}}(R_{\text{Ion}}) = k_B T. \quad (5.13)$$

The scattering time-scale goes as  $t_S \sim R^3$ , from Eq. 5.2. Thus, at sufficiently low density  $R \gg R_{\text{Ion}}$ , which is indicative of  $t_S \gg t_{\text{Ion}}$ . Therefore, we would expect  $t_S$  to be the rate-limiting step, yielding  $\Gamma_{\text{Coll}} \sim \Gamma_S$ . For this reason, the few-body regime defined by having  $\sim 1$  atoms within the Rydberg orbital, coincides with the collision rate being determined mostly by the time required for the atom to travel inside the Rydberg orbital where it can feel the strong ion-atom interaction. As mentioned previously, in the many-body regime, the average the initial particle spacing is less than the size of the Rydberg orbital such that we set  $t_S \rightarrow 0$ , resulting in the limit  $\Gamma_{\text{Coll}} \rightarrow \Gamma_{\text{AI}} + \Gamma_L$ . From Eq. 5.13 we expect  $R_{\text{Ion}}$  to decreases with temperature as  $T^{-4}$ . Similarly,  $R_{\text{Ion}}$  increases with  $n$  to an asymptotic value of  $(C_4/k_B T)^4$ , reminiscent of dynamics due to the atom-core potential in the absence of electron screening.

In these studies we have shown the ways in which the presence of ground-state atoms can impact the time evolution of Rydberg states in both the few- and many-body regime. The rates of decay impart constraints on the time scales over which experiments can be conducted in cold, dense gases. Thus, all spectra at high  $n$  presented in this work have been taken as quickly as experimentally feasible in order to minimize the effect of associative-ionization or L-changing collisions. Future lifetime studies using Sr stand to benefit by expanding the range of parameters explored and asses the validity of the models discussed. For example, the studies in Rb, presented rapid decrease in AI and LCC rates at  $n > 110$  which was attributed to a p-wave shape resonance which is absent in Sr. Additionally, a focused examination of the intermediate-regime at  $n = 49$  could be instructive. Thus, at a single value of  $n$ , studies of lifetime on both resolvable molecular states and the continuous far-detuning feature could conducted.



# Chapter 6

## Mean-Field Description in the Many-Body Regime

### 6.1 Mean-Field Spectrum

Scattering between atoms and a Rydberg results in an energy shift of the Rydberg state [70]. In the many-body regime where the number of atoms within a Rydberg wavefunction is large we can employ a mean-field calculation of the spectrum. In particular, from the data presented this applies to spectra at  $n = 60$  and  $n = 72$  where the number of atoms at peak densities are of order 100. The same model is applied at  $n = 49$  which will illustrate deficiencies in the mean-field description as the number of atoms within a Rydberg orbital, which goes as  $n^6$ , becomes small.

For a number of atoms  $dN$  at an energy  $V_{\text{MF}}$ , the shift of a Rydberg line is given by their product,

$$\hbar d\Delta_{\text{MF}} = dN V_{\text{MF}}. \quad (6.1)$$

where we use the contact-interaction potential averaged over the electron wavefunction (Eq. 4.6) to construct the mean-field potential,  $V_{\text{MF}}$ . The total shift can be calculated in terms of the atom sample density. We parameterize the shift and the potential by  $\mathbf{R}$ , the position of a ground-state atom,

$$\hbar\Delta_{\text{MF}} = 4\pi \int dR R^2 \rho(\mathbf{R}) V_{\text{MF}}(\mathbf{R}). \quad (6.2)$$

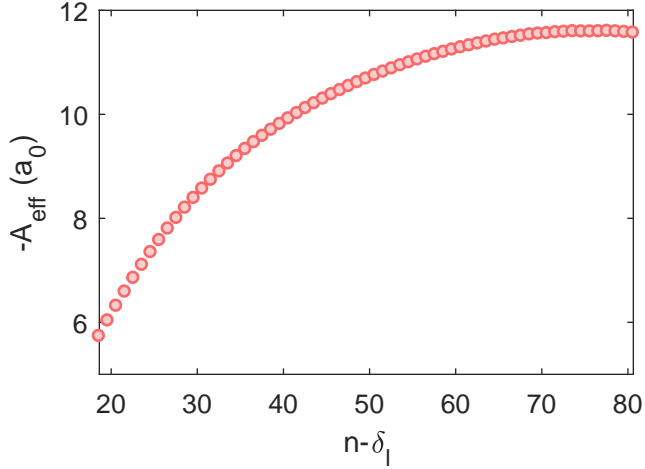


Figure 6.1: Plot of  $-A_{\text{Eff}}$  versus  $n - \delta_l$ .

When the size of the Rydberg wavefunction is much smaller than the size of the atom sample we can employ a local density approximation. That is, when the scale over which the curvature of the cloud density changes is much bigger than the size of the wavefunction, we assume that the density within the wavefunction is constant:

$$\left| \frac{d\rho(r)}{dr} \right| \ll \frac{\rho(r)}{R_{\text{Orb}}}, \quad (6.3)$$

where  $R_{\text{Orb}}$  represents the size of the Rydberg wavefunction. The validity of this approximation for a fixed sample geometry decreases with increasing  $n$ . Under this approximation we can extract the density out of the integral in Eq. 6.2 resulting in

$$\hbar\Delta_{\text{MF}}(\rho) = \frac{2\pi\hbar^2 A_{\text{Eff}}}{m_e} \rho, \quad (6.4)$$

where we have defined the effective scattering length  $A_{\text{Eff}}$ :

$$A_{\text{Eff}} \equiv \frac{2m_e}{\hbar^2} \int dR R^2 V_{\text{MF}}(\mathbf{R}). \quad (6.5)$$

Fig. 6.1 presents the results of a calculation of  $A_{\text{Eff}}$  [45]. The  $n$  dependence of  $A_{\text{Eff}}$  is weak, such that the mean-field shift is dominated by the value of local density and less so by the choice of principal quantum number.

Eq. 6.4 dictates that the total shift is proportional to the local density,  $\rho$ , within a Rydberg wavefunction. If the global density distribution was uniform, the spectrum would resemble

a transition line shifted by an amount proportional to the density. However, experimentally the atom clouds we produce are either in thermal or BEC states trapped in harmonic ODTs, both of which result in a distribution of density.

The thermal cloud spatial density is given by a Boltzmann distribution in terms of the peak density,  $\rho_0$ , temperature,  $T$  and the trapping potential,  $V(\mathbf{r})$ , as a function of the spacial coordinates,  $\mathbf{r}$ , and where  $k_B$  is the Boltzmann constant,

$$\rho_{\text{Th}}(\mathbf{r}) = \rho_0 e^{-V(\mathbf{r})/k_B T}. \quad (6.6)$$

The condensate density is well-approximated with a Thomas-Fermi distribution for a harmonic trap [71]

$$\rho_{\text{BEC}}(\mathbf{r}) = \rho - V(\mathbf{r})/U_0, \quad (6.7)$$

where  $U_0$  is the effective interaction.

From these expressions, we calculate the density distribution function,  $g(\rho)$ , of each, defined by

$$N = \int d\rho g(\rho) \quad (6.8)$$

where  $N$  is the number of atoms in the sample. For thermal ( $g_{\text{Th}}$ ) and BEC ( $g_{\text{BEC}}$ ) samples, the distributions are given by

$$g_{\text{Th}}(\rho) \propto \sqrt{\log \frac{\rho_0}{\rho}} \quad (6.9)$$

$$g_{\text{BEC}}(\rho) \propto \frac{\rho}{\rho_0} \left(1 - \frac{\rho}{\rho_0}\right)^{1/2}. \quad (6.10)$$

These distributions are plotted in Fig. 6.2 normalized such that their shapes are universal irrespective of the absolute value of peak density,  $\rho_0$  (and assuming a proportionality constant of one). See Appendices A and B for details.

Notably, these expressions only depend on the ratio of density to peak density,  $\rho/\rho_0$ . This implies that spectra, when plotted as a function of this ratio, have a universal shape. We find this to be accurate in the many-body regime, Fig. 6.3, where multiple spectra were taken for each  $n$  and normalized according to their peak density,  $\rho_0$ . Specifically, we normalize the frequency axis to the value of mean-field shift at peak density,  $\Delta_0 \equiv \Delta_{\text{MF}}(\rho_0)$ .<sup>1</sup>

---

<sup>1</sup>Note that this is a different comparison than that of Fig. 3.9, in which for the same sample the power was varied and the amplitude of spectra was allowed to vary in order to look for shape-invariance. Instead,

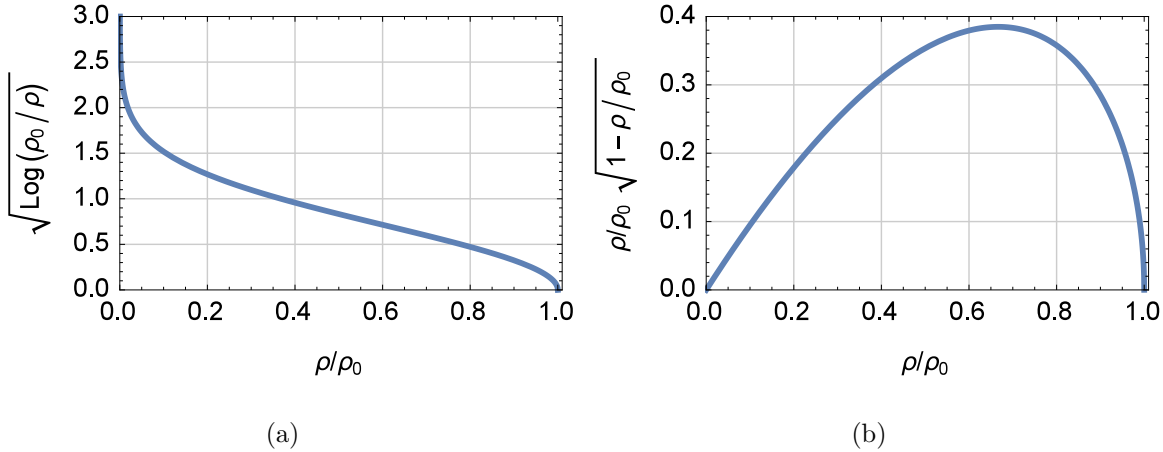


Figure 6.2: Plot of the shape of (a) thermal and (b) BEC density distributions as a function of the ratio of density to peak density.

Given that the mean-field shift is proportional to the density, likewise the spectrum,  $A$ , is proportional to the distribution of density. We can express this in terms of integrals over detuning and density, each of which are normalized such that they equal unity,

$$1 = \int d\Delta_{\text{MF}} A(\Delta_{\text{MF}}) = \int d\rho g(\rho)/N. \quad (6.11)$$

Note that we define  $A$  to be the spectrum normalized per atom in the sample. To arrive at an expression for the density distribution, we do the following: multiply both integrals by a Dirac delta function,  $\delta(\Delta_{\text{MF}} - \Delta)$ , and integrate both over values of laser detuning  $\Delta$ ,

$$\int d\Delta \int d\Delta_{MF} A(\Delta_{MF}) \delta(\Delta_{MF} - \Delta) = \int d\Delta \int d\rho \frac{g(\rho)}{N} \delta(\Delta_{MF}(\rho) - \Delta). \quad (6.12)$$

Substitute density in terms of the mean-field shift using Eq. 6.4, which results in

$$\int d\Delta \ A(\Delta) = \frac{m_e}{2\pi\hbar N A_{\text{Eff}}} \int d\Delta \ g\left(\frac{m_e}{2\pi\hbar A_{\text{Eff}}}\Delta\right), \quad (6.13)$$

implying an expression for the spectrum;

$$A(\Delta) = \frac{m_e}{2\pi\hbar N A_{\text{Eff}}} g\left(\frac{m_e}{2\pi\hbar A_{\text{Eff}}}\Delta\right). \quad (6.14)$$

Thus, under a local-density approximation, the spectrum is a proportional mapping of the density distribution of the atomic sample.

Fig. 6.3 compares spectra corresponding to atom samples with peak density difference up to about 15% and demonstrates that in spite of the difference in absolute density, there is shape universal.

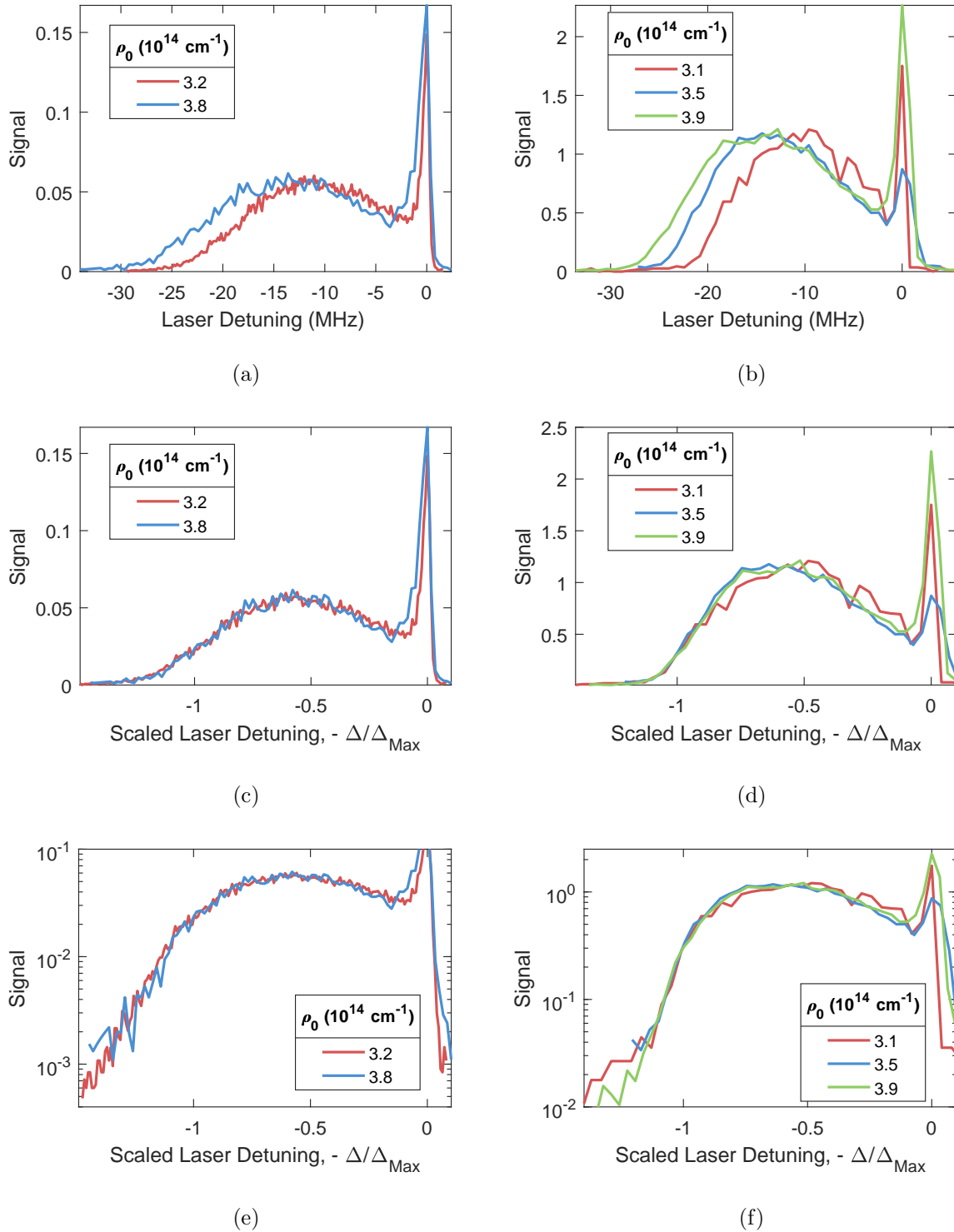


Figure 6.3: Comparison of spectra at different values of peak density. Left column:  $n = 60$  data, right column:  $n = 72$  data. Top row: data plotted versus laser frequency. Second row: data scaled to value of detuning at peak density calculated separately for each trace. Bottom row: same results in log scale demonstrating agreement of signal at high detuning.

$n$	$N_{\text{BEC}} (10^5)$	$\bar{\omega}/2\pi (\text{Hz})$	$\rho_0 (10^{14} \text{ cm}^{-3})$	$\mu/k_B (\text{nK})$
49	2.8 (3)	107 (10)	3.2 (3)	150 (20)
60	3.7 (4)	112 (10)	3.8 (4)	180 (20)
72	3.6 (4)	117 (10)	3.9 (4)	190 (20)

Table 6.1: Experimentally determined parameters. Number of atoms in the condensate ( $N_{\text{BEC}}$ ) and mean trap frequency  $\bar{\omega}$  are determined from time-of-flight-absorption images and Castin-Dum measurements (see Appendix B.3) respectively, and they determine the peak condensate density ( $\rho_0$ ) and chemical potential ( $\mu$ ).

$n$	$\eta$	$\Delta_0 (2\pi \text{ s}^{-1})$	$\Delta_0/\Delta'_0$	$\xi$
49	0.72 (6)	-19 (2)	0.95 (10)	1.8
60	0.77 (3)	-24 (1)	0.93 (5)	1.8
72	0.80 (3)	-24 (1)	0.88 (5)	1.8

Table 6.2: Fit parameters from data shown in Fig. 6.4. BEC fraction ( $\eta$ ) and shift at peak density ( $\Delta_0$ ) are determined from the spectra.

## 6.2 Analysis

I will describe the procedure in terms of the BEC spectra, but the analysis is comparable for the thermal spectra. First, we estimate the fraction of the total number of atoms in the sample that are in the BEC phase, labeled  $\eta$ . The rest, which are thermal atoms, contribute to the spectrum as signal at low-detuning given their relatively low density. Any thermal signal is isolated for analysis (shown as the green confidence band in Fig. 6.4). The BEC fraction is therefore determined from the ratio of the area under the spectrum attributed to condensate atoms to the total area of the spectrum. Alternatively,  $\eta$  can be determined from fitting to time-of-flight atom images [72], these two methods are in good agreement with one another. The experimentally determined peak density and associated parameters are listed in Table 6.2. The extracted values of  $\eta$ , along with other fitting parameter results are shown in Table 6.2.

Knowing what portion of the spectrum is attributed to BEC atoms we can next determine the value of mean-field shift at peak density,  $\Delta_0$ . We adjust the area of the mean-field BEC

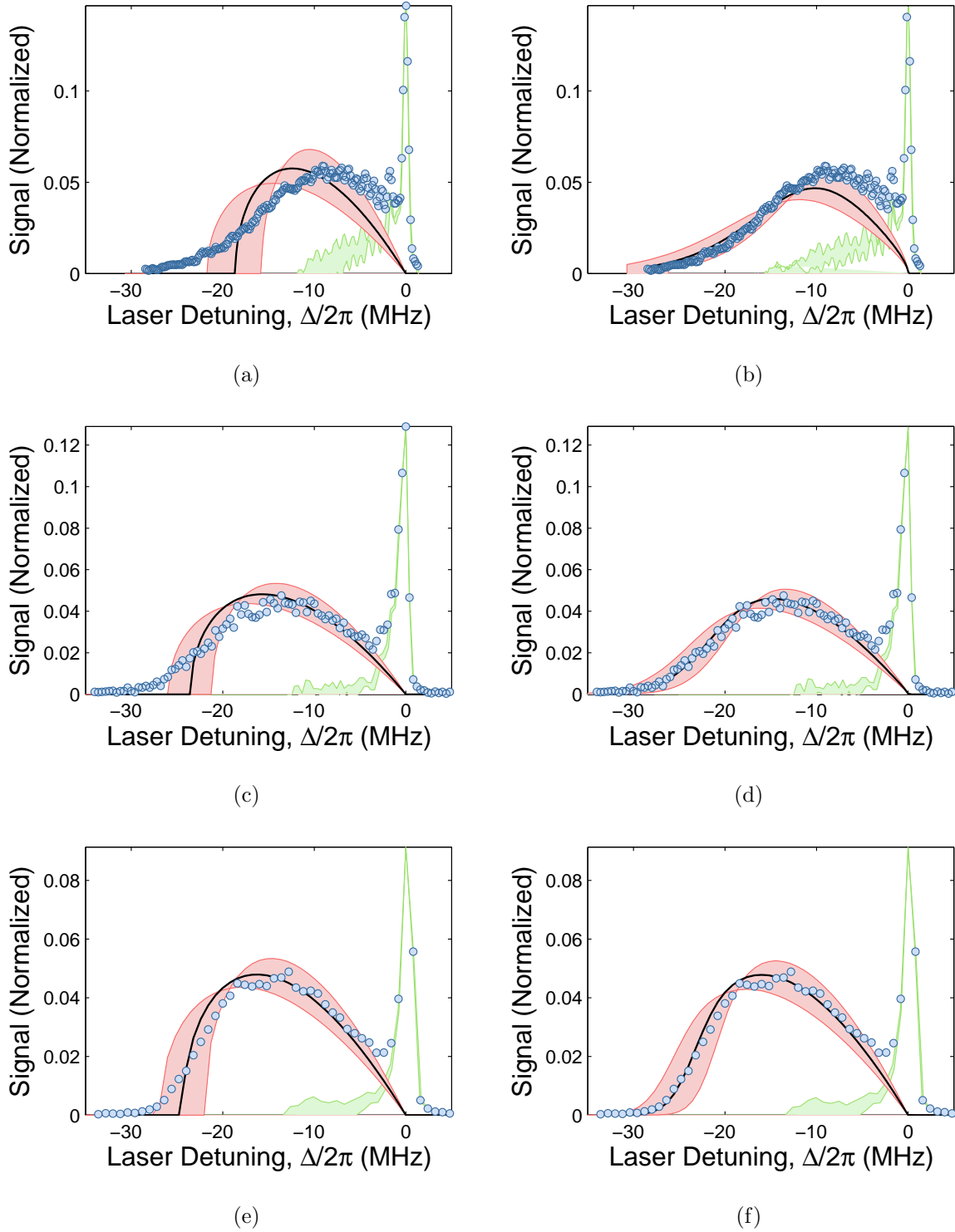


Figure 6.4: Mean-field fits to BEC spectra with (left) and without (right) convolution with the number of atoms within a Rydberg orbital. Top- middle- and bottom-rows correspond to  $n = 49, 60, 72$ , respectively. Blue dots: experimental data, black line: mean-field best-fit result, red band: confidence interval of fit, green band: thermal atoms confidence interval.

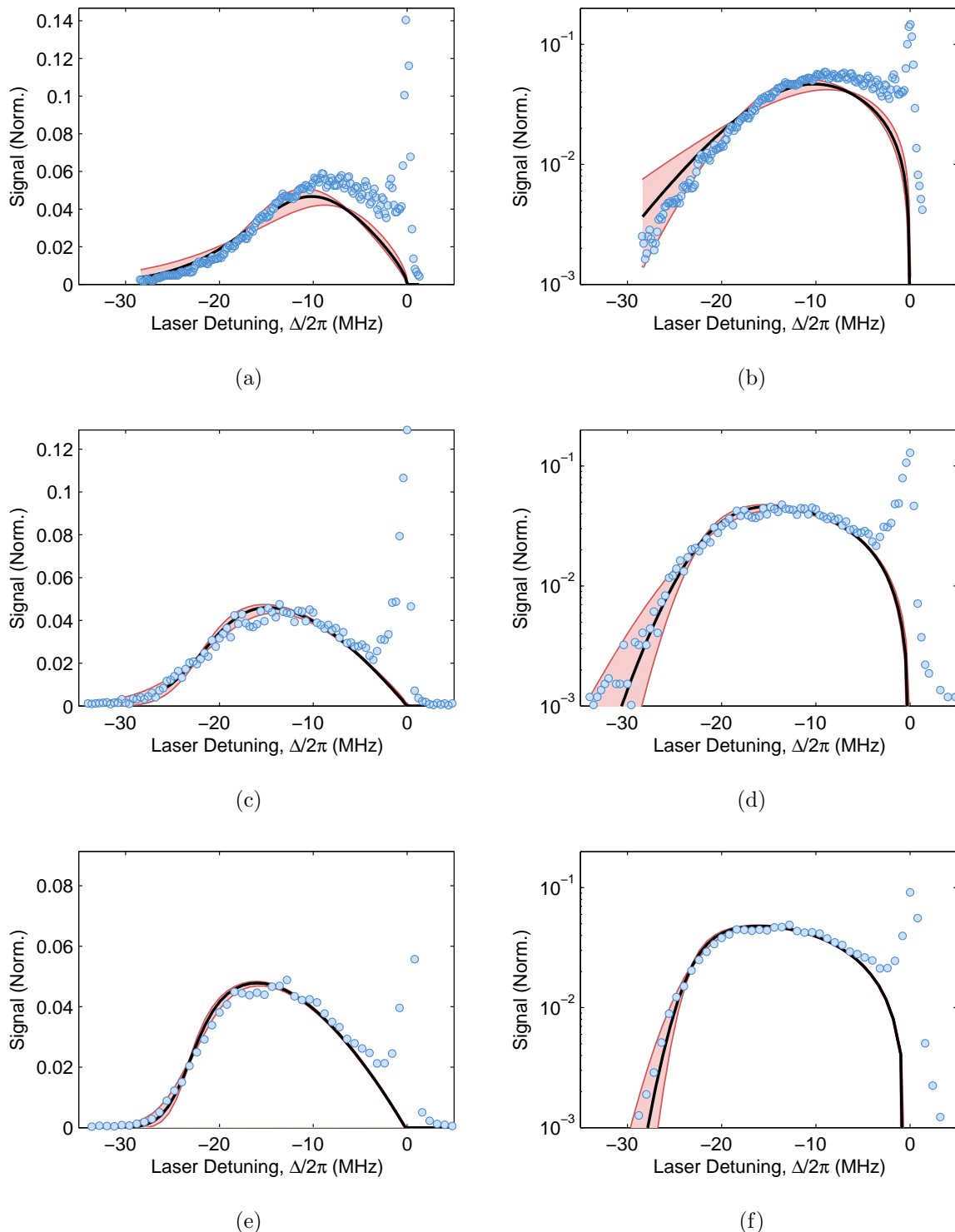


Figure 6.5: Now the data is plotted with an uncertainty band corresponding to  $\xi = 1.8(4)$ .

Top-row:  $n = 49$ , middle-row:  $n = 60$ , bottom-row:  $n = 72$ . Left-column: linear scale, right-column: log scale.

contribution so the sum of the non-condensed and mean-field BEC estimate matches the total experimental spectral area. Because the deviations between the mean-field fit and the BEC spectrum can be significant, the fit of the peak shift  $\Delta_0$  is not rigorous, and is set to satisfy the condition that the mean-field fit and the data have approximately equal area for ( $\Delta/\Delta_0 > 0.5$ ). Uncertainty in the fitting procedure decreases with increasing principal quantum number as the experimental data converges towards the mean-field shape (Fig. 6.4 (a, c, e)). The values of  $\Delta_0$  are all about 10% below  $\Delta'_0$ , where  $\Delta'_0$  is the *a priori* value of mean-field shift at peak-density.  $\Delta'_0$  is calculated from the product of peak BEC density and  $A_{\text{Eff}}$  [45]. This may point to systematic error in our analysis procedure, though a 10% is on par with uncertainty in determination of  $\omega_i$  and total atom number. The calculation of  $A_{s,\text{eff}}$  from  $V_{Ryd}(\mathbf{r})$  (Eq. 6.5) could also account for some of the discrepancy through approximations made to describe the Rydberg-atom potential at short range.

For a gas trapped in an inhomogeneous potential  $U(\mathbf{r})$ , the Hartree-Fock approximation [71, 73] yields a mean-field interaction between thermal and BEC atoms that creates an effective potential for thermal atoms,  $U_{\text{eff}}(\mathbf{r}) = U(\mathbf{r}) + 2g[\rho_{BEC}(\mathbf{r}) + \rho_{\text{th}}(\mathbf{r})]$  that is of a “Mexican hat” shape rather than parabolic [73, 74]. The peak shift in the Rydberg excitation spectrum should in principle reflect the peak condensate density plus the density of thermal atoms at the center of the trapping potential. The contribution from thermal atoms would be a significant correction if the mean-field repulsion of thermal atoms from the center of the trap were ignored. But because the sample temperature is close to the chemical potential, the density of thermal atoms is suppressed at trap center and we neglect it in discussions of the peak mean-field shift in the spectrum.

The mean-field approximation assumes that there are no fluctuations of the density around its local average, and the atomic samples are well described by Eqs. 6.6 and 6.7. But actual density around an atom and the resulting shift of the Rydberg excitation does have fluctuations, and each Rydberg excitation is a quantum mechanical measurement of this quantity. This is properly treated by Ref. [44]. It can also be treated in a classical Monte Carlo [75]. These density fluctuations account for the long tails at far red-detuning which are unaccounted for in the bare mean-field description (Figs. 6.4 a, c, e).

Here we present an alternative treatment that is easily added on top of our mean-field

description. Consider the density pair-correlation function, which expresses the joint probability of detecting two atoms separated by a distance  $R$  [76]. In the case of a BEC, the pair-correlation function is equal to one at any interparticle spacing, indicating classical density fluctuations [77]. In other words, in the simplest treatment of a BEC, the positions of particles are uncorrelated, and thus the probability of finding an atom in a particular region of space is independent of the presence of any other particles in the BEC. Based on this idea, let's calculate the spectrum of density fluctuations inside a small region with uniform average density inside a BEC.

Let's model this sample as a system of fixed total atom number,  $N$ , and total volume  $\mathcal{V}$ . This defines an average density as  $\rho = N/\mathcal{V}$ . Now consider a subvolume  $\mathcal{V}_{\text{Orb}}$ . We want to find the probability distribution function describing the distribution of number of atoms within the subvolume,  $\mathcal{V}_{\text{Orb}}$ . For each atom in  $\mathcal{V}$ , the probability of being in  $\mathcal{V}_{\text{Orb}}$  is  $p = \mathcal{V}_{\text{Orb}}/\mathcal{V}$ . And the probabilities for different atoms are uncorrelated as described above because this is a BEC. Accordingly, the probability of finding the atom anywhere else in the sample is  $1 - p$ . Thus the probability of finding  $k$  atoms within the volume  $\mathcal{V}_{\text{Orb}}$  is encoded by a binomial distribution,

$$P = \binom{N}{k} p^k (1-p)^{N-k} \quad (6.15)$$

In the limit of  $N \rightarrow \infty$ , with the average number of atoms in  $\mathcal{V}_{\text{Orb}}$  held constant ( $Np = \rho\mathcal{V}_{\text{Orb}} \equiv N_{\text{Orb}}$ ), such that the probability of finding an atom within a volume element is small, the binomial distribution is well approximated by a Poissonian distribution<sup>2</sup>

$$P(k, N_{\text{Orb}}) = \frac{N_{\text{Orb}}^k e^{-N_{\text{Orb}}}}{k!}. \quad (6.16)$$

Therefore, atom number fluctuations go as  $\sqrt{N_{\text{Orb}}}$ , set by the standard deviation of the probability distribution. We assume that the relevant volume element over which we calculate  $N_{\text{Orb}}$  is given by the geometry of a Rydberg orbital

$$\mathcal{V}_{\text{Orb}} = \frac{4\pi}{3} [\xi a_0(n - \delta_l)^2]^3, \quad (6.17)$$

where we have introduced the unitless fitting parameter  $\xi$ .

---

<sup>2</sup>Computationally, it is convenient to instead use  $P(k, N_{\text{Orb}}) = e^{k \ln(N_{\text{Orb}}) - N_{\text{Orb}} - \ln(\Gamma(k+1))}$ , which is the Poissonian function for continuous values of occurrences  $k$  [78], where  $\Gamma$  is the gamma function.

To incorporate these fluctuations into the mean-field model, we calculate the spectrum as a convolution of the mean-field result and the atom number Poisson distribution,

$$A'(\Delta) = \int dN' A(N') P(N', N_{\text{Orb}}(\rho(\Delta))). \quad (6.18)$$

Good agreement with the data is found with  $\xi = 1.8$ , which is in qualitative agreement with our assumption that the size of the Rydberg orbitals is the appropriate volume over which to calculate fluctuations (Figs. 6.4 b, d, f). A region with average density  $\rho = N_{\text{Orb}}/\mathcal{V}_{\text{Orb}}$  will contribute to the spectrum on average at  $\Delta_{\text{MF}} = \frac{2\pi\hbar A_{\text{EFF}}}{m_e} N_{\text{Orb}}/\mathcal{V}_{\text{Orb}}$ . This value will fluctuate due to number fluctuations within  $\mathcal{V}_{\text{Orb}}$  given a width  $\delta\Delta = \frac{2\pi\hbar A_{\text{EFF}}}{m_e} \sqrt{N_{\text{Orb}}}/\mathcal{V}_{\text{Orb}} = \Delta/\sqrt{N_{\text{Orb}}}$ . Thus the relative width is  $\delta\Delta/\Delta = 1/\sqrt{N_{\text{Orb}}} \propto n^{-3}$ , which yields better agreement with the bare mean-field description at increasing  $n$ .

In contrast to a BEC, in thermal samples of bosons of sufficiently low temperatures, spatial correlations are present [76]. The pair correlation function for bosons is given by

$$g^{(2)}(R) = 1 + e^{-R^2/\lambda_{dB}^2} \quad (6.19)$$

where  $R$  is the interparticle spacing and the de Broglie wavelength,  $\lambda_{dB}^2$ , sets the lengths scale below which correlations become relevant. The regions of a trap with highest density will be the most susceptible to these correlation effects. That is, the far red-detuned tail of spectra, which corresponds to positive density fluctuations could exhibit non-classical bunching of particles. Indeed, from our measurements we estimate that the interparticle separation of atoms at these densities is on par with the thermal de Broglie wavelength corresponding to  $g^{(2)} \approx 1.5$ . However, we elect to again treat fluctuations as Poissonian in *lieu* of a more accurate model that could take into account boson correlations. Fig. 6.6 depicts the predictions of our model if we apply the fit parameters extracted from the BEC spectra to the thermal data (experimental parameters in Table 6.2).

Though there is no need to discern a thermal fraction, we do have to contend with non-negligible anharmonicities of the trap. The spacial extent of the thermal samples produced explore a large region of the trap such that a harmonic approximation to the potential is insufficient in describing the density distribution. We therefore employ a numerical calculation of density using the Gaussian geometry of the ODT laser beams (see Appendix A). We find

$n$	$N_{\text{Th}} (10^6)$	$\bar{\omega}/2\pi (\text{s}^{-1})$	$T (\mu\text{K})$	$\rho_0 (10^{14} \text{ cm}^{-3})$
60	1.3 (1)	262 (13)	1.6 (1)	2.5(2)
72	2.5 (3)	222 (11)	1.5 (1)	2.3(2)

Table 6.3: Experimentally determined parameters. Number of atoms in the sample ( $N_{\text{Th}}$ ), temperature ( $T$ ) are determined from time-of-flight-absorption images. The mean trap-frequency  $\bar{\omega}$  is determined from measurements of collective mode frequencies for trapped atoms. Together, these parameters determine the peak density ( $\rho_0$ ).

good agreement between our model and thermal spectra, particularly at  $n = 72$ . Broadening derived from density fluctuations is accounted for in our treatment, though not completely accurate. Our treatment should underestimate the effects of fluctuations given that bosons can experience bunching at high density. However, the effect of these fluctuations is a small perturbation on the spectrum overall in the present experimental regime.

Our model fails in the intermediate and few-body regimes ( $n = 49$  and  $n = 38$ ) where discrete molecular features arise that are accounted for in this description. Nevertheless, we have successfully employed a mean-field description of Rydberg spectra in the many-body regime under a local-density approximation. Aided by consideration of density fluctuations, it reproduces observed spectral measurements.

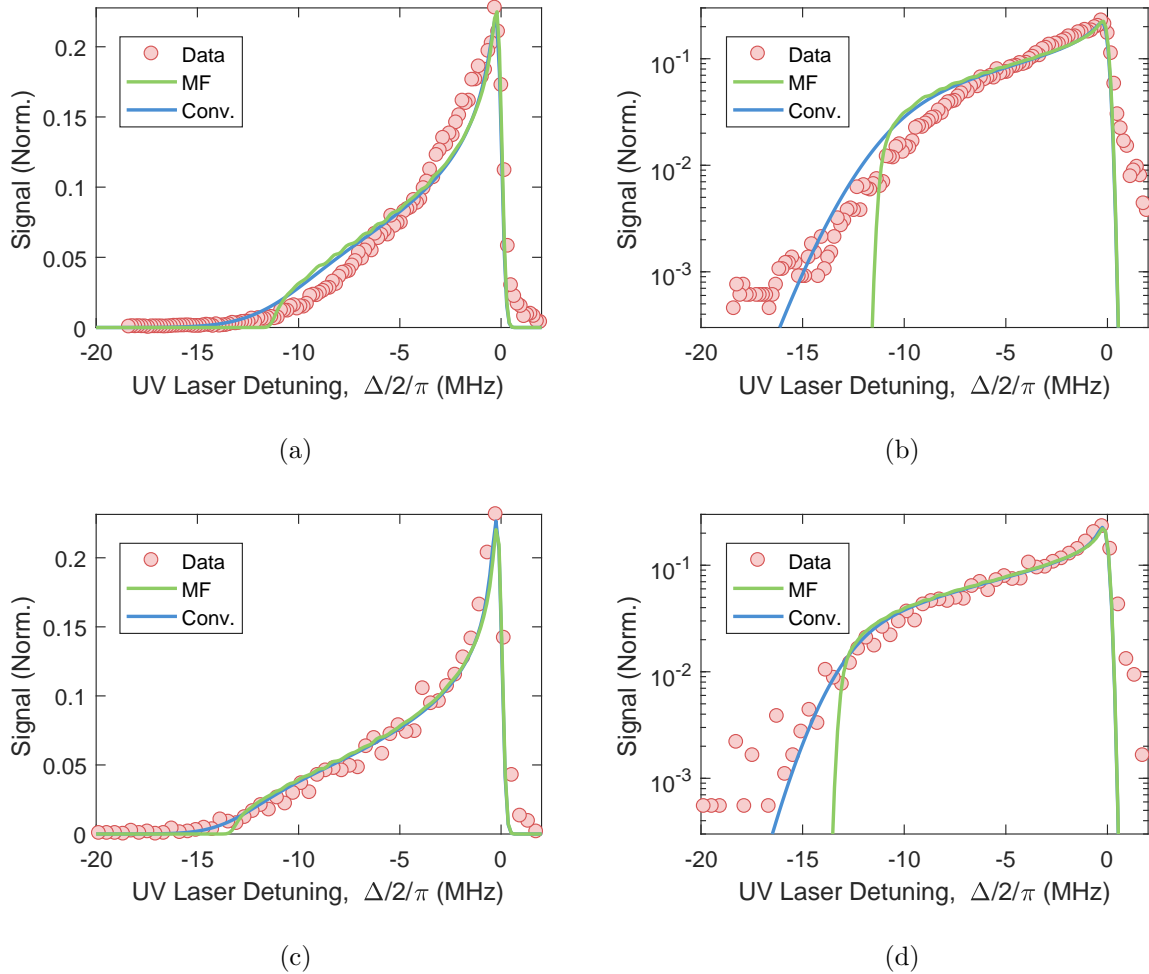


Figure 6.6: Comparison of spectra data, mean-field calculation, and the calculation with the inclusion of convolution with the number of atoms within a Rydberg wavefunction according to 6.18. Top-row:  $n = 60$ , bottom-row:  $n = 72$ , left-column: linear scale, right-column: log scale.



# Chapter 7

## Rydberg Polarons in a Bose-Einstein Condensate

### 7.1 Background

Now we turn to a description of the spectra developed by our collaborators Richard Schmidt, Hossein Sadeghpour, and Eugene Demler [44, 45], which fully describes the quantum and many-body effects using a functional determinant theory (FDT). The spectrum is derived from considering a Rydberg excitation as an impurity that can be modeled using a polaron Hamiltonian. We show that the model is valid across the few- and many-body regimes, which the mean-field theory fails to do. In the intermediate regime ( $n = 49$ ) where spectra demonstrate an amalgamation of discrete molecular features and many-body signal, we find the FDT method to be necessary in order explain the spectrum.

Polarons are quasi-particles consisting of an impurity dressed by excitations in a deformable medium. They were first proposed by Landau [79] to describe the motion of an electron in a lattice where atoms move from their equilibrium positions to screen the electron charge. Polarons play important roles in conduction in ionic crystals and polar semiconductors [80], spin-current transport in organic semiconductors [81], and collective excitations in strongly interacting fermionic and bosonic ultracold gases [82–84]. Unlike polarons of condensed matter systems [85], Rydberg polarons are described by the occupation of localized states bound to the impurity at negative energy.

Rydberg-excitation experiments have been carried out previously in a BEC of Rb [34, 75]. However, Rb excitation spectra are perturbed by a *p*-wave shape resonance [12, 29, 86] for e-Rb scattering, making identification of polaron features challenging. The presence of the *p*-wave resonance in Rb renders the underlying Rydberg molecular potential more complex than Eq. 4.6. In consequence the predicted and observed spectra are very sensitive to microscopic details of the interaction potential. In contrast there is no *p*-wave shape resonance in e-Sr scattering, such that systems of Sr are conducive to accurate theoretical predictions.

The solution of this problem [45] is found by writing the polaronic Hamiltonian of the system as the sum of the bare Hamiltonian (whose solutions are the scattering states of the ODT),  $\hat{H}_0$ , and an impurity-atom interaction term,  $V_{IB}$ ,

$$\hat{H} = \hat{H}_0 + V_{IB}. \quad (7.1)$$

The ground state many-body solution of  $\hat{H}_0$  is the BEC wavefunction,  $|\Psi_{\text{BEC}}\rangle$ . Due to the large energy scale of the impurity-boson interaction, boson-boson interactions are neglected. Thus,  $|\Psi_{\text{BEC}}\rangle$  is constructed from  $N$  particles in the ground single-particle state,  $|s\rangle$ . By driving a single Rydberg transition we diabatically turn on the impurity-boson interaction,

$$V_{IB} = \frac{1}{\mathcal{V}} \sum_{\mathbf{kq}} V(\mathbf{q}) \hat{a}_{\mathbf{k+q}}^\dagger \hat{a}_{\mathbf{k}} |ns\rangle \langle ns| \quad (7.2)$$

where  $\mathbf{k}$  is the boson momentum,  $\mathcal{V}$  is the quantization volume, and  $\hat{a}_{\mathbf{k}}$  ( $\hat{a}_{\mathbf{k}}^\dagger$ ) is the annihilation (creation) operator for the bosons with dispersion  $\epsilon_{\mathbf{k}} = \frac{\hbar^2 \mathbf{k}^2}{2m}$ . The second term,  $V_{IB}$ , which gives rise to polaron formation, describes the Rydberg impurity-boson interaction where  $V(\mathbf{q})$  is the Fourier transform of Eq. 4.6.

The single-particle solutions to Eq. 7.1,  $|\beta\rangle_i$ , which include both scattering as well as bound states (Fig. 7.1), and energies  $\epsilon_i$ , are used to construct the many-body wavefunction solution  $|\Psi\rangle_\gamma$ . From the overlap of  $|\Psi\rangle_{\text{BEC}}$  and  $|\Psi\rangle_\gamma$  one can calculate the many-body spectrum of the Hamiltonian via Fermi's golden rule

$$A(\Delta) \propto \sum_\gamma |\langle \Psi_\gamma | \Psi_{\text{BEC}} \rangle|^2 \delta(\hbar\Delta - (E_\gamma - E_{\text{BEC}})). \quad (7.3)$$

The calculation of  $A(\Delta)$  is couched in terms of the time-dependant overlap

$$S(t) = \langle \Psi_{\text{BEC}} | e^{i\hat{H}_0 t} e^{-i\hat{H}t} | \Psi_{\text{BEC}} \rangle \quad (7.4)$$

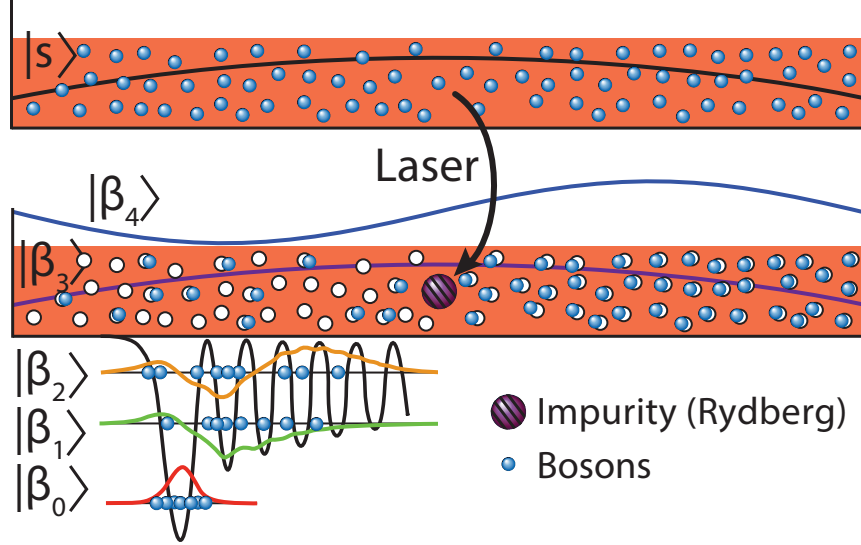


Figure 7.1: Schematic of the excitation of a Rydberg polaron in a uniform-density BEC. Laser excitation projects the system into final configurations involving atoms in bound and scattering states  $|\beta_i\rangle$  that satisfy energy conservation. Bound states are confined in the Rydberg potential  $V(\mathbf{r})$

which is evaluated using the FDT [44] method. The spectrum is then obtained via the Fourier-transform of  $S(t)$ ,

$$A(\Delta) = 2 \operatorname{Re} \left[ \int_0^\infty dt S(t) e^{i\Delta t} \right]. \quad (7.5)$$

Under a local-density approximation, the spectra are determined by averaging over the density distribution,

$$A'(\Delta) \propto \int d^3r \rho(\mathbf{r}) A(\Delta). \quad (7.6)$$

A non-zero thermal-fraction is accounted for by writing the sample density as the sum of BEC and thermal density components (see Appendix B for details). The presence of thermal atoms in the sample results in the large peaks in the spectra at zero-detuning which were unaccounted for by the mean-field description. Their inclusion here yields good agreement with the data.

## 7.2 Results

In Figs. 7.2 and 7.3 we show BEC spectra data along with fitting results from FDT analysis. At  $n = 38$  and  $n = 49$  the number of atoms found within a Rydberg wavefunction is of order  $\sim 1$  and  $\sim 10$ , respectively, *i.e.* this data corresponds to few- and intermediate-body regimes. For these states, molecular lines are resolvable given their sufficiently large binding energies relative to the laser linewidth of 400kHz. There is great agreement between the theoretical and experimental molecular binding energies. Considering data shown in Fig. 7.3 at higher values of  $n$ , the FDT calculations track the data over multiple orders of magnitude and reproduce the many-body continuum at large detunings. The number of atoms within the wavefunctions at  $n = 60$  and  $n = 72$  have increased to  $\sim 50$  and  $\sim 150$ , respectively. As such, these quantum numbers correspond to the many-body regime and no resolved lines, given our laser linewidth, are observed. Under this theoretical framework we can describe the spectra of a Rydberg impurity with great accuracy across the few- to many- body regime.

In Fig. 7.4, the frequency axis is scaled by the fit value of the mean-field shift for the peak density in the BEC,  $-\Delta_0$ , as defined previously in Ch. 6. With this scaling, the mean-field prediction depends solely on  $\Delta/\Delta_0$  and is thus universal. Data and mean-field trace are normalized to yield the same total integral in the absence of thermal contributions to the spectrum. However, the mean-field approach fails to describe the resolved few-body features and the red-detuned tails of the spectra. It is the massive, many-body occupation of quantum bound states gives rise to the formation of the broad tails. Using FDT, we isolate the spectral contribution stemming from a small, central region of the sample with the highest density (shaded regions in Fig. 7.4; obtained for average density  $\langle \rho \rangle = 0.92\rho_0$  and relative standard deviation  $\sqrt{\langle (\Delta\rho)^2 \rangle / \langle \rho \rangle} = 0.04$ ). The agreement with our observations at far red-detuning demonstrates that the tail arises entirely from impurity excitation in the highest density region where the density is essentially constant. The spectral response is nearly gaussian with a width that decreases with increasing  $n$ . This prediction is in agreement with the observed data over an order of magnitude variation in signal strength in the red-detuned tail.

The predicted gaussian profile can be understood by decomposing the spectral function

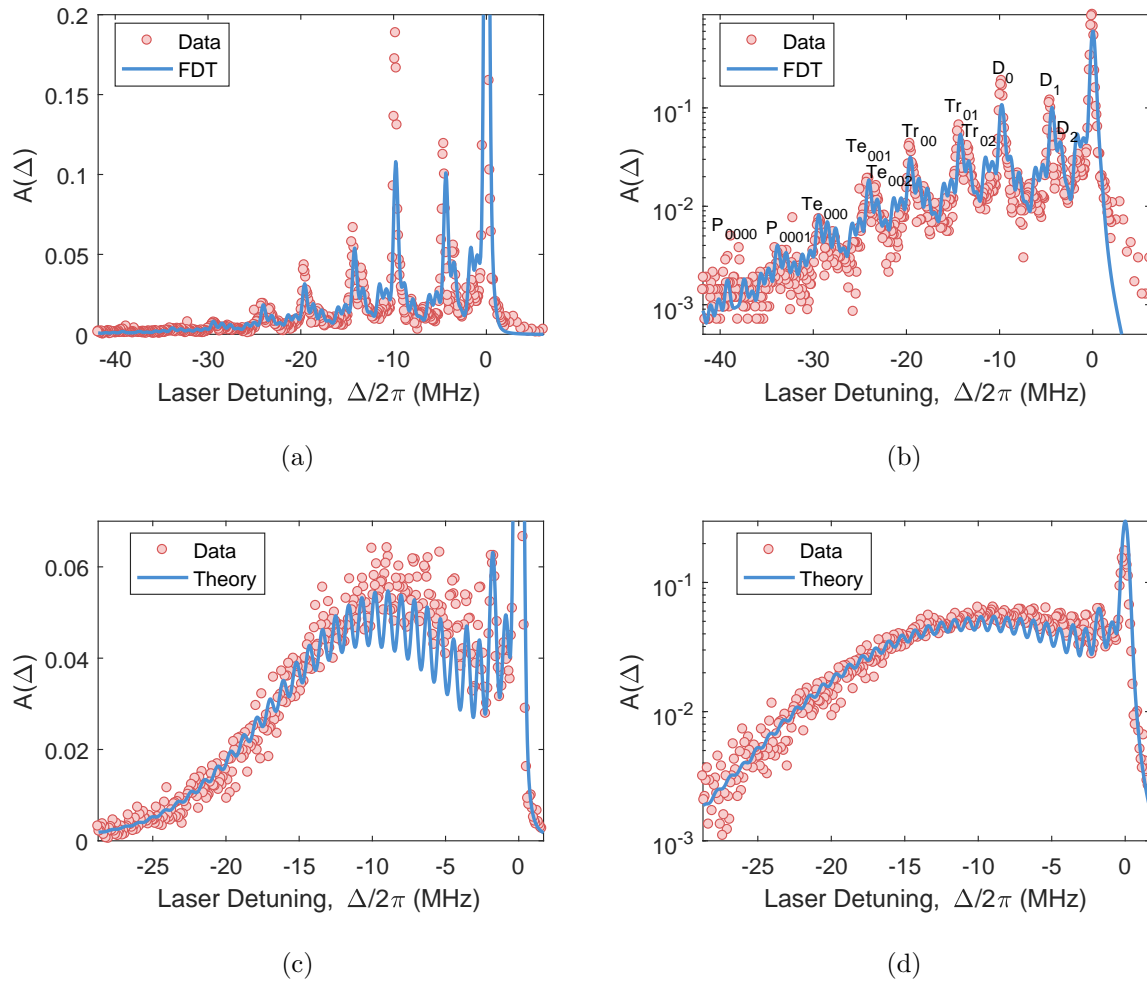


Figure 7.2: BEC spectra data and theory results. Top row:  $n = 38$  data, bottom row:  $n = 49$  data. Left column: data and theory plotted versus laser frequency in linear scale. Right column: log-scale plot of same data.

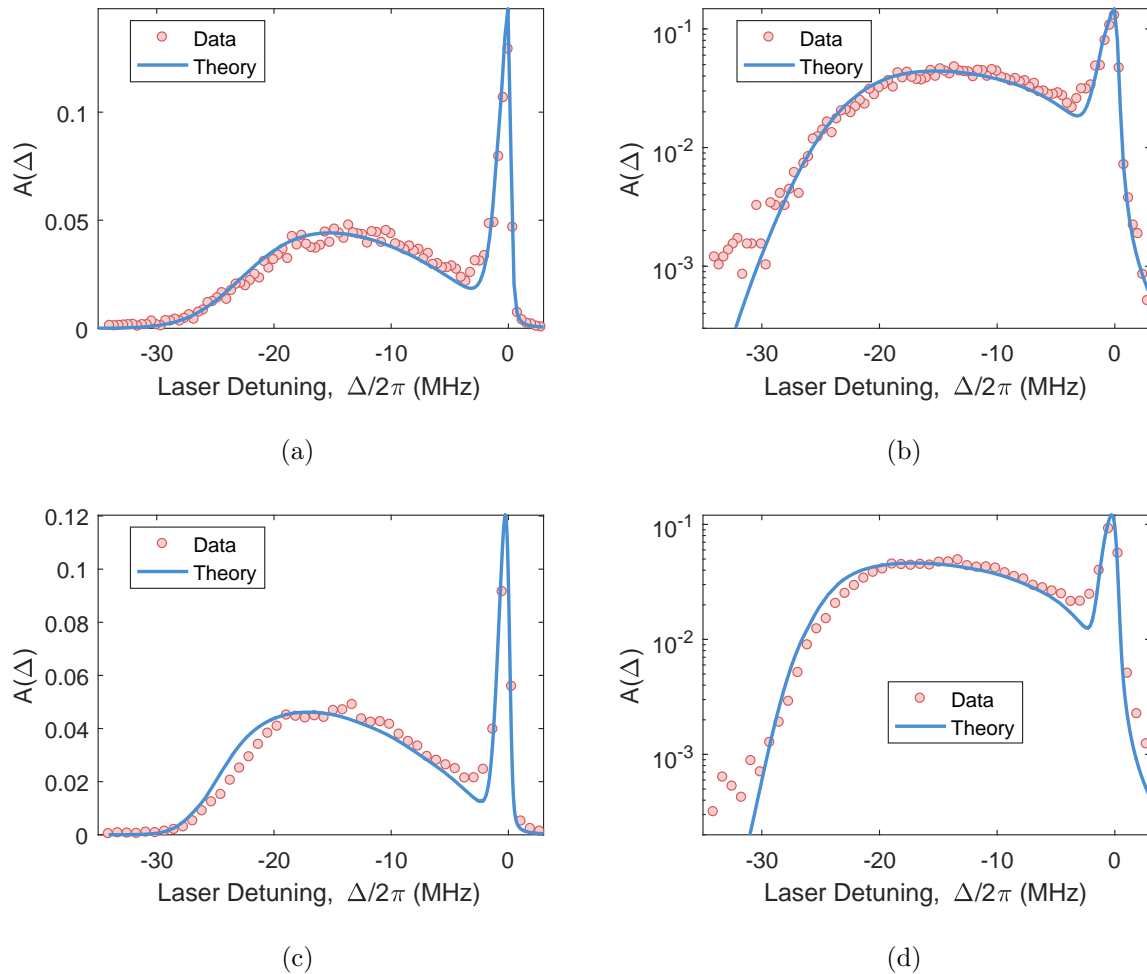


Figure 7.3: BEC spectra data and theory results. Top row:  $n = 60$  data, bottom row:  $n = 72$  data. Left column: data and theory plotted versus laser frequency in linear scale. Right column: log-scale plot of same data.

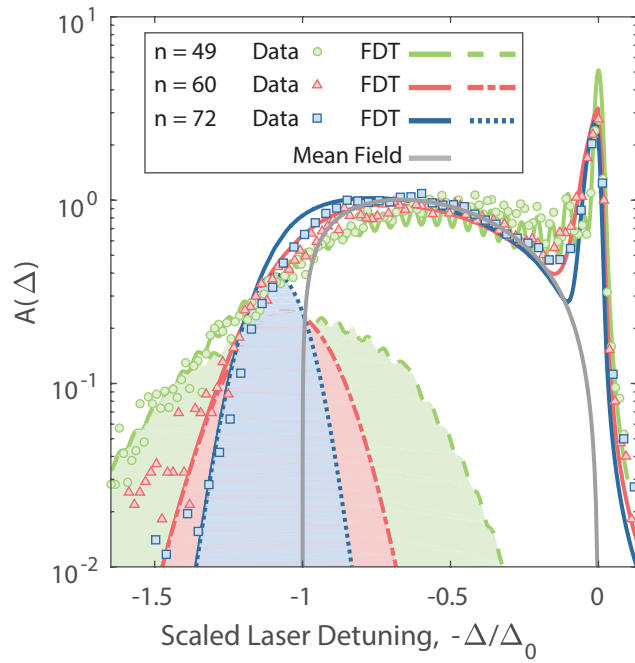


Figure 7.4: Rydberg excitation in the many-body regime for  $n = 49, 60, 72$  with a frequency axis scaled by the mean-field shift at peak density. Symbols are the experimental data. Lines are FDT or mean-field calculations. Laser detuning and signal are scaled as described in the text. The mean-field prediction is for the condensate atoms only. Deviations between the mean-field result and data at small detuning ( $-\Delta/\Delta_0 > -0.3$ ) represent contributions from the non-condensed thermal atoms. The shaded regions represent the predicted polaron response from the center of atom cloud as obtained from FDT. Theory for this high-density region matches the tail of the experimental data and represents the Rydberg-impurity spectral function for a nearly uniform-density region. For uniform density, the width of the spectrum scales as  $n^{-3}$ .

$A(\Delta)$  in terms of excitations from the BEC ground state to interacting single-particle states. The resulting multinomial distribution is dominated by a few terms with large probability  $p_i = |\langle \beta_i | s \rangle|^2$  for bath particles in state  $|s\rangle$  to scatter, via interaction with the impurity atom, into states  $|\beta_i\rangle$ . For a model with  $N$  particles and only two interacting single-particle states, *i.e.* one bound state (*e.g.*  $|\beta_0\rangle$ , Fig. 7.1), with energy  $\epsilon_B$  and overlap  $p_0 \ll 1$ , and one low-energy scattering state (*e.g.*  $|\beta_3\rangle$ ) with energy  $\epsilon_S \simeq 0$  and overlap  $p_3 = 1 - p_0 \simeq 1$ , a binomial distribution results,

$$A(\Delta) = \sum_{j=1}^N \binom{N}{j} p_0^j (1 - p_0)^{N-j} \delta(\hbar\Delta - j\epsilon_B). \quad (7.7)$$

For a large number of particles in the bound molecular state ( $Np_0 \gg 1$ ), Eq. 7.7 becomes a Gaussian with mean energy  $\mu = Np_0\epsilon_B$  and variance  $Np_0(1-p_0)\epsilon_B^2$ . Since the single-particle overlap of  $|s\rangle$  with the bound state  $|\beta_0\rangle$  is small, the gaussian width becomes  $\sqrt{Np_0}\epsilon_B$ . We identify  $Np_0 = N_{\text{Orb}}$  (as defined in Ch. 6), and assume that the gaussian mean energy corresponds to the mean-field energy  $\hbar\Delta$ . The gaussian width then varies as  $\sim \sqrt{\rho}/n^3$ , in agreement with experiment and numerical simulation of the full Hamiltonian (Fig. 7.4).

In conclusion, we present experimental evidence, for the creation of Rydberg polarons consisting of an impurity Rydberg atom dressed by a large number of bound and free excitations of Bose-condensed Sr atoms. Our observations are in remarkable agreement with predictions from FDT that accurately describe the response of a Sr Bose gas to Rydberg-impurity excitation under a wide range of conditions. The red-detuned spectral tail reveals the polaron excitation spectrum in a region of relatively uniform destiny. Important questions remain to be explored, such as whether the interactions are strong enough to lead to self-localization of the impurity, and what connection exists to important concepts in condensed matter physics, such as the effective mass, mobility, and polaron-polaron interactions. The intrinsic quantum nature of the dressing of Rydberg impurities by the many-body environment can be probed in real-time in Ramsey interferometry experiments [87–90].

# Chapter 8

## Conclusion

In this thesis I have described spectral and lifetime studies of Rydberg atomic and molecular states. We've employed strontium which affords us several advantages. The absence of a p-wave shape resonance in electron-Sr scattering is a considerable theoretical simplification. The resulting molecular potential has allowed us to developed a mean-field description in the many-body regime where collisional frequency shifts dominate the line shape. This mean-field model is accurate at high local-density, tantamount to tens or even hundreds of atoms scattering with the Rydberg electron. However, this schemes fails to describe the resolvable molecular lines that are pervasive in spectral measurements at low local-densities. We have found great agreement with a polaronic spectral description that fully accounts for the quantum-statistics of the system in both the few- and many body regimes. Future experimental inquiries could probe the effect of classical versus non-classical spatial density correlations as pertaining to observed density fluctuations. Similarly, theoretical tools could be developed to calculate density fluctuations in the presence of correlated or anti-correlated particles.

We have also explored the decay mechanisms of Sr Rydberg states across density and principal quantum number. In a many-body regime we find associative-ionization and L-changing collisions play a dominate role, much like in Rb Rydberg states. Both of these reactions stem from the attractive Rydberg core-atom potential which sets into motion fast internal dynamics. These studies bring to light strict constraints on experiments involving long coherence times of Rydberg molecular states. Future experiments in the current

apparatus could be served by implementing  $\text{Sr}_2^+$  detection. Decay measurements at higher values of  $n$ , could further probe for possible differences in decay behavior between Sr and Rb. Additionally, the range over which collisional rates are observed should be expanded to further investigate density and  $n$  scaling behavior.

# Appendices



# Appendix A

## Thermal Gas Density

### A.1 Spatial Density Distribution

In this chapter we describe how to calculate the density distribution of a Boltzmann gas given by

$$\rho_{\text{Th}}(\mathbf{r}) = N_{\text{Th}} \frac{e^{-V(\mathbf{r})/k_B T}}{\int d\mathcal{V} e^{-V(\mathbf{r})/k_B T}} \quad (\text{A.1})$$

where the number of thermal atoms in the sample is given by  $N_{\text{Th}}$ . The shape of the density is given by the Boltzmann factor  $e^{-V(\mathbf{r})/k_B T}$ , where  $V(\mathbf{r})$  is the potential landscape, and  $T$  is the sample temperature.

We consider trapping from an ODT where the lasers induce a light-shift of the atom energy levels,

$$V(\mathbf{r}) = -\alpha I(\mathbf{r})/2\epsilon_0 c \quad (\text{A.2})$$

where  $\alpha$  is the polarizability [51]. Using a 1064 nm laser, the polarizability for strontium is  $\alpha = 2364\pi\epsilon_0 a_0^3$  [91, 92], such that laser intensity maxima correspond to potential minima. In the following we consider a trap comprised of one laser beams with its waist at the atoms. These results can be readily generalized for other configurations. The intensity profile is given by the product of two gaussians,

$$I(\mathbf{r}) = I_0 \prod_i \frac{\sigma_{0,i}}{\sigma_i} e^{-2x_i^2/\sigma_i^2}, \quad i = 1, 2 \quad (\text{A.3})$$

where  $I_0$  is the peak beam intensity,  $\sigma_{0,i}$  is the beam waist in the  $i$  Cartesian direction, and  $\sigma_i$  is the size of transverse radius when the intensity has fallen by  $e^{-2}$  with respect to the

intensity at the center of the beam. The peak intensity is given by,

$$I_0 = 2P/\pi\sigma_1\sigma_2 \quad (\text{A.4})$$

where  $P$  is the laser power. The beam is defined to propagate along  $i = 3$ , and as such, the beam size is given by

$$\sigma_i = \sigma_{0,i} [1 + (r_3/R_i)^2]^{1/2} \quad (\text{A.5})$$

where  $r_3$  is the spacial coordinate along the direction of propagation.  $R_i$  is the Rayleigh length,

$$R_i = \pi\sigma_{0,i}^2/\lambda \quad (\text{A.6})$$

where  $\lambda$  is the beam wavelength.

With the trapping beams fully described, we can calculate the potential according to Eq. A.2. To obtain an analytic solution we will take a harmonic approximation at the beam waist,

$$V(\mathbf{r}) = \frac{1}{2}M \sum_i \omega_i^2 x_i^2 - V_0, \quad i = 1, 2, 3. \quad (\text{A.7})$$

Thus we define a potential depth,

$$V_0 = \alpha I_0 / 2\epsilon_0 c \quad (\text{A.8})$$

and trap frequencies,

$$\omega_i = \sqrt{\frac{2V_0}{M\sigma_{0,i}^2}}. \quad (\text{A.9})$$

Note that including gravity modifies the potential, in particular, the trap depth will change by a factor of  $\sim (1 + Mg^2/2\omega^2 V_0)$ . The effect of gravity lowers the potential barrier in the direction of gravity, and at sufficiently low ipower, will result in atoms leaking from the trap. This sets a minimum trap depth below which one cannot continue to implement forced evaporative cooling,  $V_0 = e^{1/2}gM\sigma_{0,i}$ . In addition, gravity will shift the position of the trap minima along the direction of gravity. For gravity along the Cartesian coordinate  $i$ , of the trap geometry, the shift will be a distance  $g/\omega_i^2$ . These corrections should not be ignored when evaporatively cooling down to degeneracy, but is omitted here for simplicity.

With knowledge of the trap frequencies and atom temperature, we can calculate the *shape* of the density distribution,

$$\rho_{\text{Th}} \propto \prod_i e^{-x_i^2/2\sigma_{\text{Th},i}^2}, \quad i = 1, 2, 3 \quad (\text{A.10})$$

where the length scale along each direction is given by

$$\sigma_{\text{Th},i} = (k_B T / M \omega_i^2)^{1/2}. \quad (\text{A.11})$$

Considering the geometric mean trap frequency

$$\bar{\omega} \equiv (\omega_1 \omega_2 \omega_3)^{1/3}, \quad (\text{A.12})$$

it is convenient to define the mean trap radius

$$\sigma_{\text{Th}} = (k_B T / M \bar{\omega}^2)^{1/2}. \quad (\text{A.13})$$

The harmonic approximation is valid when

$$\sigma_{\text{Th},i} / \sigma_{0,i} \ll 1, \quad (\text{A.14})$$

that is, when the size of the beam waist is much larger than the size of the cloud trapped within the beam. The larger an atom cloud is, the more atoms explore anharmonicities of the trap. Equivalently, the harmonic approximation is valid when the sample temperature is small compared to the trap depth,

$$k_B T / V_0 \ll 1. \quad (\text{A.15})$$

Experimentally, the thermal samples we produce yield  $T/V_0 \sim 10$ , which already implies that the harmonic approximation is completely justified. In Appendix A a numerical approach to calculating density is presented which takes into account the gaussian beam geometry and the effect of gravity. Fig. A.1 compares an analytic and numerical (see Section A.4) calculations of a one-dimensional trace of a ODT potential, including the effect of gravity. Most notably, the effective trap depth along the direction of gravity is reduced.

Proceeding from Eq. A.7, we can analytically determine the denominator of Eq. A.1. It is convenient to shift the zero of the potential,  $V(0) \rightarrow 0$ , such that

$$\int dV e^{-V(\mathbf{r})/k_B T} = (2\pi)^{3/2} \sigma_{\text{Th}}^3 \quad (\text{A.16})$$

where we now define the effective volume  $\mathcal{V}_{\text{Eff}} \equiv (2\pi)^{3/2} \sigma_{\text{Th}}^3$  [93, 94].

Additionally, the shift of the zero of the potential gives a convenient way to calculate the peak density

$$\rho_{0,\text{Th}} = N_{\text{Th}} / \mathcal{V}_{\text{Eff}} \quad (\text{A.17})$$

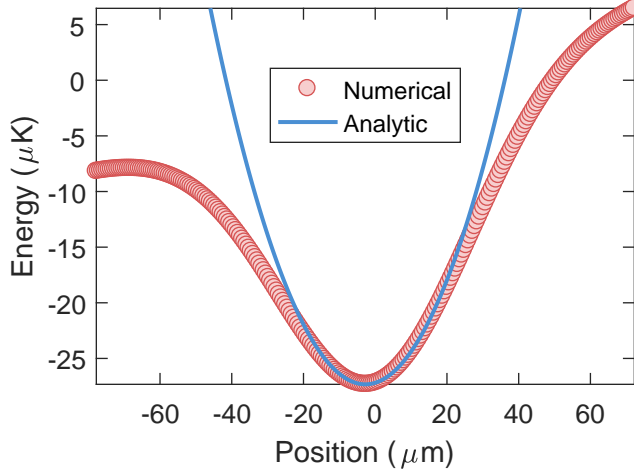


Figure A.1: Trace of numerically calculated potential ( $\bar{\omega} = 2\pi \times 265 \text{ s}^{-1}$ .) along the direction of gravity. Also plotted is an analytic harmonic approximation to the potential. Though the minimum of the trap is  $\sim 40 \mu\text{K}$ , the effect of gravity lowers the effective trap depth to  $\sim 30 \mu\text{K}$ .

Therefore, under a harmonic appoximation, we can write the density distribution as

$$\rho_{\text{Th}}(\mathbf{r}) = \rho_{0,\text{Th}} e^{-V(\mathbf{r})/k_B T}, \quad (\text{A.18})$$

which we have described in terms of various experimental parameters.

## A.2 Density Distribution

In this section we compute the distribution of density  $g(\rho)$ , and we do so with knowledge of the spatial destribution of density  $\rho(\mathbf{r})$ . Integrating  $\rho(\mathbf{r})$  over all space yields the total number of atoms in the system,  $N$ . Similarly, integrating  $g(\rho)$  over all density will also equal  $N$ ,

$$N = \int d\mathcal{V} \rho(\mathbf{r}) = \int d\rho g(\rho). \quad (\text{A.19})$$

To find an expression for  $g(\rho)$ , rewrite  $d\mathcal{V}$  in terms of a function  $f(\rho)$

$$d\mathcal{V} = d\rho f(\rho), \quad (\text{A.20})$$

then Eq. A.19 simplifies to

$$\int d\rho f(\rho) \rho = \int d\rho g(\rho), \quad (\text{A.21})$$

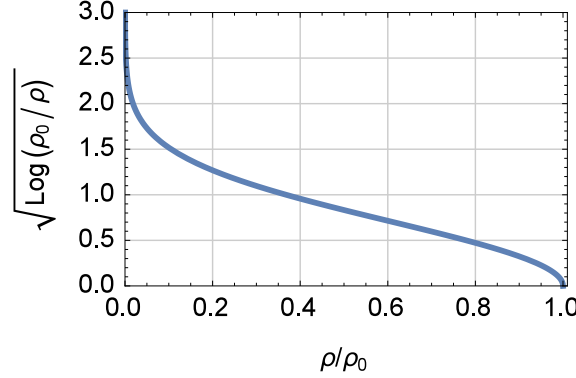


Figure A.2: Plot demonstrating the universal shape of the density distribution of a thermal gas in a harmonic trap.

and we identify

$$g(\rho) = \rho f(\rho). \quad (\text{A.22})$$

The function  $f(\rho)$  is determined given the spatial distribution of density of a system. In the case of a thermal gas density,

$$f(\rho) = \frac{8\pi}{\sqrt{2}} \frac{\sigma^3}{\rho} \sqrt{\log \rho_{0,\text{Th}}/\rho}. \quad (\text{A.23})$$

Thus, the distribution of density of a Boltzmann distributed sample under a harmonic approximation is given by

$$g_{\text{Th}}(\rho) = \frac{8\pi}{\sqrt{2}} \sigma_{\text{Th}}^3 \sqrt{\log \rho_{0,\text{Th}}/\rho}. \quad (\text{A.24})$$

Fig. A.2 plots the shape of  $g_{\text{Th}}(\rho)$ . When parametrized by  $\rho/\rho_0$ , Eq. A.24 has a universal shape applicable to any thermal samples confined by a harmonic potential. Note that although the distribution approaches an asymptote at zero density, the integral over all density is finite.

### A.3 Trap Frequency Measurement

One method of measuring the trap frequencies of a harmonic trap is to give the atom cloud an initial displacement and then measure oscillations of the atom cloud center-of-mass. There are multiple ways to induce an initial displacement, depending on the flexibility of the ODT laser system. The simplest of which is to turn off the trap and allow the atom cloud to fall

under gravity for some amount of time before turning the trap back on. Given that our trap frequencies are each of the order  $\sim 2\pi 100 \text{ s}^{-1}$ , we drop the cloud for  $100\mu\text{s}$  before recapture. After recapturing the cloud, the atoms oscillate within the trap for a variable amount of time. We thus track center of mass versus oscillation time.

We fit to a solution of the atom trajectory in a potential given by Eq. A.7, assuming an initial displacement from the equilibrium position and zero initial velocity. Using Newton's second law of motion we obtain an equation of motion, and add a phenomenological damping term,

$$\ddot{x} = -\omega_i^2 x - 2\Gamma \dot{x}. \quad (\text{A.25})$$

Damping occurs at a rate  $\Gamma$ , and is attributed to collisions of atoms within the gas. Thus, the center-of-mass oscillates as

$$x(t) = A e^{-\Gamma t} \cos\left(\sqrt{\omega^2 + \Gamma^2} + \phi\right). \quad (\text{A.26})$$

Accurate knowledge of trap frequencies is critical of all the experiments described in this work. As such, we measure trap frequencies every time an experiment is conducted within a few hours to minimize systematic discrepancies between the trap frequency measurement result and the experimental conditions. We observe deviations from *a priori* calculations of trap frequencies of  $\sim 10\%$ .

## A.4 Numerical Density Distribution

The validity of the analytically results is contingent on the fidelity of the harmonic approximation of the trapping potential. To investigate deviations from these results, we compute numerically the distribution of density given the gaussian beam geometry of the ODT.

We rewrite the definition of the density distribution  $g(\rho)$ , Eq. A.19, as a discrete sum

$$N = \sum_{q=1}^M N_q = \sum_{q=1}^M \Delta\rho g_q \quad (\text{A.27})$$

where the range of values of density have been discretized into  $M$  bins indexed by  $q$ . The number of atoms within each density bin is given by  $N_q = \Delta\rho g_q$ , where  $\Delta\rho$  is the density

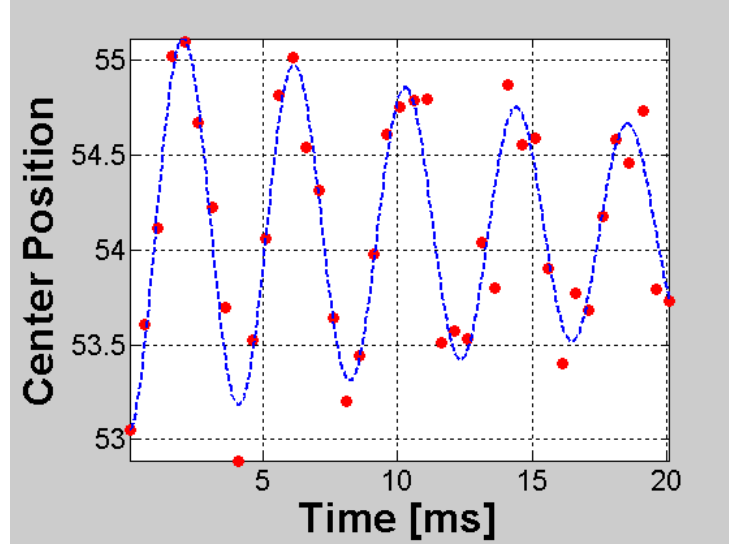


Figure A.3: Example trap frequency oscillation measurement depicting data and fit.

width of a bin. The value of density at each bin is thus

$$\rho_q = q(\Delta\rho - 1/2), \quad q = 1, 2, \dots, M \quad (\text{A.28})$$

In turn, the distribution of density is given by

$$g_q = \Delta\rho N_q. \quad (\text{A.29})$$

The number of atoms corresponding to each density bin is given by,

$$N_q = \sum_{i,j,k} N_{i,j,k} \cdot \Theta\left(\rho_{i,j,k} - \left[\rho_q - \frac{\Delta\rho}{2}\right]\right) \cdot \Theta\left(\left[\rho_q + \frac{\Delta\rho}{2}\right] - \rho_{i,j,k}\right), \quad (\text{A.30})$$

is and  $N_{i,j,k}$  are the sample density and atom number at the spatial coordinate  $x_{i,j,k}$ . Similarly,  $N_{i,j,k}$  is the number of atoms within a volume  $\Delta\mathcal{V}$  of average density  $\rho_{i,j,k}$ ,

$$N_{i,j,k} \equiv \Delta\mathcal{V} \rho_{i,j,k}. \quad (\text{A.31})$$

Note that the resolution of the computation is set by the size of  $\Delta\mathcal{V}$  and  $\Delta\rho$ .

Substituting for Eq. A.30 yields a general expression,

$$g_q = \frac{\Delta\mathcal{V}}{\Delta\rho} \sum_{i,j,k} \rho_{i,j,k} \cdot \Theta\left(\rho_{i,j,k} - \left[\rho_q - \frac{\Delta\rho}{2}\right]\right) \cdot \Theta\left(\left[\rho_q + \frac{\Delta\rho}{2}\right] - \rho_{i,j,k}\right). \quad (\text{A.32})$$

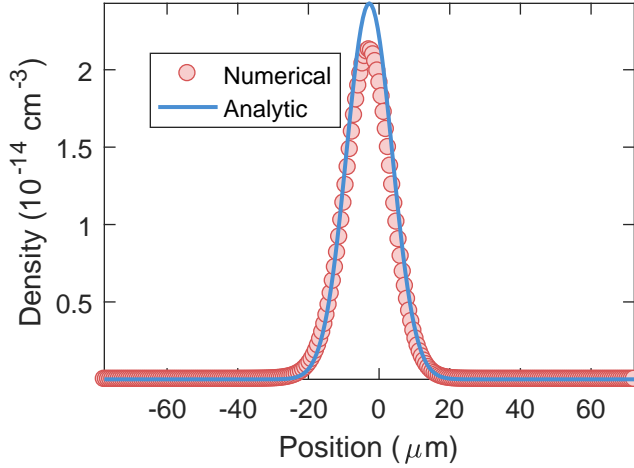


Figure A.4: Trace of numerically calculated spatial density distribution ( $\bar{\omega} = 2\pi \times 222 \text{ s}^{-1}$ ,  $N_{\text{Th}} = 2.5 \times 10^6$ ,  $T = 1.5 \mu\text{K}$ ) along the direction of gravity. Also plotted is an analytic harmonic approximation result. The numerical result indicates a 14% lower peak density which occurs due to atoms occupying regions of space further away from the trap minimum compared to a perfectly harmonic trap, subject to the constraint that the total atom number is the same.

For a thermal gas, following Eq. A.1, we write

$$\rho_{i,j,k} = \frac{N_{\text{Th}}}{\Delta V} \frac{e^{-V_{i,j,k}/k_B T}}{\sum_{i,j,k} e^{-V_{i,j,k}/k_B T}} \quad (\text{A.33})$$

The full potential landscape can be implemented, including both the gaussian beam geometric and the effect of gravity. The same method can be applied to numerically determine the density distribution of a BEC. However, given our trap geometry and typical BEC sizes, the harmonic approximation is adequate and therefore we rely on analytic solutions, see Appendix B. Fig. A.4 compares the spatial density distribution calculated analytically and numerically of a thermal cloud. These calcualtion follow from the potentials presented in Fig. A.1. The analytical solution clearly overestimates the value of peak density in-spite of a sample temperature  $\sim 20$  below the effective trap depth.

Fig. A.5 shows a comparison of an analytic and numerical calculation of  $g(\rho)$  for a thermal cloud. As mentioned previously, the analytic solution overestimates peak-density. However, not only is the peak-density different, the *shape* of  $g(\rho)$  is different as well.

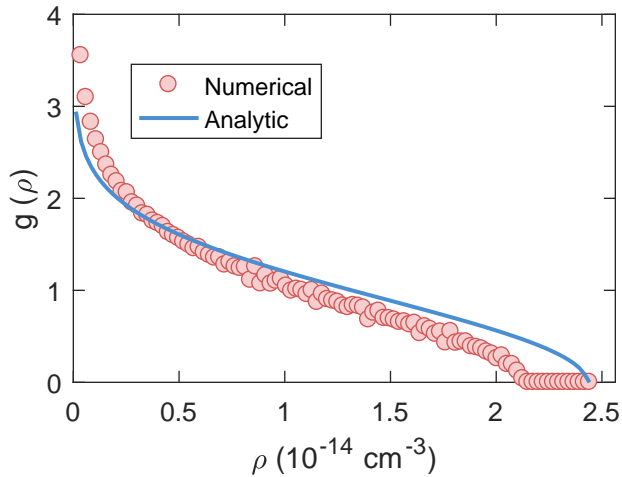


Figure A.5: Here is the distribution of density resulting from the numerical calculation as well as the analytically solution, showing good agreement.

As discussed in Ch. 6, spectra in the many-body regime are related to a sample's density distribution. Fig. A.6 demonstrates the difference in calculating a thermal spectrum depending on an analytic or numerical approach. For either data set prevent, an analytic calculation is clearly an improvement. Note that with either method, the effect of density fluctuations has been incorporated.

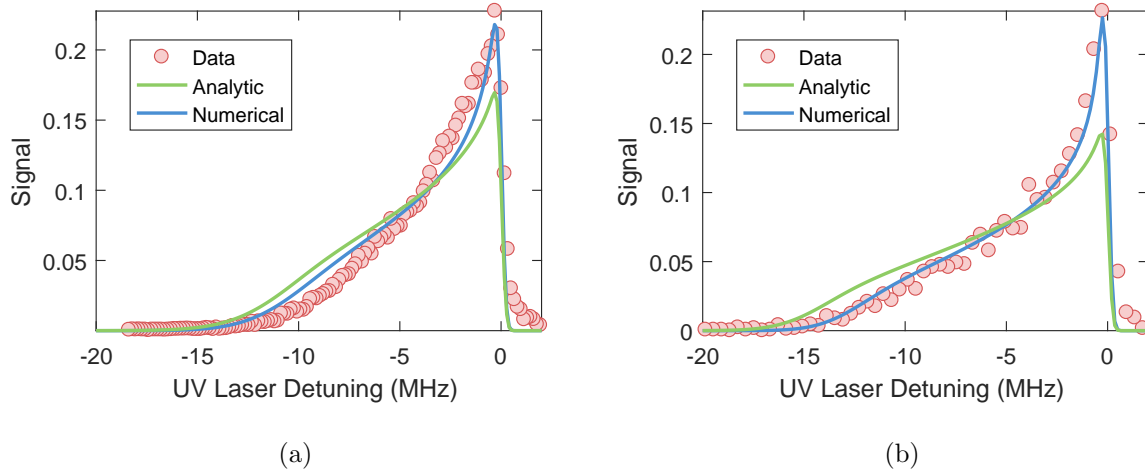


Figure A.6: Mean-field calculations and data for spectra at (a)  $n = 60$  and (b)  $n = 72$ . Both analytic and numerical calculations are presented. Additionally, a correction that accounts for density fluctuations is applied to either method, as described in Ch. 6.

# Appendix B

## BEC Density

### B.1 Density Distribution

With an expression for the BEC spatial density profile, we now seek to calculate the corresponding density distribution,  $g(\rho)$ . Similar to Ch. A, here I describe how we can arrive at expression of the distribution of density of a BEC. Following Pethick and Smith [21] we can calculate the spatial density distribution,  $\rho(\mathbf{r})$  of a BEC in an optical dipole trap as follows. For a BEC with repulsive interaction in a harmonic trap, we can write the spatial density distribution, under a Thomas-Fermi approximation as,

$$\rho_{\text{BEC}}(\mathbf{r}) = \begin{cases} \frac{\mu - V(\mathbf{r})}{U_0} & r < R_{\text{TF}} \\ 0 & r > R_{\text{TF}} \end{cases} \quad (\text{B.1})$$

where  $\mu$  is the chemical potential,  $U_0$  is the effective two-body interaction, and  $R_{\text{TF}}$  is the radius of the BEC,

$$R_{\text{TF}} = \sqrt{\frac{2\mu}{M\bar{\omega}^2}}. \quad (\text{B.2})$$

From the chemical potential,

$$\mu = \frac{\hbar\bar{\omega}}{2} \left( 15N_{\text{BEC}} \frac{a}{\bar{a}} \right)^{2/5} \quad (\text{B.3})$$

we see a  $N_{\text{BEC}}^{2/5}$  dependence on the the number of atoms in the BEC. The atom-atom scattering length for  ${}^{84}\text{Sr}$ - ${}^{84}\text{Sr}$  collisions is  $a = 123a_0$  [54], and

$$\bar{a} = \left( \frac{\hbar}{M\bar{\omega}} \right)^{1/2} \quad (\text{B.4})$$

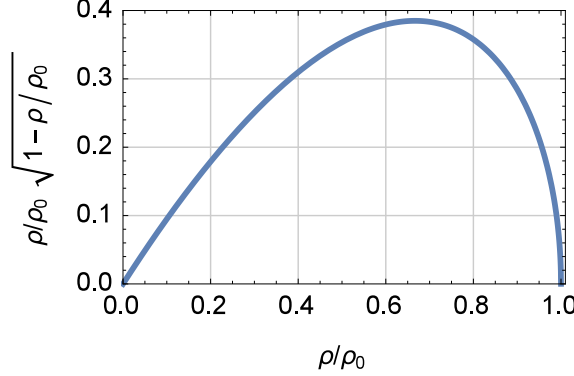


Figure B.1: Plot of the density distribution of a BEC in a harmonic trap, parameterized by  $\rho/\rho_0$ .

is the harmonic oscillator scattering length.  $M$  is the atomic mass, and the two-body interaction is given by,

$$U_0 = \frac{4\pi\hbar^2 a}{M}. \quad (\text{B.5})$$

Because of the small size of the BEC samples we produce ( $\sim 8 \mu\text{m}$ ) compared to the waist size of the ODT beams ( $60 \mu\text{m}$ ), we take harmonic approximation of the trapping potential and take  $V(0) = 0$ . Thus, the peak density of the gas is given by

$$\rho_{0,\text{BEC}} = \mu/U_0 \quad (\text{B.6})$$

Once again, we can reduced the problem of calculating  $g(\rho)$  to finding a function  $f(\rho)$ , defined by Eq. A.20,

$$f(\rho) = -16\pi(2\pi\bar{a}^4 a\rho_0)^{3/2} \left(1 - \frac{\rho}{\rho_0}\right)^{1/2}. \quad (\text{B.7})$$

Thus,

$$g_{\text{BEC}}(\rho) = 2\pi\bar{a}^3 \left(15N_{\text{BEC}} \frac{a}{\bar{a}}\right)^{3/5} \frac{\rho}{\rho_0} \left(1 - \frac{\rho}{\rho_0}\right)^{1/2} \quad (\text{B.8})$$

This results is plotted in Fig. B.1, illustrating the universal shape of the density distribution for condensates trapped in a harmonic trap.

## B.2 Two-Component BEC

Experimentally, the samples we produce always retain some fraction of the atoms in a thermal phase. In this section, I present an analytic description of a two-component sample. We

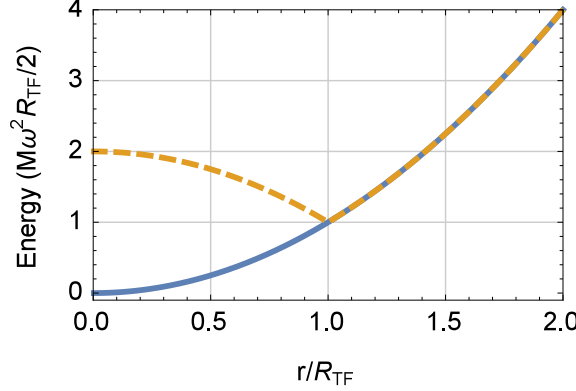


Figure B.2: Plot of harmonic potential (blue) and modified potential Eq. B.10 (dashed yellow) for thermal atoms in two-component atomic cloud. The rise in energy below the Thomas-Fermi radius results in decreasing density away from the edge of the BEC.

rewrite the spatial density distribution of the system as the sum of a BEC and thermal components [45, 95],

$$\rho(\mathbf{r}) = \rho_{\text{BEC}} + \rho'_{\text{Th}} \quad (\text{B.9})$$

Take  $\rho_{\text{BEC}}$  to be defined by Eq. B.1. The thermal component follows Eq. A.1, but in determining  $V(\mathbf{r})$ , we include atom-atom interactions

$$V(\mathbf{r}) \rightarrow V(\mathbf{r}) + 2 U_0 \rho(\mathbf{r}). \quad (\text{B.10})$$

Furthermore, we assume that the perturbation of the potential landscape is dominated by the presence of BEC atoms, and so take  $\rho(\mathbf{r}) \rightarrow \rho_{\text{BEC}}(\mathbf{r})$  in Eq. B.10 [96] resulting in

$$V(\mathbf{r}) = \begin{cases} \frac{1}{2} M \bar{\omega}^2 (2R_{\text{TF}}^2 - r^2) & r < R_{\text{TF}} \\ \frac{1}{2} M \bar{\omega}^2 r^2 & r > R_{\text{TF}} \end{cases} \quad (\text{B.11})$$

Fig. B.2 demonstrates the effect of including atom-atom interactions in the potential experienced by thermal atoms.

Next we reevaluate the effective volume of the thermal atoms, Eq. A.16,

$$\mathcal{V}'_{\text{Eff}} = \mathcal{V}_{\text{Eff}} \left\{ \frac{1}{8\sqrt{\pi}} e^{-x^2} \left[ x - \frac{1}{4} D(x) \right] + \text{erfc}(x) \right\}, \quad x \equiv \frac{1}{\sqrt{2}} \frac{R_{\text{TF}}}{\sigma_{\text{Th}}}, \quad (\text{B.12})$$

where  $D(x)$  is the Dawson integral

$$D(x) \equiv e^{-x^2} \int_0^x e^{y^2} dy \quad (\text{B.13})$$

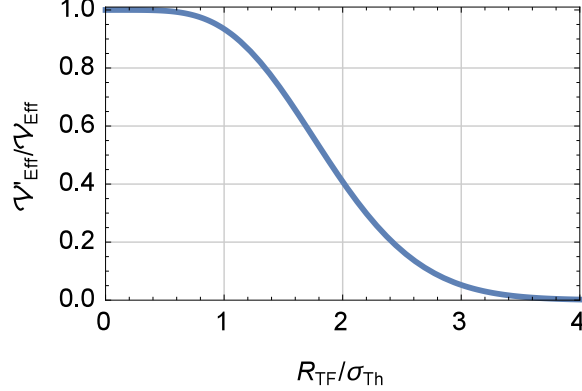


Figure B.3: Plot of modified  $\mathcal{V}'_{\text{Eff}}$  versus the ratio of the Thomas-Fermi radius to the thermal cloud width.

and  $\text{erfc}(x)$  is the complementary error function

$$\text{erfc}(x) \equiv \frac{2}{\sqrt{\pi}} \int_x^{\infty} e^{-y^2} dy. \quad (\text{B.14})$$

The modified effective volume monotonically decreases as a function of  $R_{\text{TF}}/\sigma_{\text{Th}}$ , at a value of  $R_{\text{TF}}/\sigma_{\text{Th}} = 1$  the effective volume has decreased by 7% relative to  $\mathcal{V}_{\text{Eff}}$ , Fig. B.3.

We can now write an expression for the thermal density, and we do so in terms of  $\rho_{\text{Th}}$ , the thermal density in the absence of interactions,

$$\rho'_{\text{Th}}(\mathbf{r}) = \begin{cases} \frac{\mathcal{V}'_{\text{Eff}} \rho_{\text{Th}}^2(R_{\text{TF}})}{\mathcal{V}_{\text{Eff}} \rho_{\text{Th}}(r)} & , r < R_{\text{TF}} \\ \frac{\mathcal{V}'_{\text{Eff}}}{\mathcal{V}_{\text{Eff}}} \rho_{\text{Th}}(r) & , r > R_{\text{TF}} \end{cases} \quad (\text{B.15})$$

In Fig. B.4, I compare the sample density with and without a thermal fraction. From this plot it is clearly evident that the peak-density will have some contribution due to thermal atoms, though experimentally this is negligible.

Following the recipe we have previously, we again determine an expression for the distribution of density. However, the expression is discontinuous because although the spatial density distribution is a piece-wise continuous function, the first derivative is not.

$$g'(\rho) = \begin{cases} g_{\text{Th}}(\rho) \sqrt{1 + \frac{\log(\mathcal{V}'_{\text{Eff}}/\mathcal{V}_{\text{Eff}})}{\log(\rho_{0,\text{Th}}/\rho)}} & , \rho < \rho(R_{\text{TF}}) \\ \frac{g_{\text{BEC}}(\rho)}{1 + f(\rho)} \sqrt{1 - \frac{f(\rho)/x^2}{1 - \rho/\rho_{0,\text{BEC}}}} & , \rho > \rho(R_{\text{TF}}) \end{cases} \quad (\text{B.16})$$

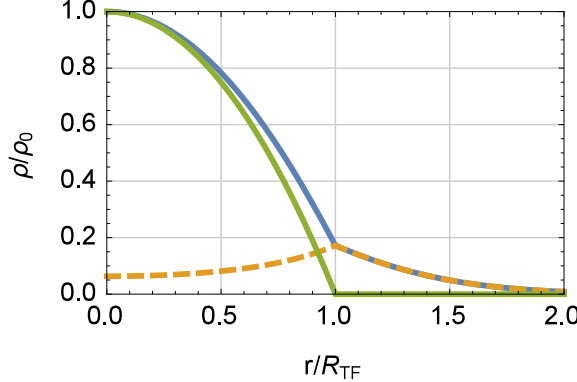


Figure B.4: Plot of BEC density (green), two-component thermal density (dashed yellow) and the sum (blue).

where

$$\begin{aligned} f(\rho) &\equiv \text{ProductLog} \left[ \frac{V'}{V} \frac{\rho_{0,\text{Th}}}{\tilde{\rho}} e^{-\rho/\tilde{\rho}-x^2} \right] \\ \tilde{\rho} &\equiv M\sigma_{\text{Th}}^2 \bar{\omega}^2 / U_0 \\ x &\equiv \frac{1}{\sqrt{2}} \frac{R_{\text{TF}}}{\sigma_{\text{Th}}} \end{aligned} \quad (\text{B.17})$$

Note that Eq. B.16 limits to  $g_{\text{Th}}(\rho)$  when  $\sigma_{\text{Th}} \rightarrow 0$ , and similarly Eq. B.16 limits to  $g_{\text{BEC}}(\rho)$  when  $R_{\text{TF}} \rightarrow 0$ .

### B.3 BEC Trap Frequency and Peak-Density Measurement

We use Castin Dum to determine trap frequencies. We assume cylindrical symmetry from the geometry of the trap. F. Dalfovo, S. Giorgini, L. P. Pitaevskii, and S. Stringari, Rev. Mod. Phys. 71, 463 (1999). Y. Castin and R. Dum, Phys. Rev. Lett. 77, 5315 (1996). Martinez PRL 103, 200402 (2009) Using a time-of-flight measurement we can determine the axial and radial trap frequencies from Castin-Dum fitting to the expansion of the cloud size. The cloud radii is given by the product of the initial radii times the scaling parameters in each direction,

$$R_{\text{TF},i}(t) = R_{\text{TF},i} b_i(t) \quad (\text{B.18})$$

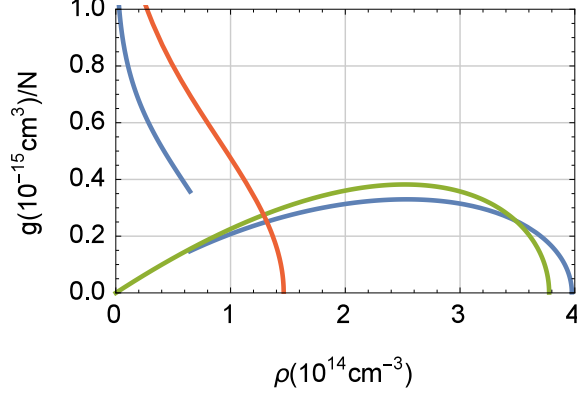


Figure B.5: Plot of BEC density distribution (green), thermal gas density distribution (red), and two-component cloud density distribution (blue). The same parameters are used for each trace, each trace is also normalized by the number of atoms such that the integral of each trace is unity.

The initial radii are taken to be the Thomas-Fermi radii, Eq. B.2. The scaling parameters obey the following second-order ordinary differential equation,

$$\ddot{b}_i(t) = \frac{\omega_i^2}{b_i b_x b_y b_z}. \quad (\text{B.19})$$

This set of three equations can be reduced by one given that the optical dipole trap is cylindrically symmetric, additionally, time is rescaled to be unitless,

$$\tau = \omega_r t \quad (\text{B.20})$$

$$\ddot{b}_r(\tau) = \frac{1}{b_r^3 b_z} \quad (\text{B.21})$$

$$\ddot{b}_z(\tau) = \frac{\lambda^2}{b_r^2 b_z^2} \quad (\text{B.22})$$

where  $\lambda = \omega_z / \omega_r$ . For ease of computation we further transform this set of two second-order differential equations into a set of four first-order equations.

$$\dot{b}_r(\tau) = \beta_r \quad (\text{B.23})$$

$$\dot{\beta}_r(\tau) = \frac{1}{b_r^3 b_z} \quad (\text{B.24})$$

$$\dot{b}_z(\tau) = \beta_z \quad (\text{B.25})$$

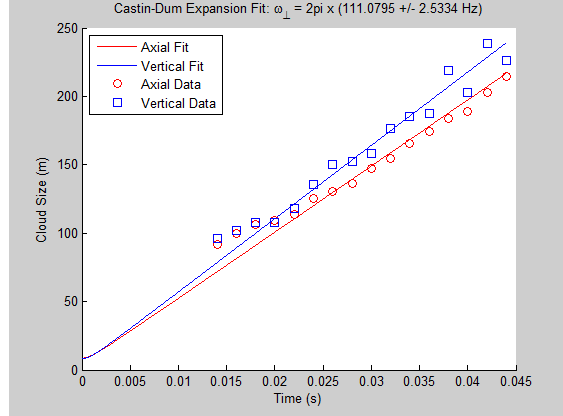


Figure B.6: Time of flight results for the width of the cloud in vertical and radial direction in addition to Casin-Dum fit results.

$$\dot{\beta}_z(\tau) = \frac{\lambda^2}{b_r^2 b_z^2} \quad (\text{B.26})$$

Because the initial size of the cloud equals  $R_{\text{TF},i}$ , we set  $b_i(0) = 1$ . In addition, because the cloud is initially stationary, we set  $\beta_i(0) = 0$ .

## B.4 Transition Temperature

The number of atoms in excited states is given by

$$N_{\text{Th}} = \int_0^\infty d\epsilon g(\epsilon) f^0(\epsilon) \quad (\text{B.27})$$

where  $\epsilon$  is the state energy,  $g(\epsilon)$  is the density of states, and  $f^0(\epsilon)$  is the Boltzmann Distribution. The density of states is given by

$$g(\epsilon) = C_\alpha \epsilon^{\alpha-1}. \quad (\text{B.28})$$

For a three-dimensional harmonic trap  $\alpha = 3$  and

$$C_3 = \frac{1}{2\hbar^3 \bar{\omega}^3} \quad (\text{B.29})$$

The critical temperature,  $T_c$ , is defined to be the highest temperature at which the lowest-energy state is occupied. To find,  $T_c$ , we impose that all atoms are in excited states with  $\mu = 0$ , which maximizes Eq. B.27. It follows that

$$N_{\text{Th}} = C_\alpha \Gamma(\alpha) \zeta(\alpha) (k_B T)^\alpha, \quad (\text{B.30})$$

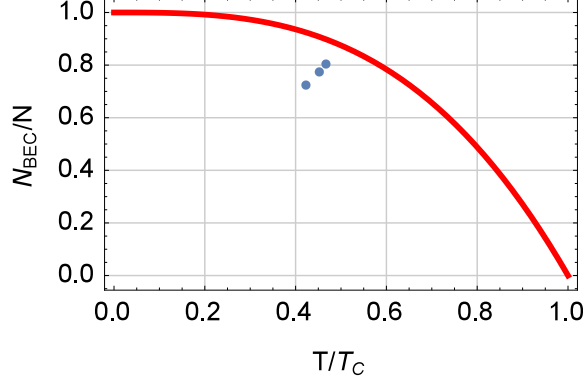


Figure B.7: Plot of BEC fraction as a function of the ratio of temperature to critical temperature for a three-dimensional harmonic trap ( $\alpha = 3$ ). Similar results have been observed [97]

where  $\Gamma(\alpha)$  is the gamma function and  $\zeta(\alpha)$  is the Riemann zeta function. For a three-dimensional harmonic trap we find the value of critical temperature when all the atoms are in the thermal state

$$N_{\text{Th}}(T = T_{\text{Th}}) = N \quad (\text{B.31})$$

$$k_B T_c \simeq 0.94 \hbar \bar{\omega} N^{1/3}. \quad (\text{B.32})$$

## B.5 BEC Fraction

Experimentally, we do not produce pure BEC's; some fraction of the atoms will remain in a thermal state. We are interested in knowing this fraction because it affects the density distribution of the atom cloud. We can calculate the

Revisiting Eqs. B.30 and B.31 we relate the thermal fraction to the ratio of temperature to critical temperature

$$N_{\text{Th}}/N = (T/T_c)^\alpha. \quad (\text{B.33})$$

Since the sum of the number of atoms in the thermal state and BEC state must equal the total number of atoms, it follows that the BEC fraction can be expressed as

$$N_{\text{BEC}}/N = 1 - (T/T_c)^\alpha. \quad (\text{B.34})$$

## **Appendix C**

### **Magnetic Field Zeroing**

We can use the known landua g factor to calibrate voltage to magnetic field. Experimentally we tried to align the electric and magnetic fields in the region of the atoms but see broadening of SFI spectra away from zero-field. During the MOT phases we choose values of field to optimize loading but once the atoms are in the ODT we switch to zero-field settings before conducting any experiments.

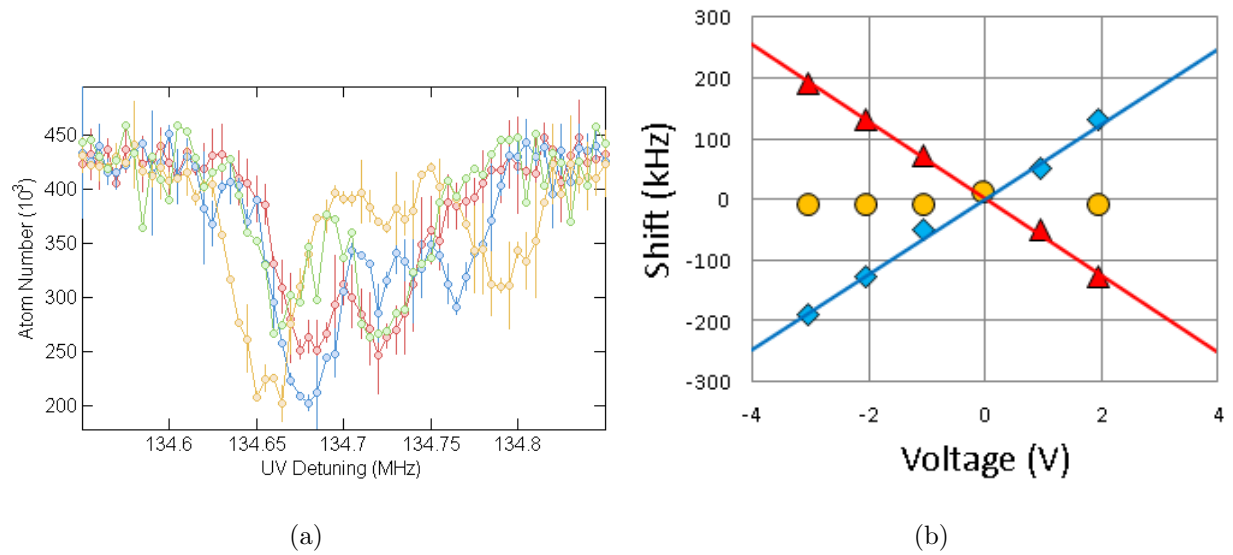


Figure C.1: (a) Image of top-hat configuration on CCD camera. (b) Traces of ODT beams before and after converging to a single beam.

## Appendix D

### Ionization Electrode Design

I modeled the design for the ionization electrode on previous work, in particular [98]. Some design choices that I made were to maximize the size of the electrodes such that the field in the region of the atoms was insensitive to stray charge anywhere in the viewports. Extra field plates where used for the express purpose of guiding charged particles towards the MCP. Though at low field values, these extra plates are not necessary, with sufficiently high field charged particles will begin to collide with the ionization electrodes instead of the MPC. This is because the MCP will not also increase in potential, such that eventually it become energetically unfavorable for the particles to move towards the MCP. The spacing between the electrodes and any other conductive part of the chamber (which will be held at ground) sets a maximum potential difference across the two which can be achievement, but this only arises if low values of principal quantum number are desired,  $n < 25$ . Additionally, the addition of an assortment of materials increases the risk of being able to achieve ultra-high vacuum. We do not have direct evidence suffering from this, however the ODT trap lifetime of 10 s points to vacuum problems. This has not been an issue to do out ability to load atoms quickly, and conduct experiments fast compared to 10 s.

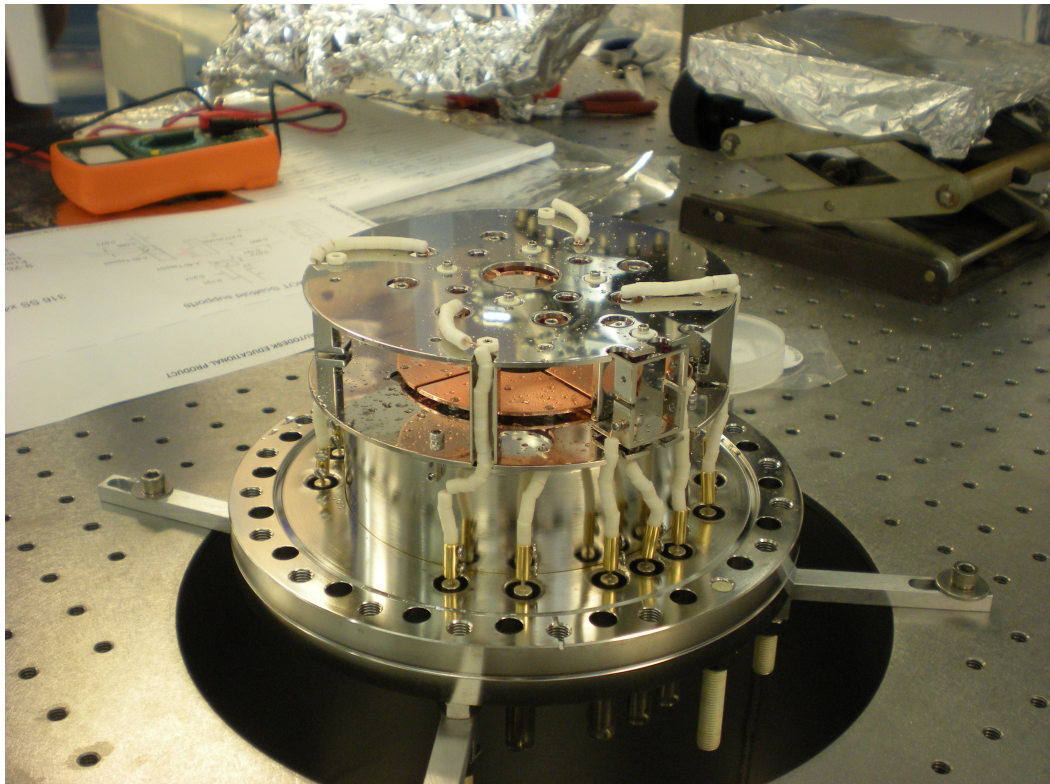


Figure D.1: Full electrode assembly attached to the bottom vacuum flange. Some of the electrodes are pictured (copper). Each electrode is connected to a feedthrough on the bottom flange via copper wire insulated by ceramic spacers.

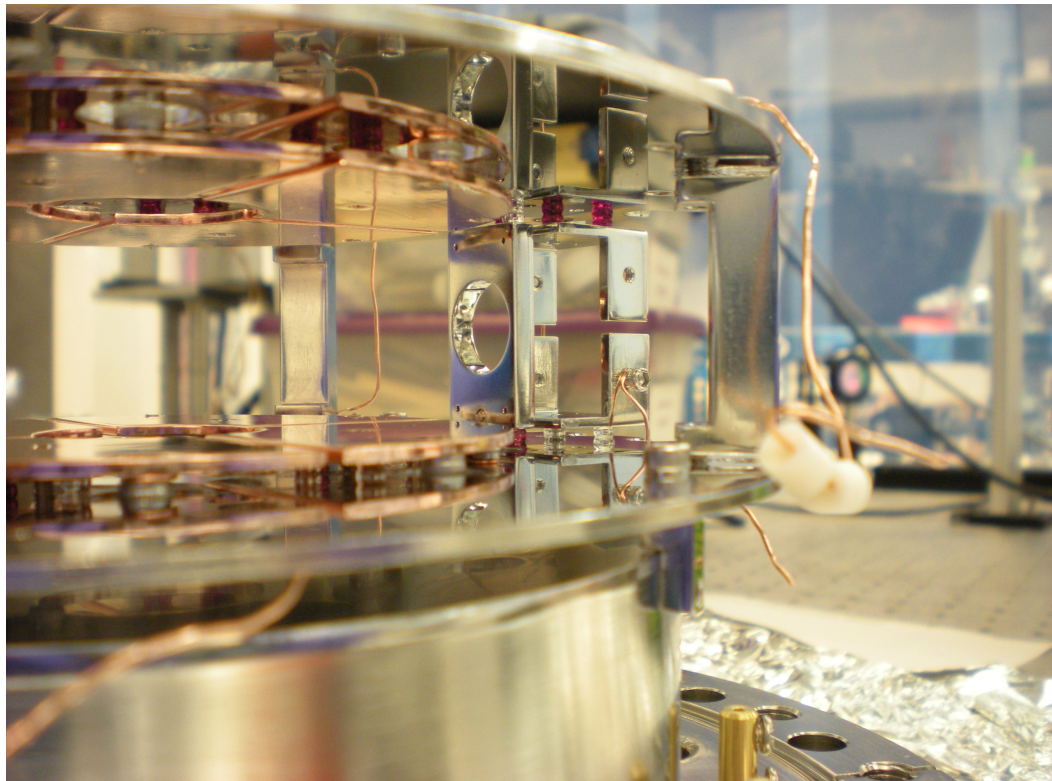


Figure D.2: Side view of the electrode assembly. Pictured are some of the ionization electrodes, the lensing and vertical guiding plates, as well as the sapphire spheres (pink) used to set the spacing between the electrodes and the scaffold. The electrodes are held in place with bolts insulated from the electrodes using ceramic washers.

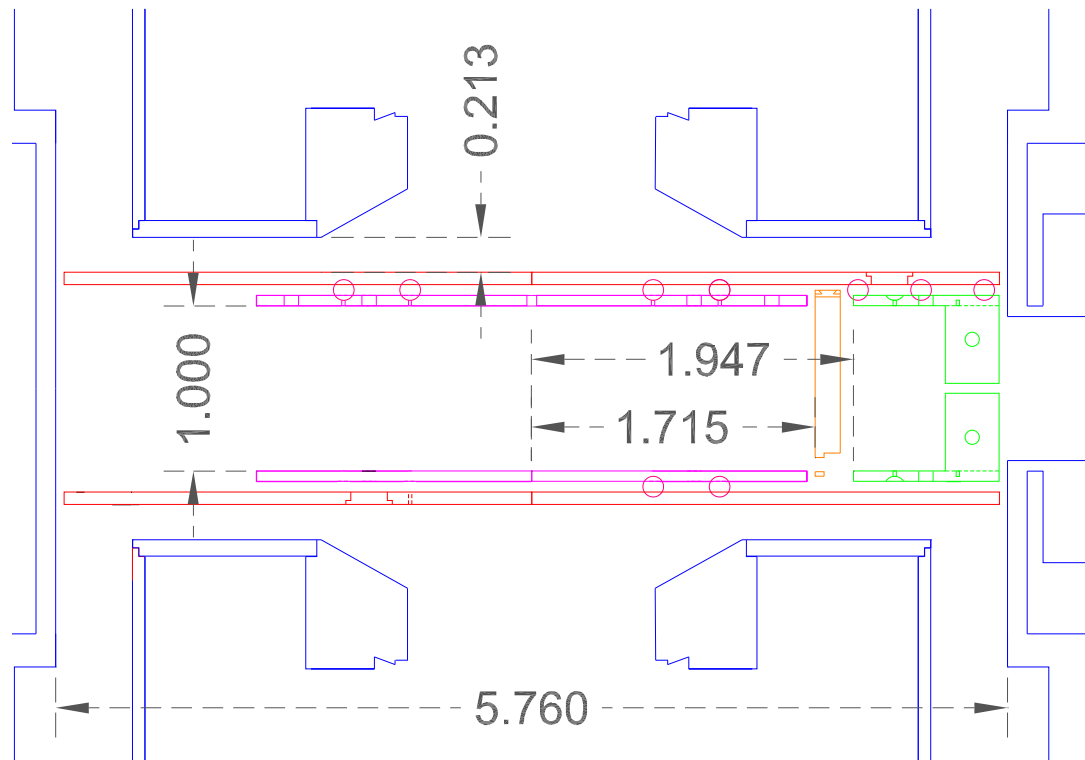


Figure D.3: Assembly of electrodes (pink) within the vacuum chamber (blue), the electrodes are suspended by but not in direct contact with a pair of scaffold plates (red). Also pictured is the lensing plate (orange) and the vertical guideing plates (green).

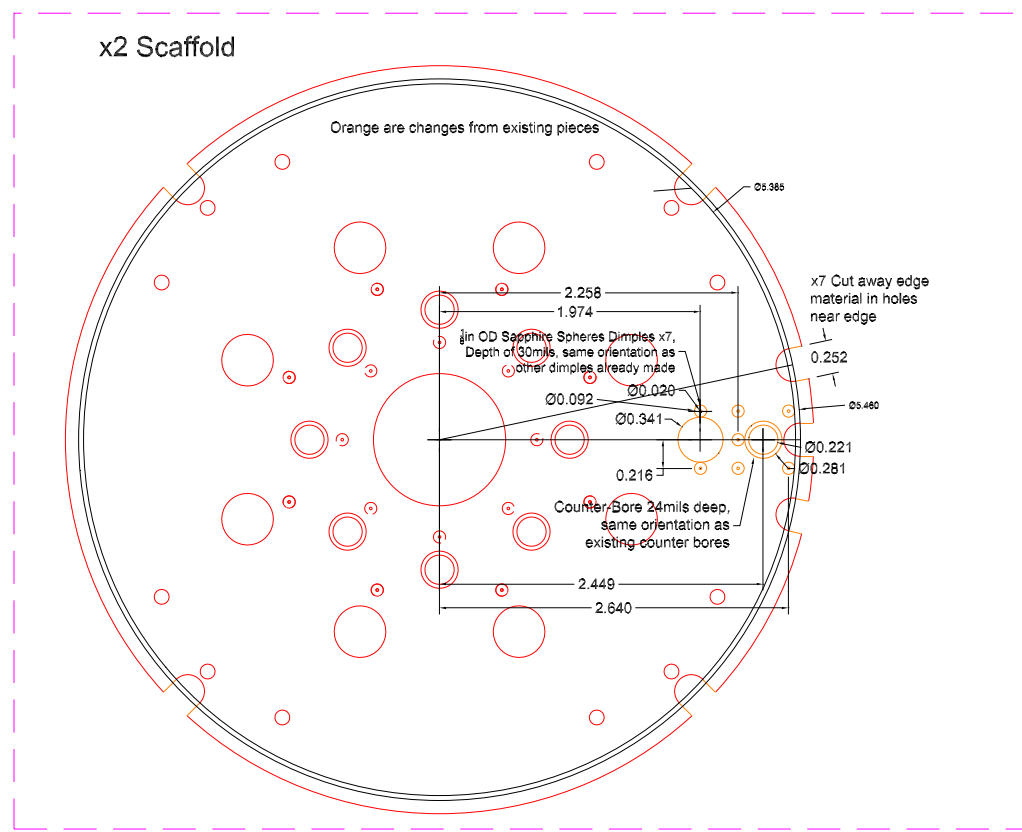


Figure D.4: Scaffold used to suspend ionization electrodes.

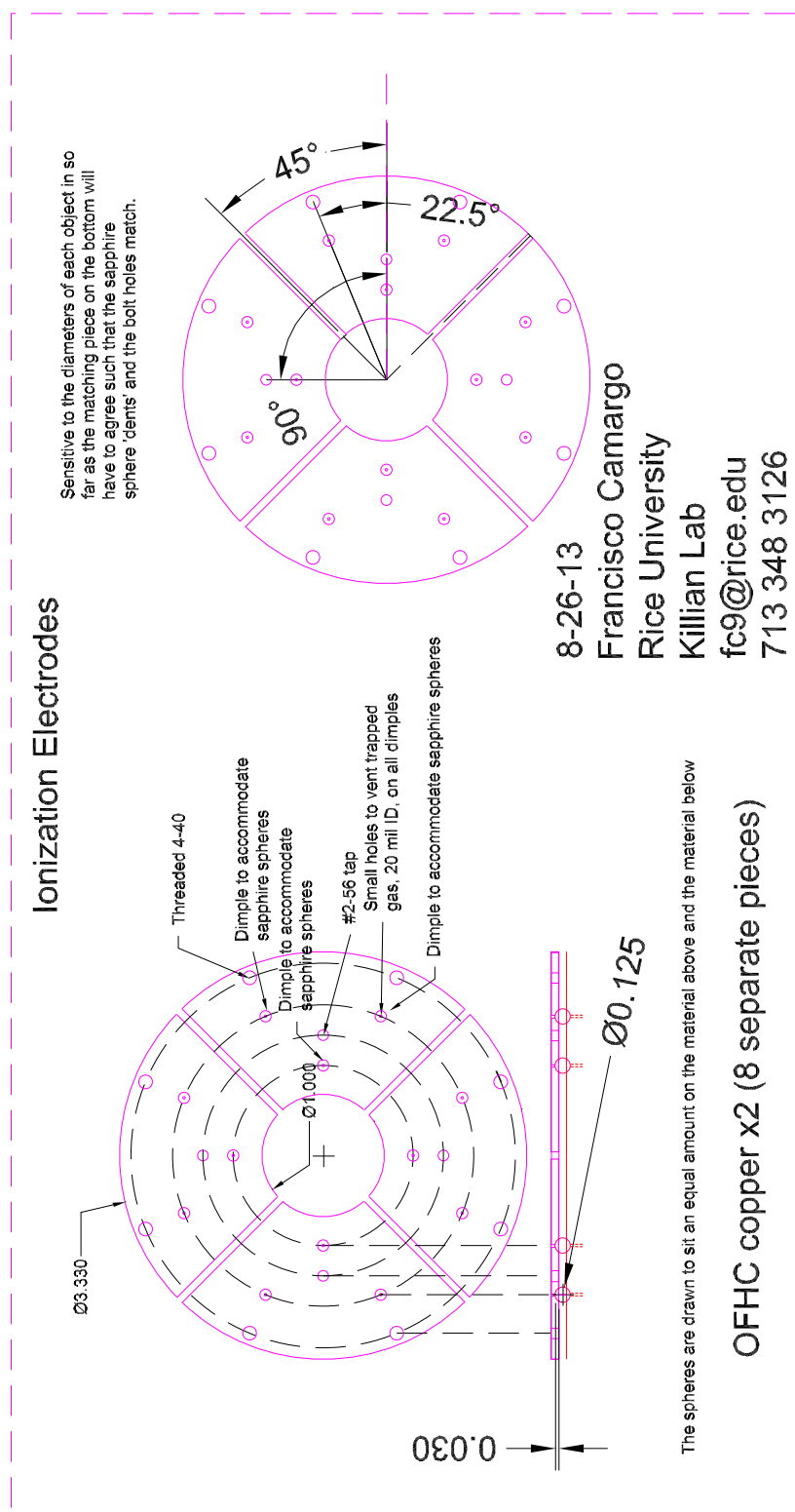


Figure D.5: Ionization electrode plates.

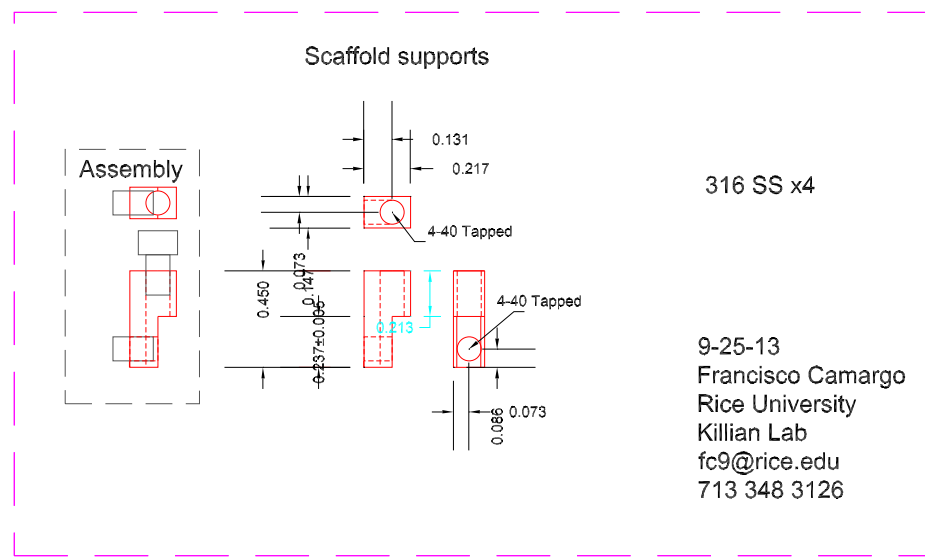


Figure D.6: Support pieces used to attach scaffold to bottom chamber flange.

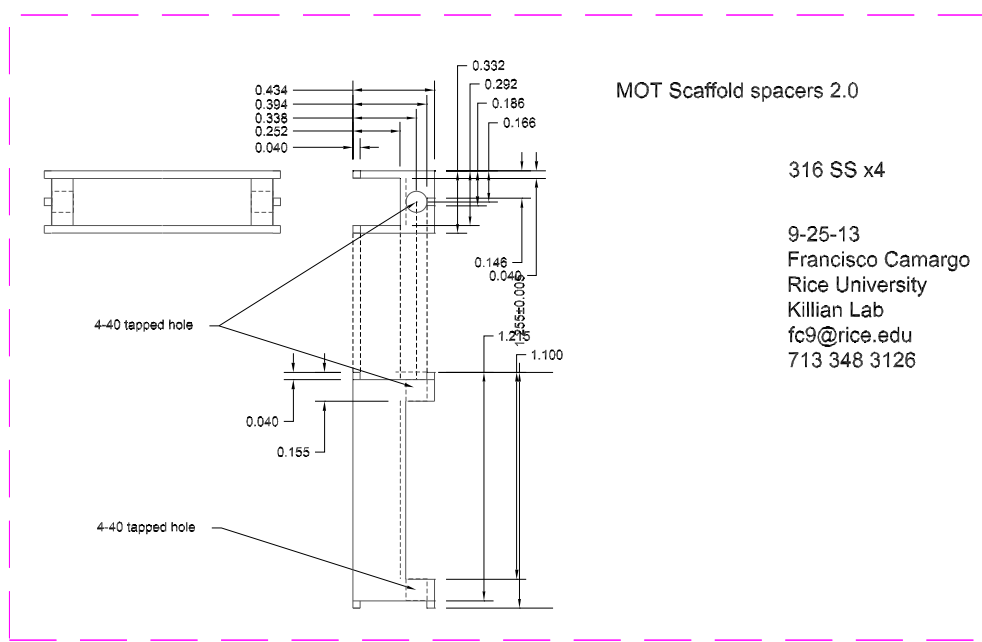


Figure D.7: Support pieces used to support top scaffold.

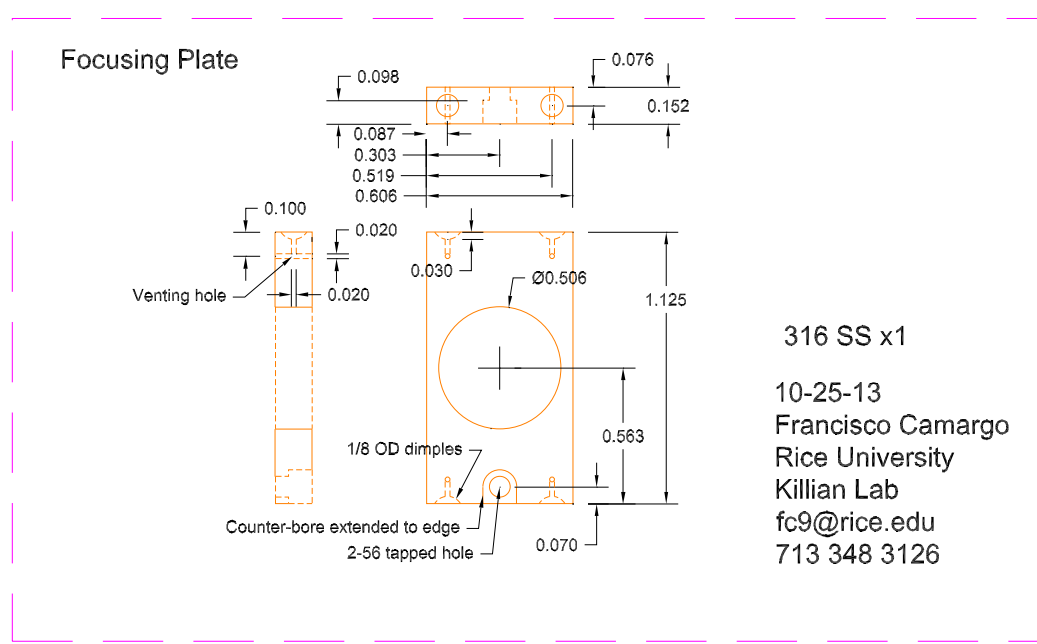


Figure D.8: Lensing plate used to focus path of electrons as they traverse towards the MCP.

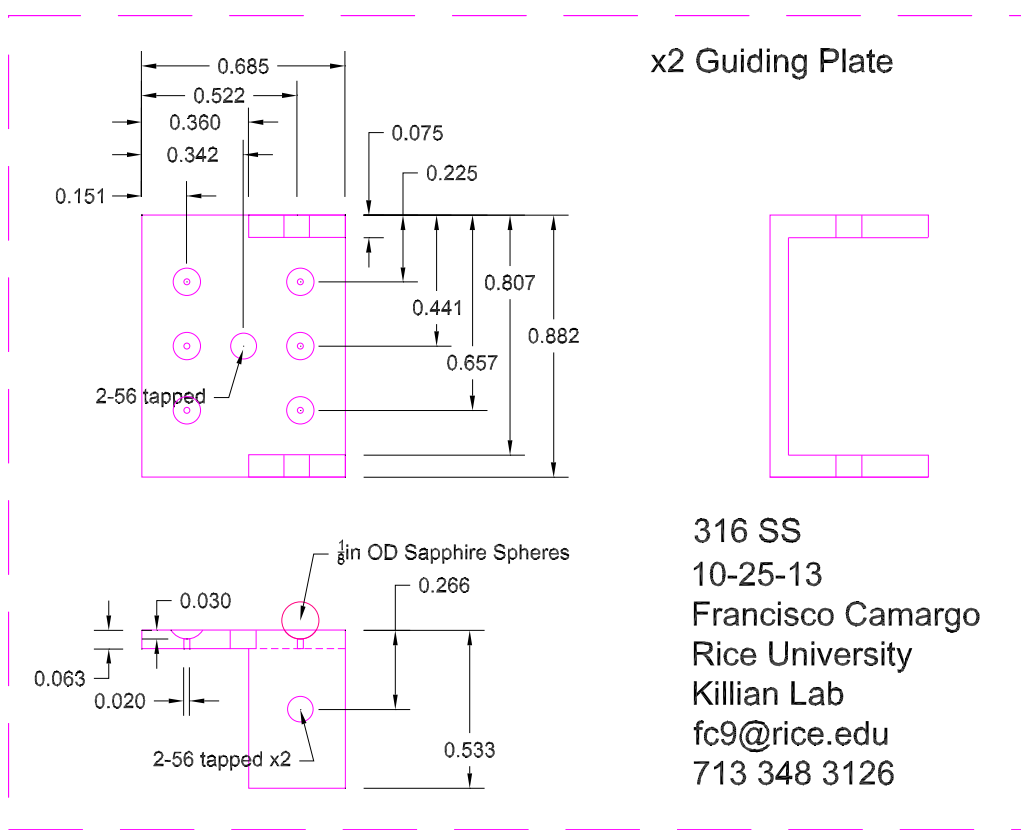


Figure D.9: Guiding plates used to displace the electron path vertically.



# List of Figures

2.1	Energy level diagram of strontium. . . . .	8
2.2	Schematic of 461 nm cooling and trapping stages. Shown is the oven-nozzle (light-blue), 2D-Collimator (red), Zeeman Slower (orange), MOT chamber (dark blue), MOT coils (pink), and arrows indicating the atom-beam propagation direction (red arrow) and 461 nm beams (blue arrows). . . . .	8
2.3	Schematic of optical setup used to generate ODT recycled beam configuration. Made using image library created by Alexander Franzen. . . . .	11
2.4	Traces of ODT beams before and after converging to a single beam. . . . .	12
2.5	Schematic of RF components used to generate Top-Hat trap in combination with an IR AOM. . . . .	13
2.6	TOF atom images in at various times during evaporation in the absence of a preceding Top-Hat phase. . . . .	15
2.7	One dimensional slices of atom images from Fig. 2.6, and fits. . . . .	16
2.8	TOF atom images in at various times during evaporation following a Top-Hat phase. . . . .	17
2.9	One dimensional slices of atom images from Fig. 2.8, and fits. . . . .	18
2.10	A comparison of BEC production with and without the use of the top-hat trap. (a) Total number of atoms as a function of time. (b) Number of condensate atoms. (c) BEC fraction. (d) Thermal temperature. . . . .	19
3.1	Relevant energy level diagram of strontium for two-photon Rydberg transitions.	22
3.2	(a) Measured energy of $5sns^3S_1$ $^{84}\text{Sr}$ states. (b) Corresponding fractional fitting residuals. . . . .	23

3.3	In red is the binding energy of an atom in the $n = 20$ state. The other traces are the potentials experienced by an electron at different values of external electric field. In orange is the potential of an electron with an external field equal to the classical ionization field for $n = 20$ . The blue trace is at half the same ionization field, and the green trace has an external field twice as strong compared to the ionization field. . . . .	25
3.4	Layout of electrodes within our vacuum-chamber. 1 represents the chamber which sets ground. 10 is the MCP front-plate, 11 is the grounded MPC case. Atoms are in the geometric center of electrodes 2-9 which constitute the ionization electrodes. Plates 2, 5, 6, 9 are pulsed to positive voltages while 3, 4, 7, 8 are pulsed negatively. By doing so, the potential difference between the Rydberg electrons and the MCP is constant irrespective of the ionization fields and therefore the the states being ionized. Plates 12, 11, 13, 14 in these experiments always grounded. The front-plate of the MCP is set to 200V. . .	26
3.5	Electrode potential ramp measurement. . . . .	27
3.6	Sample charged particle signal after MCS discriminator with 100 ns resolution, plotted in electric-field units. . . . .	28
3.7	(a) For $2\ \mu\text{s}$ long pulses and 220 mW UV power, signal response is linear across the available red laser power. (b) At fixed laser powers, roll-over is evident as a function of laser pulse time. . . . .	29
3.8	For low number of excitations per pulse, detection is linear up to about four excitations per pulse and corresponding to one count on the MCP. . . . .	30
3.9	Here are two spectra each taken within the linear response regime. Between the two traces the UV power was changed, however shape invariance of the spectra is reflective of having taken the data in the linear regime. . . . .	31
4.1	Calculated molecular potential (black) at $n = 38$ and calculated wavefunctions for the $\nu = 0$ (red), 1 (green), and 2 (blue) molecular vibrational states. . . .	35

4.2	Measured Rydberg excitation spectrum (the parent $38^3S_1$ feature is attenuated by a factor of 10). Calculations done by Shuhei Yoshida of the positions and relative excitation strengths for the $\nu = 0, 1$ , and 2 molecular vibrational dimer states are indicated by the vertical bars. . . . .	37
4.3	Left column: spectra taken in thermal samples, right column: spectra taken in BEC samples. Top row: $n = 38$ spectra. Bottom row: $n = 49$ spectra. Pure atomic excitation is at zero detuning, and lines for dimers ( $X = D$ ) through hexamers ( $X = H$ ) are visible. Subscripts ( $X_{ij\dots}$ ) indicate the molecular levels of the Rydberg potential occupied by atoms after laser excitation. . . . .	38
4.4	Measured binding energies for the ground state wavefunctions of dimers (red), trimers (blue), and tetramers (green) along with $1/(n-\delta_l)^6$ fit trendlines. Data presented is a combination of results of from [7] and this work. . . . .	39
4.5	Left column: spectra taken in thermal samples, right column: spectra taken in BEC samples. Top row: $n = 60$ spectra. Bottom row: $n = 72$ spectra. . .	40
5.1	Schematic diagram of the timing sequence used to determine lifetimes. The time between laser pulses and the beginning of field-ionization is varied. We maintain the time between ionization ramps fixed at $230\ \mu s$ , a time long compared to the lifetimes measures such that no residual Rydberg states remain in between pulse sequences. . . . .	43
5.2	Evolution of the SFI spectrum for (a) the parent $38^3S_1$ Rydberg state and (b) the $\nu = 0$ molecular vibrational state as a function of delay time. The values of the various delay times used are as indicated. The arrows indicate the $n$ values of ${}^3P$ states populated by BBR-induced transitions. . . . .	44
5.3	Evolution of the population of $38^3S_1$ Rydberg atoms and of the molecular $\nu = 0, 1$ , and 2, vibrational states as a function of time delay $t_D$ . The data sets are each normalized to one at $t_D = 0$ . . . . .	45
5.4	Comparison of decay rate results between Sr and Rb [33]. Measured decay rates as a function of peak trap density with linear best fit lines. . . . .	46

5.5 Diagram of the two decay channels that arise from the internal dynamics of a Rydberg molecule. The blue circles denote the Rydberg ionic core, the purple circles and rings denote the Rydberg electron, and the red circles represent an initially bound atom. Associative ionization produces a $\text{Sr}_2^+$ molecule and a free electron. Through an L-changing collision, enough energy is released to dissociate the molecule and a Rydberg atom results with different values of $nL$ . . . . .	48
5.6 Excitation spectra recorded for (a) 49s, (b) 60s, and (c) 72s Rydberg states expressed as a function of detuning from the atomic line. The spectra are normalized to have equal areas. . . . .	49
5.7 Time evolution of the SFI spectra recorded for $n = 49$ and the detunings indicated. . . . .	50
5.8 Time evolution of the SFI spectra recorded for $n = 60$ and the detunings indicated. . . . .	51
5.9 Time evolution of the SFI spectra recorded for $n = 72$ and the detunings indicated. . . . .	52
5.10 Relative Rydberg population evolution over time. In the left-column, decay is plotted over a time range comparable to the natural decay of the Rydberg states. In the right-column a subset of the data is plotted where we focus on the first $5\ \mu\text{s}$ where AI and LCC are the dominant decay channels. The solid lines show the fits to the data obtained using Eqs. 5.8. Top-row: $n = 49$ , middle-row: $n = 60$ , bottom-row: $n = 72$ . . . . .	54
5.11 Circles: Rydberg molecule destruction rates, $\Gamma_{AI} + \Gamma_L$ , measured in a BEC for the detunings, $\gamma$ , indicated. The colored solid lines show the results of model simulations (see text). Triangles: radiative decay rates, $\Gamma_R$ , measured using thermal samples on atomic resonance and L-changed atoms created in a BEC [35]. The black solid line indicates a fit to the radiative decay rates on resonance. . . . .	55
5.12 $\Gamma_{AI} + \Gamma_L$ plotted versus UV laser detuning at various values of $n$ . Plotted are both simulation and experimental results which each demonstrated a linear dependence. . . . .	56

5.13 L-changing and associative ionization collisions times in a BEC Rb at various detunings as measured and plotted in Ref. [36]. Rates range from $\sim 2 \times 10^5 \text{ s}^{-1}$ at -3 MHz detuning to $\sim 10^6 \text{ s}^{-1}$ at -48 MHz for quantum numbers between 50 and 70. . . . .	57
5.14 Comparison of decay rate measurements made in the few- and many-body regime. We have extrapolated the predictions made by each model. The offset between the two trendlines alludes to the incompatibility of the models across all density. Measurements at $n = 49, 60, 72$ correspond to the many-body regime, measurements at $n = 38$ correspond to the few-body regime. . . . .	58
6.1 Plot of $-A_{\text{Eff}}$ versus $n - \delta_l$ . . . . .	62
6.2 Plot of the shape of (a) thermal and (b) BEC density distributions as a function of the ratio of density to peak density. . . . .	64
6.3 Comparison of spectra at different values of peak density. Left column: $n = 60$ data, right column: $n = 72$ data. Top row: data plotted versus laser frequency. Second row: data scaled to value of detuning at peak density calculated separately for each trace. Bottom row: same results in log scale demonstrating agreement of signal at high detuning. . . . .	65
6.4 Mean-field fits to BEC spectra with (left) and without (right) convolution with the number of atoms within a Rydberg orbital. Top- middle- and bottom-rows correspond to $n = 49, 60, 72$ , respectively. Blue dots: experimental data, black line: mean-field best-fit result, red band: confidence interval of fit, green band: thermal atoms confidence interval. . . . .	67
6.5 Now the data is plotted with an uncertainty band corresponding to $\xi = 1.8(4)$ . Top-row: $n = 49$ , middle-row: $n = 60$ , bottom-row: $n = 72$ . Left-column: linear scale, right-column: log scale. . . . .	68
6.6 Comparison of spectra data, mean-field calculation, and the calculation with the inclusion of convolution with the number of atoms within a Rydberg wavefunction according to 6.18. Top-row: $n = 60$ , bottom-row: $n = 72$ , left-column: linear scale, right-column: log scale. . . . .	73

7.1 Schematic of the excitation of a Rydberg polaron in a uniform-density BEC. Laser excitation projects the system into final configurations involving atoms in bound and scattering states $ \beta_i\rangle$ that satisfy energy conservation. Bound states are confined in the Rydberg potential $V(\mathbf{r})$	77
7.2 BEC spectra data and theory results. Top row: $n = 38$ data, bottom row: $n = 49$ data. Left column: data and theory plotted versus laser frequency in linear scale. Right column: log-scale plot of same data.	79
7.3 BEC spectra data and theory results. Top row: $n = 60$ data, bottom row: $n = 72$ data. Left column: data and theory plotted versus laser frequency in linear scale. Right column: log-scale plot of same data.	80
7.4 Rydberg excitation in the many-body regime for $n = 49, 60, 72$ with a frequency axis scaled by the mean-field shift at peak density. Symbols are the experimental data. Lines are FDT or mean-field calculations. Laser detuning and signal are scaled as described in the text. The mean-field prediction is for the condensate atoms only. Deviations between the mean-field result and data at small detuning ( $-\Delta/\Delta_0 > -0.3$ ) represent contributions from the non-condensed thermal atoms. The shaded regions represent the predicted polaron response from the center of atom cloud as obtained from FDT. Theory for this high-density region matches the tail of the experimental data and represents the Rydberg-impurity spectral function for a nearly uniform-density region. For uniform density, the width of the spectrum scales as $n^{-3}$ .	81
A.1 Trace of numerically calculated potential ( $\bar{\omega} = 2\pi \times 265 \text{ s}^{-1}$ ) along the direction of gravity. Also plotted is an analytic harmonic approximation to the potential. Though the minimum of the trap is $\sim 40 \mu\text{K}$ , the effect of gravity lowers the effective trap depth to $\sim 30 \mu\text{K}$ .	90
A.2 Plot demonstrating the universal shape of the density distribution of a thermal gas in a harmonic trap.	91
A.3 Example trap frequency oscillation measurement depicting data and fit.	93

A.4 Trace of numerically calculated spatial density distribution ( $\bar{\omega} = 2\pi \times 222 \text{ s}^{-1}$ , $N_{\text{Th}} = 2.5 \times 10^6$ , $T = 1.5 \mu\text{K}$ ) along the direction of gravity. Also plotted is an analytic harmonic approximation result. The numerical result indicates a 14% lower peak density which occurs due to atoms occupying regions of space further away from the trap minimum compared to a perfectly harmonic trap, subject to the constraint that the total atom number is the same. . . . .	94
A.5 Here is the distribution of density resulting from the numerical calculation as well as the analytically solution, showing good agreement. . . . .	95
A.6 Mean-field calculations and data for spectra at (a) $n = 60$ and (b) $n = 72$ . Both analytic and numerical calculations are presented. Additionally, a correction that accounts for density fluctuations is applied to either method, as described in Ch. 6. . . . .	96
B.1 Plot of the density distribution of a BEC in a harmonic trap, parameterized by $\rho/\rho_0$ . . . . .	98
B.2 Plot of harmonic potential (blue) and modified potential Eq. B.10 (dashed yellow) for thermal atoms in two-component atomic cloud. The rise in energy below the Thomas-Fermi radius results in decreasing density away from the edge of the BEC. . . . .	99
B.3 Plot of modified $\mathcal{V}_{\text{Eff}}$ versus the ratio of the Thomas-Fermi radius to the thermal cloud width. . . . .	100
B.4 Plot of BEC density (green), two-component thermal density (dashed yellow) and the sum (blue). . . . .	101
B.5 Plot of BEC density distribution (green), thermal gas density distribution (red), and two-component cloud density distribution (blue). The same parameters are used for each trace, each trace is also normalized by the number of atoms such that the integral of each trace is unity. . . . .	102
B.6 Time of flight results for the width of the cloud in vertical and radial direction in addition to Casin-Dum fit results. . . . .	103

B.7 Plot of BEC fraction as a function of the ratio of temperature to critical temperature for a three-dimensional harmonic trap ( $\alpha = 3$ ). Similar results have been observed [97] . . . . .	104
C.1 (a) Image of top-hat configuration on CCD camera. (b) Traces of ODT beams before and after converging to a single beam. . . . .	106
D.1 Full electrode assembly attached to the bottom vacuum flange. Some of the electrodes are pictured (copper). Each electrode is connected to a feedthrough on the bottom flange via copper wire insulated by ceramic spacers. . . . .	108
D.2 Side view of the electrode assembly. Pictured are some of the ionization electrodes, the lensing and vertical guiding plates, as well as the sapphire spheres (pink) used to set the spacing between the electrodes and the scaffold. The electrodes are held in place with bolts insulated from the electrodes using ceramic washers. . . . .	109
D.3 Assembly of electrodes (pink) within the vacuum chamber (blue), the electrodes are suspended by but not in direct contact with a pair of scaffold plates (red). Also pictured is the lensing plate (orange) and the vertical guideing plates (green). . . . .	110
D.4 Scaffold used to suspend ionization electrodes. . . . .	111
D.5 Ionization electrode plates. . . . .	112
D.6 Support pieces used to attach scaffold to bottom chamber flange. . . . .	113
D.7 Support pieces used to support top scaffold. . . . .	113
D.8 Lensing plate used to focus path of electrons as they traverse towards the MCP. . . . .	114
D.9 Guiding plates used to displace the electron path vertically. . . . .	115

# List of Tables

1.1	List of scaling laws and values for Sr $5s38s\ ^3S_1$ . . . . .	4
5.1	Decay rate results and estimated collisional cross-sections for Rydberg atoms and molecules on the $5s38s\ ^3S_1$ line. . . . .	46
6.1	Experimentally determined parameters. Number of atoms in the condensate ( $N_{\text{BEC}}$ ) and mean trap frequency $\bar{\omega}$ are determined from time-of-flight-absorption images and Castin-Dum measurements (see Appendix B.3) respectively, and they determine the peak condensate density ( $\rho_0$ ) and chemical potential ( $\mu$ ). . . . .	66
6.2	Fit parameters from data shown in Fig. 6.4. BEC fraction ( $\eta$ ) and shift at peak density ( $\Delta_0$ ) are determined from the spectra. . . . .	66
6.3	Experimentally determined parameters. Number of atoms in the sample ( $N_{\text{Th}}$ ), temperature ( $T$ ) are determined from time-of-flight-absorption images. The mean trap-frequency $\bar{\omega}$ is determined from measurements of collective mode frequencies for trapped atoms. Together, these parameters determine the peak density ( $\rho_0$ ). . . . .	72



# Bibliography

- [1] J. R. Rydberg. On the structure of the line-spectra of the chemical elements. *Philosophical Magazine Series 5*, 29(179):331–337, 1890.
- [2] R. F. Stebbings and F. B. Dunning. *Rydberg States of Atoms and Molecules*. Cambridge University Press, 1983.
- [3] V. Alan Kostelecký and Michael Martin Nieto. Analytical wave functions for atomic quantum-defect theory. *Phys. Rev. A*, 32:3243–3246, Dec 1985.
- [4] A. R. P. Rau and Mitio Inokuti. The quantum defect: Early history and recent developments. *American Journal of Physics*, 65(3):221–225, 1997.
- [5] Markus Mack, Florian Karlewski, Helge Hattermann, Simone Höckh, Florian Jessen, Daniel Cano, and József Fortágh. Measurement of absolute transition frequencies of  $^{87}\text{Rb}$  to  $nS$  and  $nD$  rydberg states by means of electromagnetically induced transparency. *Phys. Rev. A*, 83:052515, May 2011.
- [6] C L Vaillant, M P A Jones, and R M Potvliege. Long-range rydberg–rydberg interactions in calcium, strontium and ytterbium. *Journal of Physics B: Atomic, Molecular and Optical Physics*, 45(13):135004, 2012.
- [7] B. J. DeSalvo, J. A. Aman, F. B. Dunning, T. C. Killian, H. R. Sadeghpour, S. Yoshida, and J. Burgdörfer. Ultra-long-range rydberg molecules in a divalent atomic system. *Phys. Rev. A*, 92:031403, Sep 2015.
- [8] Niels Bohr. On the constitution of atoms and molecules. *Philosophical Magazine*, 26(151):1–25, 1913.

- [9] E. Amaldi and E. Segré. Effect of pressure on high terms of alkaline spectra. *Nature*, 133(3352):141–141, 1934.
- [10] Enrico Fermi. Sopra lo spostamento per pressione delle righe elevate delle serie spettrali. *Il Nuovo Cimento (1924-1942)*, 11(3):157, 1934.
- [11] Chris H. Greene, A. S. Dickinson, and H. R. Sadeghpour. Creation of polar and nonpolar ultra-long-range rydberg molecules. *Phys. Rev. Lett.*, 85:2458–2461, Sep 2000.
- [12] I. I. Fabrikant. Interaction of rydberg atoms and thermal electrons with k, rb and cs atoms. *Journal of Physics B: Atomic and Molecular Physics*, 19(10):1527, 1986.
- [13] A. A. Khuskivadze, M. I. Chibisov, and I. I. Fabrikant. Adiabatic energy levels and electric dipole moments of rydberg states of rb<sub>2</sub> and cs<sub>2</sub> dimers. *Phys. Rev. A*, 66:042709, Oct 2002.
- [14] C. Bahrim and U. Thumm. Low-lying <sup>3</sup>P<sup>o</sup> and <sup>3</sup>S<sup>e</sup> states of rb<sup>-</sup>, cs<sup>-</sup>, and fr<sup>-</sup>. *Phys. Rev. A*, 61:022722, Jan 2000.
- [15] C. Bahrim, U. Thumm, and I. I. Fabrikant. 3 s e and 1 s e scattering lengths for e - + rb, cs and fr collisions. *Journal of Physics B: Atomic, Molecular and Optical Physics*, 34(6):L195, 2001.
- [16] M. H. Anderson, J. R. Ensher, M. R. Matthews, C. E. Wieman, and E. A. Cornell. Observation of bose-einstein condensation in a dilute atomic vapor. *Science*, 269(5221):198–201, 1995.
- [17] K. B. Davis, M. O. Mewes, M. R. Andrews, N. J. van Druten, D. S. Durfee, D. M. Kurn, and W. Ketterle. Bose-einstein condensation in a gas of sodium atoms. *Phys. Rev. Lett.*, 75:3969–3973, Nov 1995.
- [18] C. C. Bradley, C. A. Sackett, J. J. Tollett, and R. G. Hulet. Evidence of bose-einstein condensation in an atomic gas with attractive interactions [phys. rev. lett. 75, 1687 (1995)]. *Phys. Rev. Lett.*, 79:1170–1170, Aug 1997.

- [19] Simon Stellmer, Meng Khoon Tey, Bo Huang, Rudolf Grimm, and Florian Schreck. Bose-einstein condensation of strontium. *Phys. Rev. Lett.*, 103:200401, Nov 2009.
- [20] Y. N. Martinez de Escobar, P. G. Mickelson, M. Yan, B. J. DeSalvo, S. B. Nagel, and T. C. Killian. Bose-einstein condensation of  $^{84}\text{Sr}$ . *Phys. Rev. Lett.*, 103:200402, Nov 2009.
- [21] C. J. Pethick and H. Smith. *Bose-Einstein Condensation in Dilute Gases*. Cambridge University Press, 2008.
- [22] V. Bendkowsky, B. Butscher, J. Nipper, J. P. Shaffer, R. Löw, and T. Pfau. Observation of ultralong-range Rydberg molecules. *Nature*, 458(7241):1005, April 2009.
- [23] J. Tallant, S. T. Rittenhouse, D. Booth, H. R. Sadeghpour, and J. P. Shaffer. Observation of blueshifted ultralong-range  $\text{Cs}_2$  rydberg molecules. *Phys. Rev. Lett.*, 109:173202, Oct 2012.
- [24] Heiner Saßmannshausen, Frédéric Merkt, and Johannes Deiglmayr. Experimental characterization of singlet scattering channels in long-range rydberg molecules. *Phys. Rev. Lett.*, 114:133201, Mar 2015.
- [25] A. T. Krupp, A. Gaj, J. B. Balewski, P. Ilzhöfer, S. Hofferberth, R. Löw, T. Pfau, M. Kurz, and P. Schmelcher. Alignment of  $d$ -state rydberg molecules. *Phys. Rev. Lett.*, 112:143008, Apr 2014.
- [26] D. A. Anderson, S. A. Miller, and G. Raithel. Photoassociation of long-range  $nd$  rydberg molecules. *Phys. Rev. Lett.*, 112:163201, Apr 2014.
- [27] M. A. Bellos, R. Carollo, J. Banerjee, E. E. Eyler, P. L. Gould, and W. C. Stwalley. Excitation of weakly bound molecules to trilobitelike rydberg states. *Phys. Rev. Lett.*, 111:053001, Jul 2013.
- [28] D. Booth, S. T. Rittenhouse, J. Yang, H. R. Sadeghpour, and J. P. Shaffer. Production of trilobite rydberg molecule dimers with kilo-debye permanent electric dipole moments. *Science*, 348(6230):99–102, 2015.

- [29] Edward L Hamilton, Chris H Greene, and H R Sadeghpour. Shape-resonance-induced long-range molecular rydberg states. *Journal of Physics B: Atomic, Molecular and Optical Physics*, 35(10):L199, 2002.
- [30] Thomas Niederprüm, Oliver Thomas, Tanita Eichert, Carsten Lippe, Jesús Pérez-Ríos, Chris H. Greene, and Herwig Ott. Observation of pendular butterfly rydberg molecules. *Nature Communications*, 7:12820, May 2016.
- [31] A. Gaj, A. T. Krupp, J. B. Balewski, R. Löw, S. Hofferberth, and T. Pfau. From molecular spectra to a density shift in dense Rydberg gases. *Nature communications*, 5:4546, 2014.
- [32] D B Branden, T Juhasz, T Mahlokozera, C Vesa, R O Wilson, M Zheng, A Kortyna, and D A Tate. Radiative lifetime measurements of rubidium rydberg states. *Journal of Physics B: Atomic, Molecular and Optical Physics*, 43(1):015002, 2010.
- [33] Björn Butscher, Vera Bendkowsky, Johannes Nipper, Jonathan B Balewski, Ludmila Kukota, Robert Löw, Tilman Pfau, Weibin Li, Thomas Pohl, and Jan Michael Rost. Lifetimes of ultralong-range Rydberg molecules in vibrational ground and excited states. *Journal of Physics B: Atomic, Molecular and Optical Physics*, 44(18):184004, September 2011.
- [34] J. B. Balewski, A. T. Krupp, A. Gaj, D. Peter, H. P. Büchler, R. Löw, S. Hofferberth, and T. Pfau. Coupling a single electron to a Bose-Einstein condensate. *Nature*, 502(7473):664, October 2013.
- [35] F. Camargo, J. D. Whalen, R. Ding, H. R. Sadeghpour, S. Yoshida, J. Burgdörfer, F. B. Dunning, and T. C. Killian. Lifetimes of ultra-long-range strontium rydberg molecules. *Phys. Rev. A*, 93:022702, Feb 2016.
- [36] Michael Schlagmüller, Tara Cubel Liebisch, Felix Engel, Kathrin S. Kleinbach, Fabian Böttcher, Udo Hermann, Karl M. Westphal, Anita Gaj, Robert Löw, Sebastian Hofferberth, Tilman Pfau, Jesús Pérez-Ríos, and Chris H. Greene. Ultracold chemical reactions of a single rydberg atom in a dense gas. *Phys. Rev. X*, 6:031020, Aug 2016.

- [37] J. D. Whalen, F. Camargo, R. Ding, T. C. Killian, F. B. Dunning, Jesús Pérez-Ríos, S. Yoshida, and J. Burgdörfer. Lifetimes of ultralong-range strontium rydberg molecules in a dense bec. 2017.
- [38] L Barbier and M Cheret. Experimental study of penning and hornbeck-molnar ionisation of rubidium atoms excited in a high s or d level ( $5d \leq nl \leq 11s$ ). *Journal of Physics B: Atomic and Molecular Physics*, 20(6):1229, 1987.
- [39] I.L Beigman and V.S Lebedev. Collision theory of rydberg atoms with neutral and charged particles. *Physics Reports*, 250(3):95 – 328, 1995.
- [40] A. Kumar, B.C. Saha, C.A. Weatherford, and S.K. Verma. A systematic study of hornbeck molnar ionization involving rydberg alkali atoms. *Journal of Molecular Structure: THEOCHEM*, 487(1):1 – 9, 1999.
- [41] A. A. Mihajlov, V. A. Srećković, Lj. M. Ignjatović, and A. N. Klyucharev. The chemi-ionization processes in slow collisions of rydberg atoms with ground state atoms: Mechanism and applications. *Journal of Cluster Science*, 23(1):47–75, 2012.
- [42] Thomas Niederprüm, Oliver Thomas, Torsten Manthey, Tobias M. Weber, and Herwig Ott. Giant cross section for molecular ion formation in ultracold rydberg gases. *Phys. Rev. Lett.*, 115:013003, Jul 2015.
- [43] S. Kunze, R. Hohmann, H. J. Kluge, J. Lantzsch, L. Monz, J. Stenner, K. Stratmann, K. Wendt, and K. Zimmer. Lifetime measurements of highly excited rydberg states of strontium i. *Zeitschrift für Physik D Atoms, Molecules and Clusters*, 27(2):111–114, 1993.
- [44] Richard Schmidt, H. R. Sadeghpour, and E. Demler. Mesoscopic rydberg impurity in an atomic quantum gas. *Phys. Rev. Lett.*, 116:105302, Mar 2016.
- [45] F. Camargo, R. Schmidt, J. D. Whalen, R. Ding, G Woehl Jr., S. Yoshida, J. Burgdörfer, F. B. Dunning, H. R. Sadeghpour, E. Demler, and T. C. Killian. Creation of rydberg polarons in a bose gas. *arxiv*, 2017.

- [46] T. F. Gallagher. *Rydberg Atoms*. Cambridge University Press, 1994.
- [47] V. Bendkowsky, B. Butscher, J. Nipper, J. B. Balewski, J. P. Shaffer, R. Löw, T. Pfau, W. Li, J. Stanojevic, T. Pohl, and J. M. Rost. Rydberg trimers and excited dimers bound by internal quantum reflection. *Phys. Rev. Lett.*, 105:163201, Oct 2010.
- [48] Francisco Camargo. Strontium laser cooling and trapping apparatus. Master's thesis, Rice University, 2015.
- [49] Roger Ding. Narrow line cooling of  $^{84}\text{Sr}$ . Master's thesis, Rice University, 2016.
- [50] Wolfgang Ketterle and N.j. Van Druten. Evaporative cooling of trapped atoms. *Advances In Atomic, Molecular, and Optical Physics*, page 181–236, 1996.
- [51] Rudolf Grimm, Matthias Weidemüller, and Yurii B. Ovchinnikov. Optical dipole traps for neutral atoms. *Advances In Atomic, Molecular, and Optical Physics*, page 95–170, 2000.
- [52] Dimitris Trypogeorgos, Tiffany Harte, Alexis Bonnin, and Christopher Foot. Precise shaping of laser light by an acousto-optic deflector. *Optics Express*, 21(21):24837, Oct 2013.
- [53] K. M. O'Hara, M. E. Gehm, S. R. Granade, and J. E. Thomas. Scaling laws for evaporative cooling in time-dependent optical traps. *Phys. Rev. A*, 64:051403, Oct 2001.
- [54] Y. N. Martinez de Escobar, P. G. Mickelson, P. Pellegrini, S. B. Nagel, A. Traverso, M. Yan, R. Côté, and T. C. Killian. Two-photon photoassociative spectroscopy of ultracold  $^{88}\text{Sr}$ . *Phys. Rev. A*, 78:062708, Dec 2008.
- [55] Brian J. DeSalvo. *Ultralong-Range Molecules and Rydberg Blockade in Ultracold  $^{84}\text{Sr}$* . PhD thesis, Rice University, 2015.
- [56] T. H. Jeys, G. W. Foltz, K. A. Smith, E. J. Beiting, F. G. Kellert, F. B. Dunning, and R. F. Stebbings. Diabatic field ionization of highly excited sodium atoms. *Phys. Rev. Lett.*, 44:390–393, Feb 1980.

- [57] E. Urban, T. a. Johnson, T. Henage, L. Isenhower, D. D. Yavuz, T. G. Walker, and M. Saffman. Observation of Rydberg blockade between two atoms. *Nat. Phys.*, 5(2):110–114, January 2009.
- [58] B. J. DeSalvo, J. A. Aman, C. Gaul, T. Pohl, S. Yoshida, J. Burgdörfer, K. R. A. Hazzard, F. B. Dunning, and T. C. Killian. Rydberg-blockade effects in autler-townes spectra of ultracold strontium. *Phys. Rev. A*, 93:022709, Feb 2016.
- [59] Omont, A. On the theory of collisions of atoms in rydberg states with neutral particles. *J. Phys. France*, 38(11):1343–1359, 1977.
- [60] David Alexander Anderson. *Rydberg molecules and circular Rydberg states in cold atom clouds*. PhD thesis, The University of Michigan, 2015.
- [61] Thomas F. O’Malley, Leonard Rosenberg, and Larry Spruch. Low-energy scattering of a charged particle by a neutral polarizable system. *Phys. Rev.*, 125:1300–1310, Feb 1962.
- [62] Henry L. Schwartz, Thomas M. Miller, and Benjamin Bederson. Measurement of the static electric dipole polarizabilities of barium and strontium. *Phys. Rev. A*, 10:1924–1926, Dec 1974.
- [63] K Bartschat and H R Sadeghpour. Ultralow-energy electron scattering from alkaline-earth atoms: the scattering-length limit. *Journal of Physics B: Atomic, Molecular and Optical Physics*, 36(1):L9, 2003.
- [64] M. Born and R. Oppenheimer. Zur quantentheorie der moleküle. *Annalen der Physik*, 389(20):457–484, 1927.
- [65] I. I. Beterov, D. B. Tretyakov, I. I. Ryabtsev, A. Ekers, and N. N. Bezuglov. Ionization of sodium and rubidium  $ns$ ,  $np$ , and  $nd$  rydberg atoms by blackbody radiation. *Phys. Rev. A*, 75:052720, May 2007.
- [66] I. L. Glukhov, E. A. Nekipelov, and V. D. Ovsiannikov. Blackbody-induced decay, excitation and ionization rates for rydberg states in hydrogen and helium atoms. *Journal of Physics B: Atomic, Molecular and Optical Physics*, 43(12):125002, 2010.

- [67] V D Ovsiannikov, I L Glukhov, and E A Nekipelov. Rates of blackbody radiation-induced transitions from rydberg states of alkali atoms. *Journal of Physics B: Atomic, Molecular and Optical Physics*, 44(19):195010, 2011.
- [68] W. Li, T. Pohl, J. M. Rost, Seth T. Rittenhouse, H. R. Sadeghpour, J. Nipper, B. Butscher, J. B. Balewski, V. Bendkowsky, R. Löw, and T. Pfau. A homonuclear molecule with a permanent electric dipole moment. *Science*, 334(6059):1110–1114, 2011.
- [69] Yan-mei Yu, Bing-bing Suo, Hui-hui Feng, Heng Fan, and Wu-Ming Liu. Finite-field calculation of static polarizabilities and hyperpolarizabilities of  $\text{in}^+$  and  $\text{sr}$ . *Phys. Rev. A*, 92:052515, Nov 2015.
- [70] Thomas C. Killian.  $1s - 2s$  spectrum of a hydrogen bose-einstein condensate. *Phys. Rev. A*, 61:033611, Feb 2000.
- [71] Franco Dalfovo, Stefano Giorgini, Lev P. Pitaevskii, and Sandro Stringari. Theory of bose-einstein condensation in trapped gases. *Rev. Mod. Phys.*, 71:463–512, Apr 1999.
- [72] Mi Yan. *Optical Feshbach Resonances and Coherent Photoassociation in a Strontium BEC*. PhD thesis, Rice University, 2013.
- [73] R. P. Smith. Effects of interactions on bose-einstein condensation. *arxiv*, 2016.
- [74] Naaman Tammuz, Robert P. Smith, Robert L. D. Campbell, Scott Beattie, Stuart Moulder, Jean Dalibard, and Zoran Hadzibabic. Can a bose gas be saturated? *Phys. Rev. Lett.*, 106:230401, Jun 2011.
- [75] Michael Schlagmüller, Tara Cubel Liebisch, Huan Nguyen, Graham Lochead, Felix Engel, Fabian Böttcher, Karl M. Westphal, Kathrin S. Kleinbach, Robert Löw, Sebastian Hofferberth, Tilman Pfau, Jesús Pérez-Ríos, and Chris H. Greene. Probing an electron scattering resonance using rydberg molecules within a dense and ultracold gas. *Phys. Rev. Lett.*, 116:053001, Feb 2016.
- [76] M. Naraschewski and R. J. Glauber. Spatial coherence and density correlations of trapped bose gases. *Phys. Rev. A*, 59:4595–4607, Jun 1999.

- [77] Joe D. Whalen. Probing many-body correlations with ultralong-range rydberg molecules. Master's thesis, Rice University, 2016.
- [78] P. R. Bevington and D. K. Robinson. *Data Reduction and Error Analysis for the Physical Sciences*. McGraw-Hill, 2002.
- [79] L. D. Landau. über die bewegung der elektronen in kristalgitter. *Phys. Z. Sowjetunion*, 3:644–645, 1933.
- [80] J. T. Devreese and F. Peters, editors. *Polarons and Excitons in Polar Semiconductors and Ionic Crystals*. Plenum Press, New York, 1984.
- [81] S. Watanabe, K. Ando, K. Kang, S. Mooser, Y. Vaynzof, H. Kurebayashi, E. Saitoh, and H. Sirringhaus. Polaron spin current transport in organic semiconductors. *Nature Physics*, 10(4):308, 2014.
- [82] A. Schirotzek, C.-H. Wu, A. Sommer, and M. W. Zwierlein. Observation of fermi polarons in a tunable fermi liquid of ultracold atoms. *Phys. Rev. Lett.*, 102:230402, 2009.
- [83] Ming-Guang Hu, Michael J. Van de Graaff, Dhruv Kedar, John P. Corson, Eric A. Cornell, and Deborah S. Jin. Bose polarons in the strongly interacting regime. *Phys. Rev. Lett.*, 117:055301, Jul 2016.
- [84] Nils B. Jørgensen, Lars Wacker, Kristoffer T. Skalmstang, Meera M. Parish, Jesper Levinsen, Rasmus S. Christensen, Georg M. Bruun, and Jan J. Arlt. Observation of attractive and repulsive polarons in a bose-einstein condensate. *Phys. Rev. Lett.*, 117:055302, Jul 2016.
- [85] J. T. Devreese and A. S. Alexandrov. Fröhlich polaron and bipolaron: recent developments. *Reports on Progress in Physics*, 72(6):066501, 2009.
- [86] M. I. Chibisov, A. A. Khuskivadze, and I. I. Fabrikant. Energies and dipole moments of long-range molecular rydberg states. *Journal of Physics B: Atomic, Molecular and Optical Physics*, 35(10):L193, 2002.

- [87] Marko Cetina, Michael Jag, Rianne S. Lous, Jook T. M. Walraven, Rudolf Grimm, Rasmus S. Christensen, and Georg M. Bruun. Decoherence of impurities in a fermi sea of ultracold atoms. *Phys. Rev. Lett.*, 115:135302, Sep 2015.
- [88] Michael Knap, Aditya Shashi, Yusuke Nishida, Adilet Imambekov, Dmitry A. Abanin, and Eugene Demler. Time-dependent impurity in ultracold fermions: Orthogonality catastrophe and beyond. *Phys. Rev. X*, 2:041020, Dec 2012.
- [89] Marko Cetina, Michael Jag, Rianne S. Lous, Isabella Fritzsche, Jook T. M. Walraven, Rudolf Grimm, Jesper Levinsen, Meera M. Parish, Richard Schmidt, Michael Knap, and Eugene Demler. Ultrafast many-body interferometry of impurities coupled to a fermi sea. *Science*, 354(6308):96–99, 2016.
- [90] Richard Schmidt, Michael Knap, Dmitri A. Ivanov, Jhih-Shih You, Marko Cetina, and Eugene Demler. Universal many-body response of heavy impurities coupled to a fermi sea. *arxiv*, 2017.
- [91] Jun Ye, H. J. Kimble, and Hidetoshi Katori. Quantum state engineering and precision metrology using state-insensitive light traps. *Science*, 320(5884):1734–1738, 2008.
- [92] Pascal Gerry Mickelson. *Trapping and Evaporation of  $^{87}\text{Sr}$  and  $^{88}\text{Sr}$  Mixtures*. PhD thesis, Rice University, 2010.
- [93] A. Traverso, R. Chakraborty, Y. N. Martinez de Escobar, P. G. Mickelson, S. B. Nagel, M. Yan, and T. C. Killian. Inelastic and elastic collision rates for triplet states of ultracold strontium. *Phys. Rev. A*, 79:060702, Jun 2009.
- [94] Pascal Gerry Mickelson. Saturation effects in photoassociation spectroscopy of  $^{86}\text{sr}$ . Master’s thesis, Rice University, 2006.
- [95] L. P. Pitaevskii and S. Stringari. *Bose-Einstein condensation*. Clarendon Press, 2013.
- [96] R.j. Dodd, K. Burnett, M. Edwards, and Ch.w. Clark. Trapped bose-einstein condensates at finite temperature: a two-gas model. *Acta Physica Polonica A*, 93(1):45–53, 1998.

- [97] Simon Stellmer. *Degenerate quantum gases of strontium*. PhD thesis, University of Innsbruck, 2013.
- [98] Robert Löw, Hendrik Weimer, Johannes Nipper, Jonathan B Balewski, Björn Butscher, Hans Peter Büchler, and Tilman Pfau. An experimental and theoretical guide to strongly interacting rydberg gases. *Journal of Physics B: Atomic, Molecular and Optical Physics*, 45(11):113001, 2012.